Enhancing the electrocatalytic activity of phthalocyanines through finding the ideal combination of substituents in push-pull phthalocyanine-based systems

REITUMETSE PRECIOUS NKHAHLE

A thesis submitted in fulfilment of the requirements for the degree of

Doctor of Philosophy

Rhodes University

February 2023

ABSTRACT

Phthalocyanines (Pcs) are a class of synthetic pigments with a similar structure to porphyrins. The work presented in this thesis is centred around these electron-rich macrocycles and their use in electrocatalysis. This body of work provides a more rigorous analysis on asymmetric Pcs, focusing on finding the “ideal” combination of substituents in the synthesis of A_3B-type Pcs and how these asymmetric structures compare with their symmetric counterparts (A_4) in the electrocatalysis of hydrazine and nitrite.

The choice in substituents in the syntheses of the Pcs was such that there is both electron-donating and electron-withdrawing groups to induce a push-pull effect. In the studies involving the electrocatalysis of hydrazine, asymmetric cobalt Pcs (CoPcs) possessing alkyl groups as the primary substituents, with variations in the acid-containing group, along with their symmetric counterparts, probes with potential for further improvement were identified. Using voltammetric and amperometric techniques, the analyte-electrode kinetics, mechanism in which the electrochemical reaction proceeds along with the limits of detection (LoD) were determined. In the general sense, the pentadecylphenoxy-derived CoPcs performed better than those containing the *tert*-butyl substituent as the dominant substituent with the asymmetric CoPcs producing more favourable results than their symmetric analogues.

With respect to the probes designed for nitrite, a multi-dimensional approach was undertaken in that acetaminophen was chosen as the primary substituent whilst multiple changes in the asymmetric component were made. In addition to varying the carboxylic acid-containing substituent, alkyne- and amine-based substituents were also explored in which the alkyne-containing Pc was anchored onto the electrode surface through click chemistry while the amine-bearing Pc was covalently linked (and π-stacked) to nitrogen-doped graphene quantum dots (NGQDs). Another component that was altered was the central metal where CoPcs were compared to manganese Pcs (MnPcs). The most desirable peak oxidation potential for nitrite was observed in the MnPcs as it was the lowest with adsorption sometimes being a better suited method of electrode modification relative to clicking. The inclusion of NGQDs was found to be beneficial when combined with the symmetric CoPc whilst in the presence of an asymmetric Pc complex, less desirable results were observed. Overall, there were variations in the results with the symmetric CoPc sometimes being better than some of the asymmetric CoPcs demonstrating that a blanket-approach in terms of synthesizing and applying asymmetric Pcs is not always viable.

DECLARATION

The work presented in this thesis is my own and was conducted whilst completing the degree of Doctor of Philosophy in Chemistry whilst enrolled at Rhodes University. Any work that is not my own has been referenced accordingly. I, Reitumetse Precious Nkhahle, certify that this thesis has not been submitted for a degree at any other university, technikon or college.

Signed: ____________________

Date: ___08/02/2022_______

ACKNOWLEDGEMENTS

“Mazithi iingqondo zethu zimbonge uYehova, kuba iinceba zaKhe zimi ngonaphakade.
Kubo bonke oothixo, akekho onjengaYe, kuba iinceba zaKhe zimi ngonaphakade.”

“Sanctus, sanctus, sanctus dominus Deus Sabaoth
pleni sunt celi et terra gloria tua.
Hosanna in exelsis.”

To my supervisor, Professor Tebello Nyokong, thank you for being a great supervisor; for the knowledge imparted, the patience demonstrated and the freedom you have given us to create.

I would like to further express my gratitude to the following academic staff members, Prof John Mack, Dr Jonathan Britton and Dr Edward Kutloano Sekhosana.

A big thank you to Ms Gail Cobus for all the administrative support and Mr Francis Chindeka for the technical support. To my labmates in S22 and F26, the Chemistry Department, Marvin from the Electron Microscopy Unit, thank you all.

My family, mom and dad, Moreheng and Thabo Nkhahle; my siblings, Thapelo, Teboho, Phetho, Lifutso, and Aus’ Disebo, thank you for your support.

My dear friends, Lindokuhle “Kush” Nene, Nobuhle Ndebele and the great Azole Sindelo, thank you. This is our thesis. And thank you to Yonela Faba and Avuyonke Balfour too.

Furthermore, I would like to acknowledge the National Research Foundation in collaboration with the German government through the German Academic Exchange Service for funding (NRF-DAAD).

Opinions and conclusions expressed in this work are those of the author and not the NRF-DAAD.

CONTENTS

TITLE i

ABSTRACT ii

DECLARATION iv

ACKNOWLEDGEMENTS v

CONTENTS vi

LIST OF SYMBOLS xi

LIST OF ABBREVIATIONS xii

CHAPTER 1 1

1. Introduction 2

1.1 Catalysis – Electrocatalysis 2

1.2 Graphene quantum dots (GQDs) 7

1.2.1 Overview 7

1.2.2 Synthesis 7

1.3 Phthalocyanines 11

1.3.1 Structure and general applications 11

1.3.2 Synthesis 12

1.3.2.1 Symmetric phthalocyanines 12

1.3.2.2 Asymmetric phthalocyanines 14

1.3.3 Electronic spectra of phthalocyanines 16

1.3.4 Redox behaviour of phthalocyanines 17

1.3.5 Phthalocyanines in electrocatalysis 18

1.3.6 Phthalocyanines reported in this thesis 26

1.4 Analytes 33

1.4.1 Hydrazine 33

1.4.2 Nitrite 34

1.5 Aims and objectives 36

1.5.1 Aims 36

1.5.2 Objectives 36

CHAPTER 2 37

2. Experimental 38
2.1 Materials 38
2.1.1 Solvents 38
2.1.2 General materials 38
2.1.3 Previously reported materials 38
2.2 Equipment 39
2.2.1 Structural characterisation 39
2.2.2 Electrochemical characterisation and application 40
2.2.3 Theoretical procedure (DFT calculations) 40
2.3 Syntheses 41
2.3.1 Synthesis of tri-(3-pentadecylphenoxy)-mono-cinnamic acid cobalt(II) phthalocyanine (complex 1), *Scheme 3.1* 41
2.3.2 Synthesis of tri-(3-pentadecylphenoxy)-mono-phenoxy acetic acid cobalt(II) phthalocyanine (complex 2), *Scheme 3.1* 41
2.3.3 Syntheses of tri-(3-pentadecylphenoxy)-mono-phenoxy propanoic acid cobalt(II) phthalocyanine and 2,9,16,23-tetrakis-(3-pentadecylphenoxy) cobalt(II) phthalocyanine (complexes 3 and 5), *Scheme 3.1* 42
2.3.4 Synthesis of tri-(3-pentadecylphenoxy)-mono-caffeic acid cobalt(II) phthalocyanine (complex 4), *Scheme 3.1* 43
2.3.5 Synthesis of 4-(tri-*tert*-butyl)-mono phenoxy benzoic acid cobalt(II) phthalocyanine (complex 6), *Scheme 3.2* 44
2.3.6 Syntheses of tris-(4-acetamidophenoxy)-mono-(hex-5-yn-1-yloxy) cobalt(II) phthalocyanine and 2,9,16,23-tetrakis-acetamidophenoxy cobalt(II) phthalocyanine (complexes 8 and 9), *Scheme 3.3* 44
2.3.7 Syntheses of tris-(4-acetamidophenoxy)-mono-(hex-5-yn-1-yloxy) manganese(III) chloride phthalocyanine and 2,9,16,23-tetrakis-acetamidophenoxy manganese(III) 45

chloride phthalocyanine (complexes 10 and 11), *Scheme 3.3*
2.3.8 Synthesis of tris-(4-acetamidophenoxy)-mono-aminophenoxy cobalt(II) phthalocyanine (complex 12), *Scheme 3.3* 46
2.3.9 Synthesis of *tris*-(4-acetamidophenoxy)-mono-phenoxy benzoic acid cobalt(II) phthalocyanine (complex 13), *Scheme 3.3* 47
2.3.10 Synthesis of *tris*-(4-acetamidophenoxy)-mono-phenoxy propanoic acid cobalt(II) phthalocyanine (complex 14), *Scheme 3.3* 47
2.3.11 Synthesis of *tris*-(4-acetamidophenoxy)-mono-caffeic acid cobalt(II) phthalocyanine (complex 15), *Scheme 3.3* 48
2.4 Formation of conjugates 48
2.4.1 Conjugation through π-π stacking, *Scheme 3.4* 49
2.4.2 Conjugation through covalent linking, *Scheme 3.5* 49
2.5 Electrode modification 50
2.5.1 Modification through adsorption (drop-drying) 50
2.5.2 Modification through covalent anchoring ("clicking") 51
2.6 Attempted syntheses 52

RESULTS AND DISCUSSION 54
PUBLICATIONS 55

CHAPTER 3 56
3. Synthesis and characterisation 57
3.1 Phthalocyanine complexes 57
3.2 Characterisation of the composites 64
3.3 Summary of chapter 75

CHAPTER 4 76

4. Characterisation of the modified electrodes 77

4.1 Characterisation in a ferrocyanide-ferricyanide solution 77

4.1.1 Cyclic voltammetry 79

4.1.2 Electrochemical impedance spectroscopy (EIS) 83

4.1.3 Scanning electrochemical microscopy (SECM) 86

4.2 Characterisation in the buffers 88

4.3 Determination of the surface coverage 89

4.4 Confirmation of triazole ring formation 92

4.5 Summary of chapter 97

CHAPTER 5 98

5. Electrochemical sensing 99

5.1 Electro-oxidation of hydrazine 99

5.1.1 Voltammetric analyses 99

5.1.1.1 Kinetic studies on hydrazine-electrode interactions 103

5.1.1.2 Stability studies 107

5.1.2 Chronoamperometric analyses 109

5.1.2.1 Limits of detection 109

5.1.2.2 Catalytic rates 112

5.1.3 Computational chemistry 113

5.2 Electro-oxidation of nitrite 118

5.2.1 pH studies 118

5.2.2 Voltammetric analyses 120

5.2.2.1 Kinetic studies on nitrite-electrode interactions 123

5.2.2.2 Stability studies 126

5.2.3 Interference studies 127

5.2.4 Chronoamperometric analyses 128

5.2.4.1 Limits of detection 128

5.2.4.2 Catalytic rates 132

5.3 Summary of chapter 132

CHAPTER 6 134

6. General conclusions, future prospects and recommendations 135

6.1 General conclusions 135

6.2 Future prospects and recommendations 135

REFERENCES 137

APPENDIX 157

LIST OF SYMBOLS

Symbol	Definition
α	Non-peripheral
β	Peripheral
ΔE_p	Difference in the peak anodic and peak cathodic potential
E_p	Peak oxidation potential
I_p	Peak catalytic current/peak background corrected current
Γ	Surface coverage
R_{CT}	Resistance-to-charge

LIST OF ABBREVIATIONS

Abbreviation	**Description**
ACN	Acetonitrile
CFE	Carbon fibre electrode
CT	Charge transfer
CPE	Carbon paste electrode
DBU	1,8-Diazabicyclo(5.4.0)undec-7-ene
DCC	Dicyclohexyl carbodiimide
DCM	Dichloromethane
DLS	Dynamic light scattering
DMAP	4-Dimethylaminopyridine
DMF	*N,N*-Dimethylformamide
DMSO	Dimethyl sulfoxide
EDC	1-Ethyl-3-(3-dimethylaminopropyl)-carbodiimide
EIS	Electrochemical impedance spectroscopy
FT-IR	Fourier-transform infrared
GCE	Glassy carbon electrode
gCNQDs	Graphitic carbon nitride quantum dots
GCP	Glassy carbon plate
GE	Graphite electrode
GQDs	Graphene quantum dots
H_2Pc	Metal-free phthalocyanine
HER2	Human epidermal growth factor receptor 2

HOMO	Highest occupied molecular orbital
ICT	Intramolecular charge transfer
LUMO	Lowest occupied molecular orbital
MWCNTs	Multi-walled carbon nanotubes
NHS	N-Hydroxysuccinimide
ORR	Oxygen reduction reaction
Pc/MPc	Phthalocyanine/metallophthalocyanine
PDT	Photodynamic therapy
PPh_3	Triphenylphosphine
PPY	Polypyrrole
PSA	Prostate specific antigen
RT	Room temperature
SPCE	Screen-printed carbon electrode
SWCNTs	Single-walled carbon nanotubes
$TBABF_4$	Tetrabutylammonium tetraborofluorate
TEA	Triethylamine
TEM	Transmission electron microscopy
THF	Tetrahydrofuran
TX	Triton X-100
XPS	X-ray photoelectron spectroscopy

CHAPTER 1

INTRODUCTION

This chapter is based on the existing literature pertaining to graphene quantum dots, phthalocyanines and their use in electrocatalysis. In addition to the phthalocyanines that have been previously reported, an outline of the phthalocyanines used in this thesis is also provided.

1. Introduction

1.1 Catalysis – Electrocatalysis

Catalysis is defined as the acceleration of a chemical reaction by means of a catalyst [1]. The classification of catalysis is, in most cases, based on the state of the material serving as the catalyst [2-4]. The categories of catalysis are homogeneous, heterogeneous and autocatalysis where in homogeneous catalysis, the catalyst exists in the same state or phase of matter as the reactants, in heterogeneous catalysis, the catalyst is in a different phase and in terms of autocatalysis, there is no catalyst added, instead one of the products serve as a catalyst themselves [2-4].

In electrochemistry, the most favourable type of catalysis is heterogeneous catalysis which involves the immobilization of an electrocatalyst onto a working electrode [5]. The combination of catalysis and electrochemistry is referred to as electrocatalysis and is applied in the detection of substances through electrochemical processes [6]. The widespread use of catalysts in electrochemistry has been largely driven by the desire to improve the selectivity of bare/unmodified electrodes [6]. In addition to improving the selectivity, electrode modification has been found to enhance the sensitivity of the electrode, reduce the overpotential as well improve on the stability of the surface which are all considered traits of a good or desirable electrocatalyst [6-11]. An example of how electrode modification improves the electrochemical response of an electrode is shown in **Fig. 1.1** where it can be observed that the modified electrode, in comparison to the bare electrode, elicits a better peak current response at a lower oxidation potential [9].

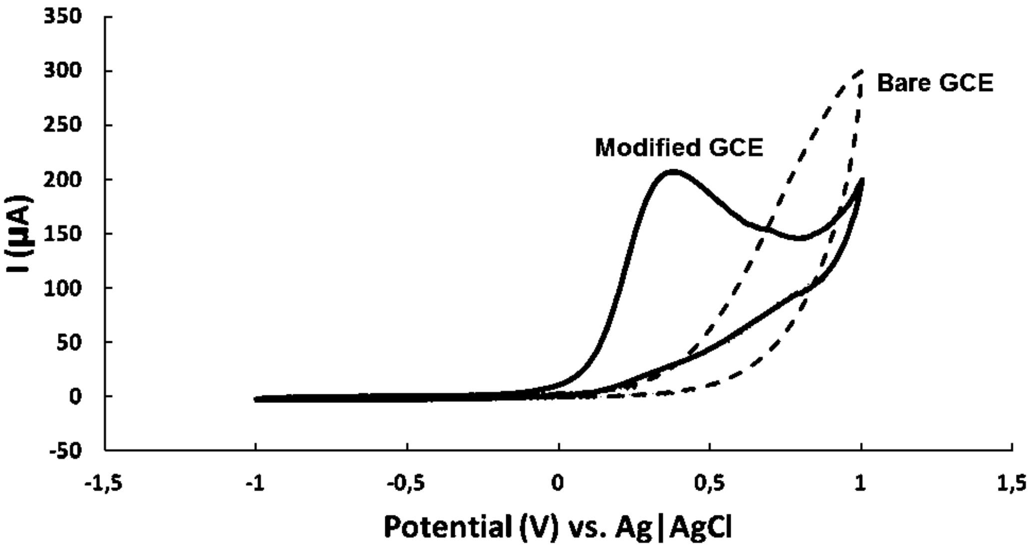

Fig. 1.1: Cyclic voltammograms for a bare GCE (dashed line) and a modified GCE (solid line) in 0.2 M NaOH containing 6 mM of hydrazine [9].

With respect to the electrodes available, there are several options including electrodes fashioned from noble metals such as platinum and gold as well as those derived from non-metals such as carbonaceous electrodes [12,13]. Of the materials mentioned, carbon-based electrodes have shown signs of being the most favourable as they are sourced from a naturally occurring substance that exists in great abundance. Unlike metal-based electrodes, carbon electrodes possess great mechanical flexibility in that the fabrication thereof can be achieved in different ways which in turn influences the arrangement of the carbon atoms in space [13]. Examples of these include carbon paste electrodes (CPEs), graphite electrodes (GEs), screen-printed carbon electrodes (SPCEs), glassy carbon electrodes (GCEs) and carbon fibre electrodes (CFEs) [10,14,15].

Of the aforementioned electrodes, the glassy carbon electrode (GCE) was selected as the most suitable as it is highly conductive and has a non-porous surface [16]. In comparing it to the gold, platinum and other carbon electrodes, namely the CPE and SPCE, as showcased in **Table 1.1**, it is evident that the GCE is marked by more positive attributes than the other electrodes [10,12,16-24].

Table 1.1: Advantages and disadvantages/limitations of common electrodes in existence.

Type of electrode	Advantages	Limitations
CPE	• Inexpensive • Wide potential range • Low background current (good filter)	• Unstable in organic solvents
SPCE	• All three electrodes including reference, counter and working electrode on a single platform • Portable and disposable • Fairly inexpensive	• Confined to flat surfaces
GCE	• Inexpensive • Wide potential range • Low oxidation rate • High chemical stability and inertness	• Susceptible to fouling/passivation
Pt	• Can exist as an alloy with rhodium (more rigidity) • Available as a wire, flat plate, or tube	• Expensive • Limited cathodic potential range
Au	• Extensive cathodic potential range • Available as a wire, flat plate, or tube	• Expensive • Susceptible to surface oxidation (reduces anodic window)

Despite presenting seemingly ideal properties, the GCE is not always responsive to analytes or target compounds. It is for this reason that there is a need to modify/alter the electrode surface through the introduction of conductive materials with the intention of enhancing the signal output [20,25-27]. Surface modification can be achieved through adsorption (dip-dry/drop-dry), electropolymerization, covalent means or click chemistry amongst others [10,28].

The methods in which an electrode is modified depend on the type of modifier as well as the type of electrochemical techniques that are to be applied. Drop-drying and dip-drying are variations of modification through adsorption where the former entails dropping an aliquot of the electrode modifier or electrocatalyst onto the electrode surface and allowing it to dry whilst the latter involves the immersion of the electrode into a solution of the electrocatalyst, removing it from the solution and leaving it to dry (an illustration of drop-drying is provided in **Fig. 1.2**) [29,30].

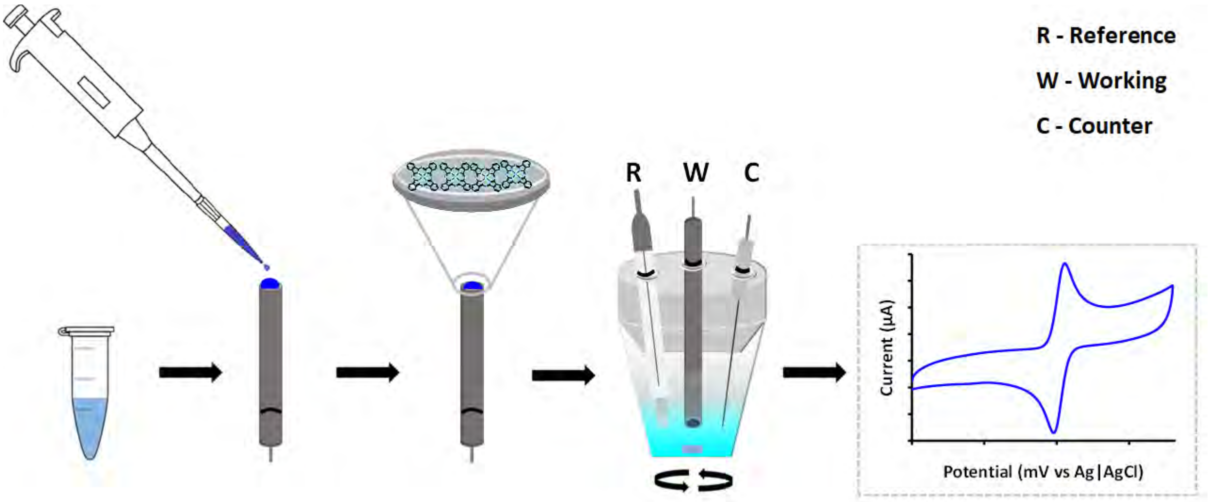

Fig. 1.2: Schematic diagram of how drop-drying takes place with the subsequent use in a three-electrode electrochemical system.

Electropolymerization and grafting are similar in that they require the use of a complete three-electrode system composed of the working electrode, reference and counter electrode and a potentiostat. Electropolymerization of an electrode involves performing multiple cyclic voltammetric scans over a specified potential range. What is of importance in this case is that the electrocatalyst must possess functional groups that allow for the electropolymerization to take place (e.g. -NH_2) [30]. In terms of modification by covalent means, grafting is sometimes followed by the introduction of a secondary material either through a Schiff base reaction or a Sharpless copper-catalysed cycloaddition reaction [31-34]. The procedure usually involves the reduction of a diazonium salt where the radicals produced bind to the electrode surface (which in essence is grafting), with the result being a modified surface that possesses functional groups to facilitate the addition of the desired electrocatalyst (**Fig. 1.3**) [34].

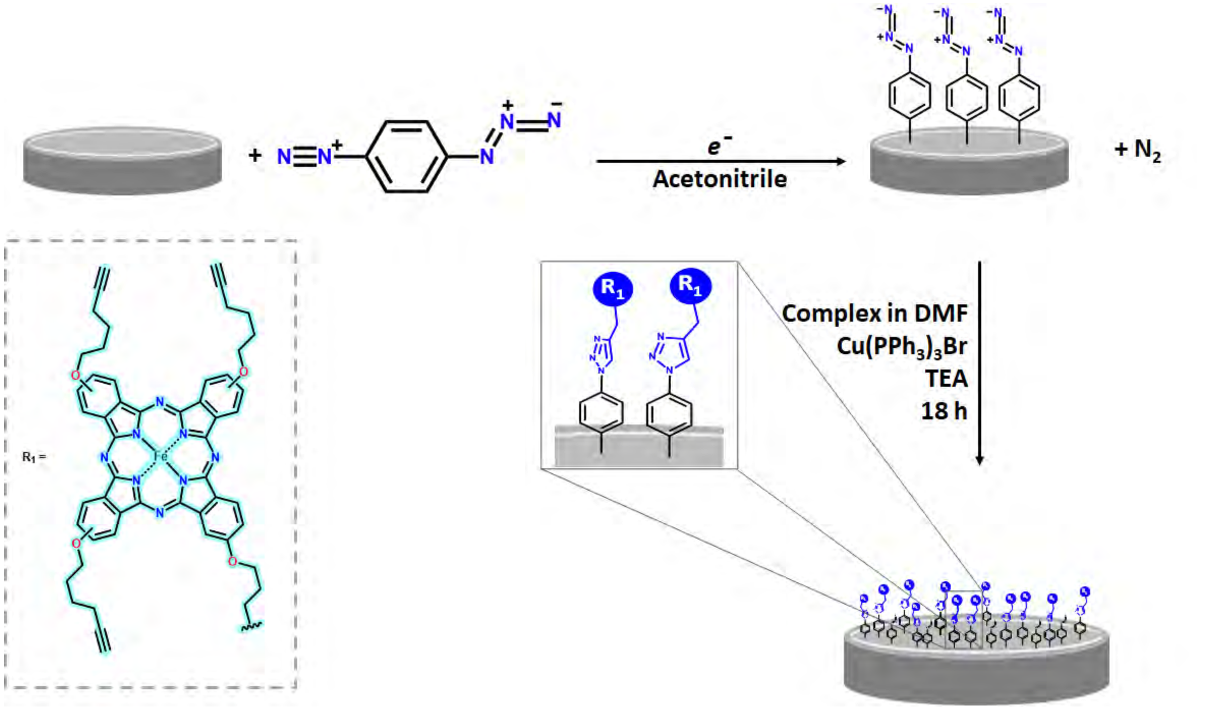

Fig. 1.3: Illustration of a click chemistry reaction involving an alkyne-substituted iron Pc. (DMF = *N,N*-dimethylformamide; $Cu(PPh_3)_3Br$ = bromotris(triphenylphosphine)copper(I); TEA = triethylamine).

The work presented in this thesis involves modification of a glassy carbon electrode using two of the methods described, adsorption through drop-drying as well as modification through click chemistry. The materials used in doing so are graphene quantum dots (GQDs) and phthalocyanines (Pcs). In the following sections, a brief introduction on GQDs will be provided followed by an extensive account on Pcs as they are the primary electrocatalysts of interest.

1.2 Graphene quantum dots (GQDs)

1.2.1 Overview

Graphene quantum dots (GQDs) are nanosized particles derived from graphene, a 2-dimensional (2D) material composed of sp^2-hybridized carbon atoms arranged in the form of a honeycomb [35,36]. Unlike graphene in its bulk state, GQDs are fluorescent and highly soluble in a variety of solvents [37-39]. These properties enable GQDs a wider reach in terms of applications (e.g. photocatalysis, biomedicine, the fabrication of solar cells and sensors, etc.) as they present these properties whilst retaining those of bulk graphene such as high thermal and mechanical stability [40-43]. Furthermore, relative to their semiconductor quantum dot counterparts that are derived from cadmium, selenium and tellurium, GQDs have no known/reported history of being toxic [42,44,45]. And beyond being able to be adapted for specific applications through the inclusion of heteroatoms (referred to as "doping"), and the amendments in functional groups and sizes, carbon-based nanomaterials have been found to be highly biocompatible [40-42,46].

1.2.2 Synthesis

The synthesis of GQDs, inspired by a desire to possess certain chemical and photoluminescent properties which is influenced primarily by the starting materials, is classified into two categories, top-down and bottom-up methods [**47**,**48**]. As the terms suggest, one approach entails moving from the top towards the bottom whilst the other involves moving in an upward trajectory to achieve a certain outcome (**Scheme 1.1**).

GQDs generally exist in the size range of 2 – 20 nm and as the top-down term implies, the synthesis of GQDs in this manner involves downsizing of large or bulk carbon-based precursors into the nanosized particles [**47**,**49**]. Common carbon precursors employed in the top-down synthesis of GQDs include graphite, coal, single-walled carbon nanotubes (SWCNTs), multi-walled carbon nanotubes (MWCNTs), graphene oxide and naturally, graphene itself [**47**]. In attaining the GQDs, these materials are exposed to extreme chemical and/or mechanical conditioning such as chemical exfoliation, laser ablation, hydro- and solvothermal as well as electrochemical treatments [**47**,**50**,**51**].

In most cases, the method chosen is based not only on the carbon precursor but on the desired outcome as well in terms of size and surface functionalization. The most frequently reported methods of synthesizing GQDs are the hydro- and solvothermal routes [**47**]. The only difference between the two methods is that one makes use of water as the solvent (hydrothermal) whilst the other favours organic solvents more (solvothermal). In both instances, there is a carbon source, the application of elevated temperatures that exceed 150 °C and a closed, high-pressure system [**47**].

The bottom-up approach to synthesizing GQDs, as the term suggests, is the opposite of the top-down method. Bottom-up synthesis of GQDs involves the use of small carbon-rich precursors such as glucose, sucrose, and citric acid [**47**,**51**,**52**]. These are also subjected to high temperatures (i.e. pyrolysis) with the difference being instead of reducing a bulk material into a smaller one, small molecules are used to build the GQDs to the desired size range. Some advantages that the bottom-up approach has over the top-down method is that there is more control over the size and functionalization of the GQDs, and more importantly, because there is greater specificity in the precursors, the GQDs derived from a bottom-up approach present less structural defects in comparison to their top-down counterparts [47].

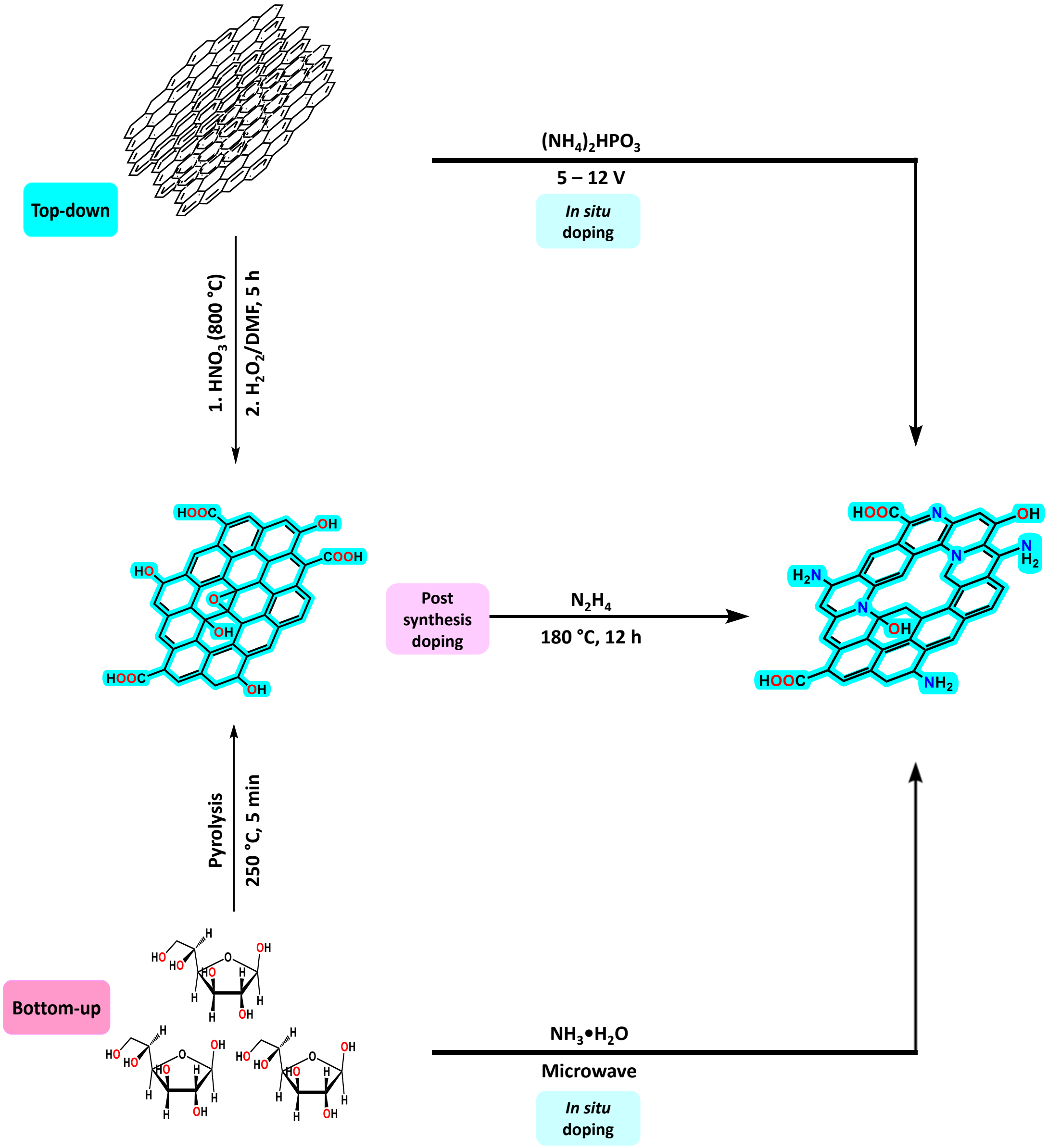

Scheme 1.1: An illustration of the top-down and bottom-approaches towards the synthesis of pristine GQDs and nitrogen-doped GQDs (NGQDs). (DMF = *N,N*-dimethylformamide).

An additional “synthetic pathway”, not entirely a standalone method, is that of doping. Naturally, GQDs are rich in oxygen-bearing functional groups, groups such as carboxylic acids and hydroxyls which can be oxidized or reduced as desired [49]. In order to improve on the natural properties of GQDs, atoms such as nitrogen, sulphur, fluoride, and boron are introduced into the graphene network which is referred to as doping [51,53,54]. Doping, an act achievable *in situ* or post-synthesis, has been demonstrated to improve the photoluminescence and electrochemical properties of GQDs [50]. Some of the synthetic pathways applied in the synthesis of doped GQDs are demonstrated in **Scheme 1.1** where both the top-down and bottom-up approaches are shown along with one-pot (*in situ*) doping as well as post-synthesis doping of the pristine GQDs [47,51,52,55].

One particular heteroatom that has garnered a great deal of favour in doping is nitrogen. Nitrogen possesses a similar size to carbon and so its incorporation into the graphene carbon network hardly presents significant distortions, with a large portion of the matrix retaining its network of sp^2-hybridized carbons, which is an important aspect in the formation of non-covalent composites [39,50]. While the introduction of nitrogen into GQDs can be performed on the peripheral ends of the GQDs, the GQDs used in this work are composed of nitrogen as a contributor to the graphene lattice. The inclusion of nitrogen in the graphene network brings forth different types of nitrogen atoms which all have an influence on the performance of the GQDS. The types of nitrogen observable in nitrogen-doped GQDS (NGQDs) include pyridinic, pyrrolic, and graphitic nitrogen(s) [39,50]. The work reported herein makes use of NGQDs in conjunction with phthalocyanines for electrocatalysis.

1.3 Phthalocyanines

1.3.1 Structure and general applications

Phthalocyanines (Pcs) are synthetic dyes characterized by an intense Q-band absorption in the ultraviolet spectrum nearing the infrared region (~650 nm or higher) [56]. Similar to their naturally occurring analogues, porphyrins, Pcs are highly conjugated macrocycles composed of an 18-π electron system within the main framework (**Fig. 1.4**) [57]. At present, most Pcs possess a metal or metalloid in the central cavity, which is a significant difference from the metal-free Pc (H_2Pc) [58,59]. In addition to the cavity's ability to host a multitude of transition metals and metalloids, the flexibility through substitution of the hydrogen atoms in the alpha (α) and/or beta (β) positions has seen Pcs gain traction in various fields of application (**Fig. 1.4**) [58,60].

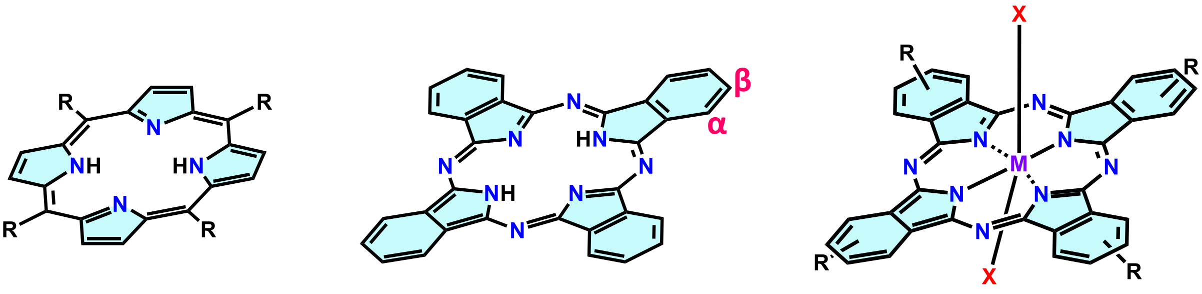

Porphyrin

Free-base phthalocyanine (H_2Pc)

Metallophthalocyanine (MPc)

Fig. 1.4: General structures of a porphyrin, a free-base phthalocyanine (H_2Pc) and a metallophthalocyanine where R represents the substituents, M the central metal and X the axial ligand.

Metallophthalocyanines (MPcs) containing diamagnetic metals have been reported to be efficient photosensitizers in photodynamic therapy (PDT) [60,61]. Cobalt, iron and manganese-bearing MPcs have found favour in electrocatalysis due to their incompletely occupied d-orbitals [62-64]. In addition to electrocatalysis and biomedicine through PDT, other fields that have sought to exploit the electronic and mechanical properties of Pcs/MPcs include optics (non-linear optics as optical limiters), energy conversion in the fabrication of dye-sensitized solar cells and the near infrared region (NIR) absorbers [60-67].

1.3.2 Synthesis

1.3.2.1 Symmetric phthalocyanines

The first phthalocyanine was synthesized accidentally in 1907 where 2-cyanobenzamide was subjected to high temperatures to produce a metal-free phthalocyanine (H_2Pc) [58]. Further knowledge through attempts at synthesizing the blue pigment has seen the synthesis of Pcs evolve where other precursors such as phthalic acid, phthalimide and 1,3-diiminoisoindole have been used (**Scheme 1.2**) [68-70]. In environments that require the product to be of an even higher purity, phthalonitriles have been the more favourable choice [68]. The general synthesis of a Pc entails the refluxing of the organic precursor as demonstrated in **Scheme 1.2**, in a solvent that possesses a high boiling point. To obtain the metalated phthalocyanine, the same protocol is followed with the difference being the inclusion of a metal salt and a base that serves as the catalyst (to deprotonate the internal hydrogen atoms) [68-70].

Substitution of Pcs on the peripheral (beta) and/or non-peripheral (alpha) positions often induce significant changes in the electronic transitions as observed in the absorption spectra through hypsochromic or bathochromic shifts [71,72]. To a certain degree, the type of substituents employed result in spectral changes but often, substitution on the alpha position induces more notable bathochromic shifts [73]. Other substituents such as *tert*-butyl groups, although unlikely to induce spectral shifts, have been found to improve the overall solubility of the Pc molecule(s) [74]. The choice in central metal as well as the insertion of axial ligands has also been shown to induce not only spectroscopic changes but how the molecules function or behave as well [67].

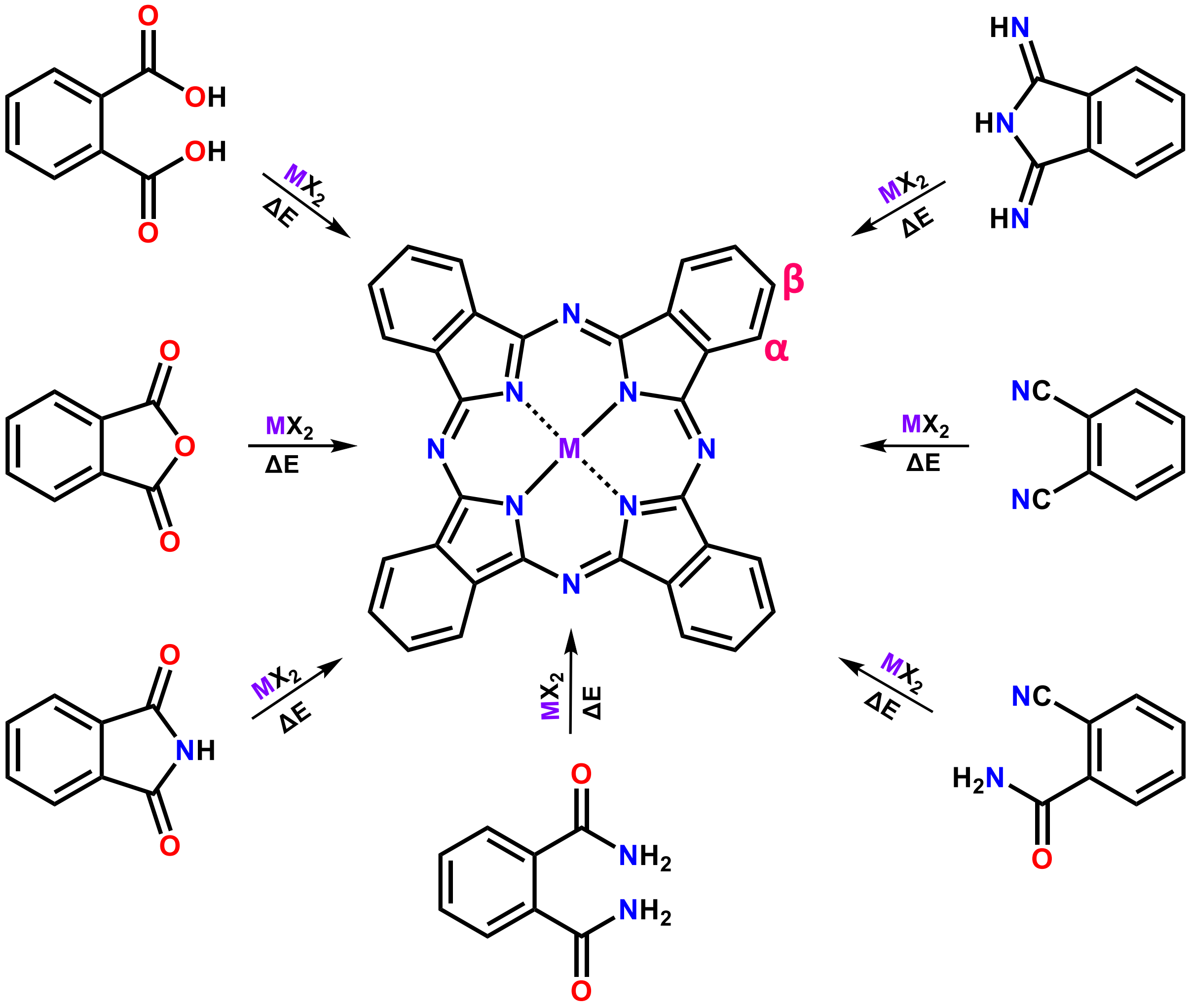

Scheme 1.2: An illustration of how a phthalocyanine can be synthesized from different precursors where M in MX_2 represents the metal and X the complementary ion (e.g. Cl^-, CH_3COO^-, NO_3^-, etc.).

In addition to chemical and electronic/spectral changes, substitution of four ends on the periphery or non-peripheral ends, referred to as tetra-substitution, results in the production of regioisomers [75]. While the tetra-substituted Pcs are generally referred to as being symmetric (due to the uniformity in substituents), the regioisomers themselves demonstrate the different symmetries that can be observed (**Fig. 1.5**). Another factor which can alter the symmetry of a Pc is the central metal (or its absence). Based on its size, a metal can either fit into the central cavity or protrude from it rendering the overall molecule non-planar [76,77].

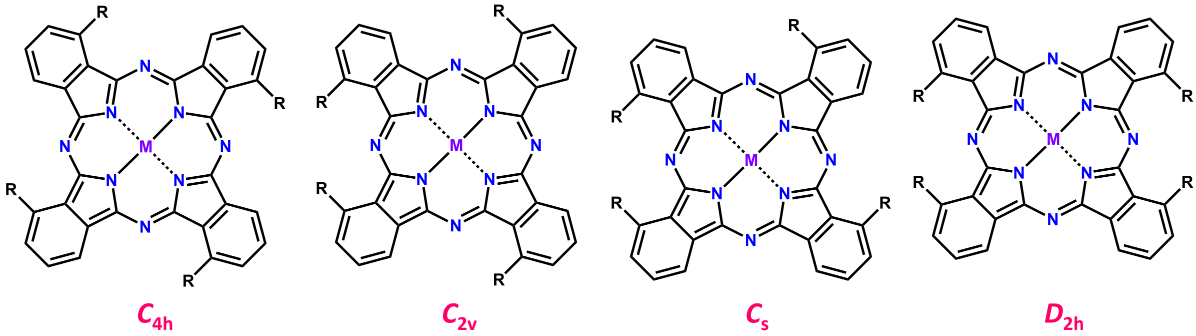

Fig. 1.5: Regioisomers illustrating the various symmetries assumed by a tetra-substituted MPc where R represents the substituent and M the central metal.

1.3.2.2 Asymmetric phthalocyanines

Asymmetric phthalocyanines, usually the A_3B/AB_3 type, are phthalocyanines that are composed of a different substituent or are unsubstituted on one out of the four isoindole units [68,78]. The common synthetic route for these kinds of Pcs is similar to that of symmetric Pcs with the difference being that it entails the use of two phthalonitrile derivatives rather than one [68]. The method undertaken is referred to as the statistical condensation method where the ratios of the phthalonitriles are unequal [78]. The most common ratios reported include 1:3, 1:5 and in some instances, 1:9 or more. In most cases, the synthesis of A_3B/AB_3 Pcs is often accompanied by the formation of the symmetric (A_4/B_4) analogues as side products. Other possible side products include A_2B_2 and ABAB Pcs which accounts for the poor yields reported for the target compounds as demonstrated in **Scheme 1.3** [78,79].

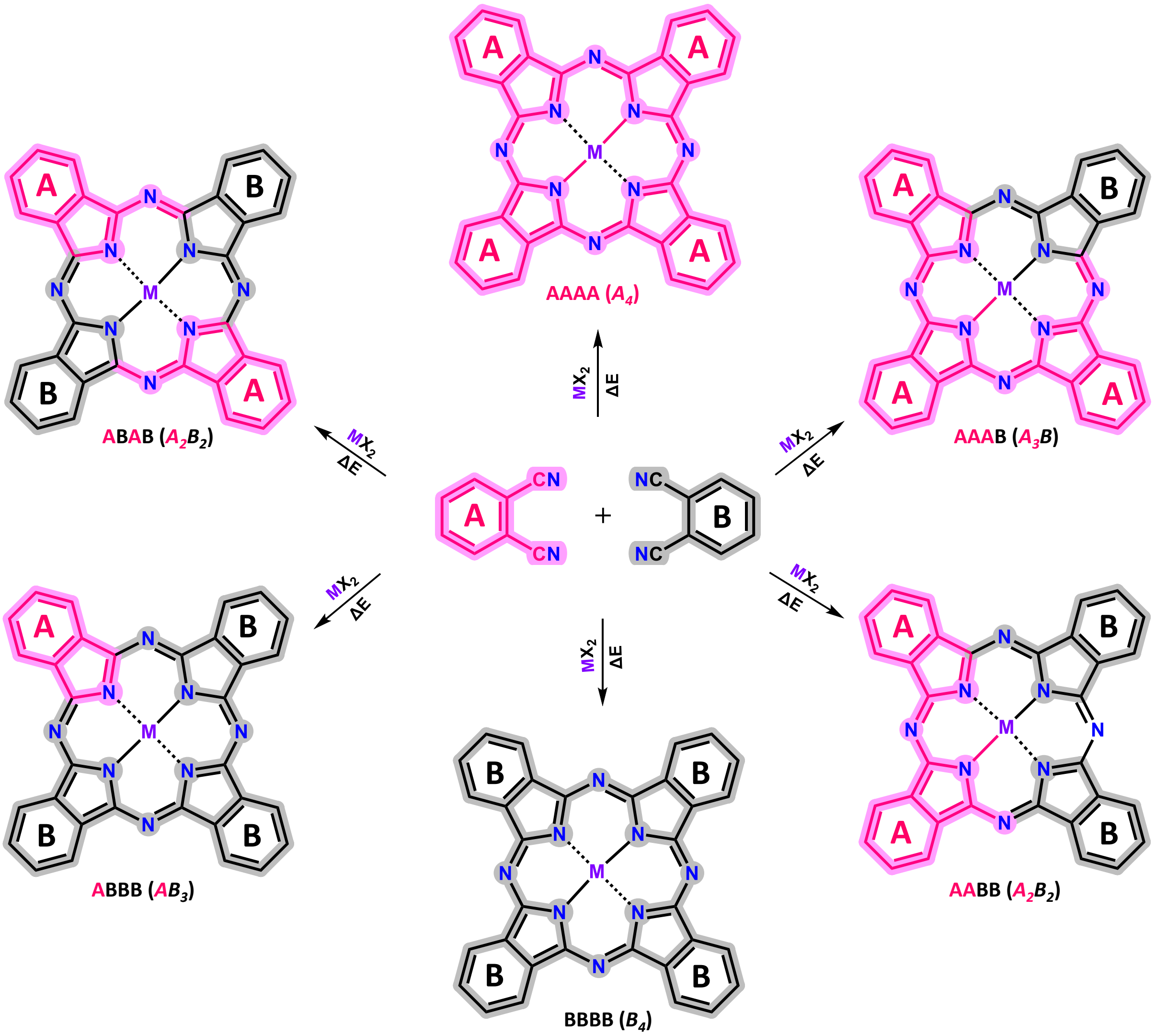

Scheme 1.3: Synthetic route for asymmetric Pcs (A$_3$B/AB$_3$-type) and the possible side-products where M in MX$_2$ represents the metal and X the complementary ion (e.g. Cl$^-$, CH$_3$COO$^-$, NO$_3^-$, etc.).

One alternative to improving the yield by limiting the number of side-products formed is through the ring expansion of a subphthalocyanine (**Scheme 1.4**). Subphthalocyanines are a variation of Pcs composed of three isoindole units instead of four. While there are several advantages to this approach (i.e. higher yields and better selectivity), several factors such as the substituents, solvent and reaction time render this approach less viable as there is no "standardized" approach [79].

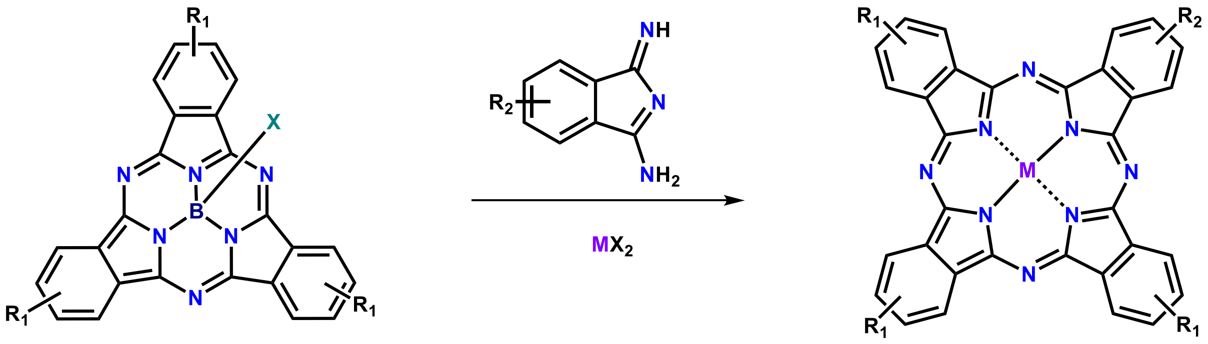

Scheme 1.4: Synthesis of an A_3B phthalocyanine through the ring expansion reaction of a subphthalocyanine where M in MX_2 represents the metal and X the complementary ion (e.g. Cl^-, CH_3COO^-, NO_3^-, etc.).

1.3.3 Electronic spectra of phthalocyanines

The electronic spectra of Pcs, in the case of metalated Pcs, is marked by the appearance of two distinct absorption bands, the Q-band and the B-band (**Fig. 1.6**). The Q-band, as seen in **Fig. 1.6**, is generally observed in the visible region from approximately 650 nm or higher [56]. Its position, however, can be altered through variations in the point of substitution (alpha or beta position), the substituents themselves, the central metal as well as conjugation to other materials, through covalent or non-covalent means [67,72,80,81]. The Soret band, generally referred to as the B-band, is often observed at wavelengths below 400 nm (approx. 340 nm) and is usually of a lower intensity than the Q-band. In explaining the appearance of both the Q and B-bands, Gouterman's four orbital model has been considered the most appropriate [82]. According to the theoretical calculations, the Q-band is a result of transitions from the a_{1u} level at the highest occupied molecular orbital (HOMO) to the e_g level of the lowest unoccupied molecular orbital (LUMO). The B-band on the other hand, is caused by transitions from the b_{2u} and a_{2u} levels at the HOMO to the e_g level within the LUMO (**Fig. 1.6 inset**). Due to the proximity of the b_{2u} and a_{2u} energy levels, the observation of a single broad B-band due to an electronic overlap is considered a norm. Both the Q-band and B-band(s) are the result of π → π* transitions that occur within the ring system [68,82]. Charge transfer (CT) bands are the result of ligand-to-metal or metal-to-ligand charge transfer and are sometimes observable between the B- and Q-bands as seen in **Fig. 1.6**. This charge transfer is ascribed to the position of the d-orbitals from the central metal where they find themselves situated in between the HOMO and LUMO of the Pc's main framework [83-86].

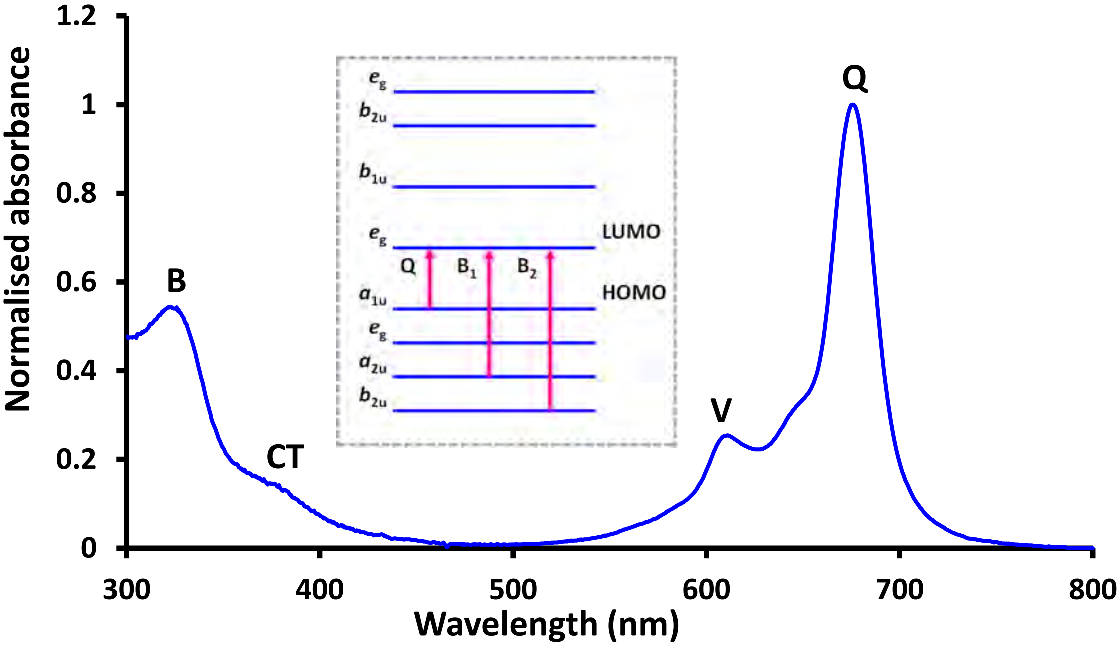

Fig. 1.6: Absorption spectra of a tetra-substituted diethylamino-phenoxy cobalt Pc in DMF where **B** is the B-band, **CT** the charge transfer band, **V** the vibronic band and **Q**, the Q-band.

1.3.4 Redox behaviour of phthalocyanines

An understanding of the electrochemical processes that take place in Pcs is important as it can aid in the expansion of how these macrocycles are applied. Historically, the characterisation of Pcs has been focused predominantly on the spectral characterisation however, this has changed significantly over the years with electrochemical characterisation also being recognized as an important aspect in the overall characterisation of Pcs [87,88].

In understanding the redox processes that take place in Pcs, an electrochemical assessment is performed. Such assessments entail the use of simple electrochemical techniques such as differential pulse or cyclic voltammetry (example using cyclic voltammetry is provided in **Fig. 1.7**) [89-91].

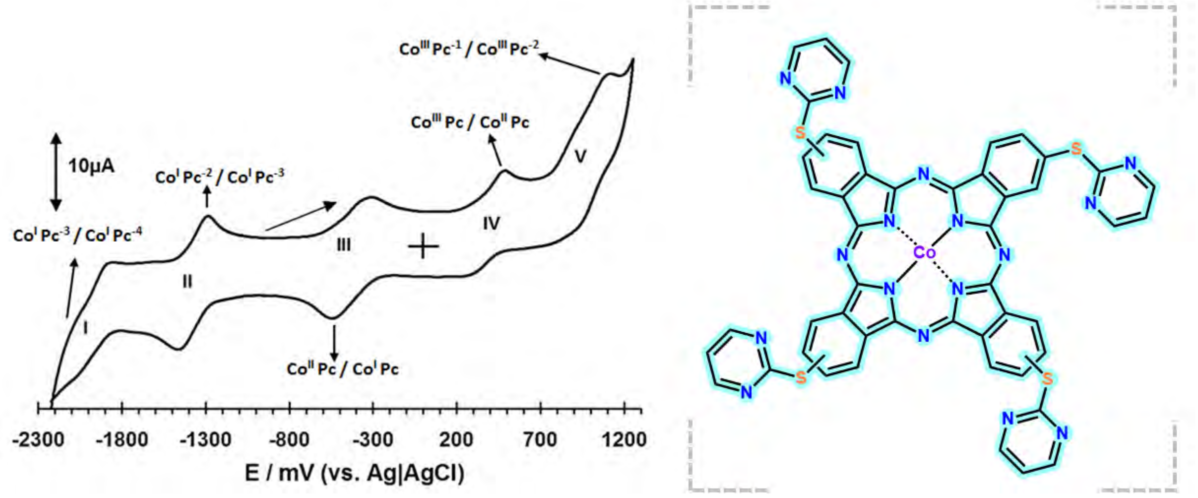

Fig. 1.7: A cyclic voltammogram of a tetramercaptopyrimidine cobalt Pc in *N,N*-dimethylformamide (DMF), in 0.1 M of tetrabutylammonium tetrafluoroborate ($TBABF_4$) [91].

At the very least, Pcs can undergo six electrochemical processes attributed solely to the ring system [87,91,92]. Out of the 6, 4 are attributed to the addition of electrons to the e_g level (LUMO) orbitals whilst 2 undergo oxidation from the a_{1u} orbitals (HOMO) [93]. Other factors that may influence the redox behaviour of Pcs include the nature of the substituents; the type of solvent used in the electrochemical assessment as well as the central metal [94,95].

1.3.5 Phthalocyanines in electrocatalysis

A substantial amount of research regarding the use of Pcs in electrochemical sensing has been conducted. In this section of the thesis, some of the Pcs involved in electrocatalysis (in conjunction with GQDs and/or similar materials) are outlined along with the analytes and/or electrochemical reactions involved (**Table 1.2**) [**96**-**104**].

Table 1.2: A selection of some MPcs/Pcs used in electrocatalysis in conjunction with graphene quantum dots.

Phthalocyanine	Central metal and R groups		Electrode modification/supporting material	Analyte(s)	Ref.
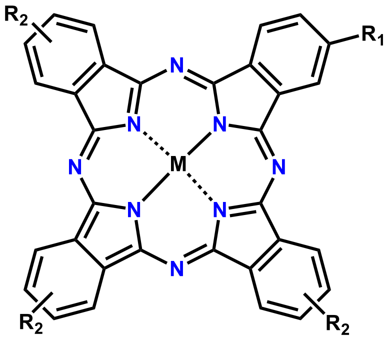	M = Co(II), R_1 = 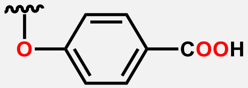	R_2 = None	Drop-dry (with GQDs)	Hydrazine	[96]
	M = Co(II), R_1 = 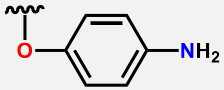	R_2 = 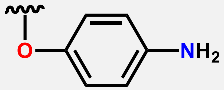			
	M = Co(II), R_1 = 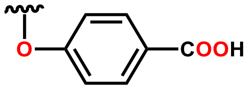	R_2 = 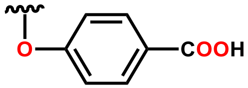	Drop-dry (with GQDs, SNGQDs and PPY)	HER2 and hydrazine	[96,97]
	M = Co(II), R_1 = 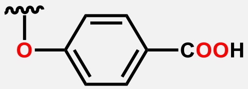	R_2 = 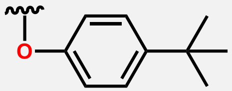	Drop-dry (with rGQDs, NH_2GQDS and NGQDs)	Hydrazine	[98,99]
	M = Co(II), R_1 = 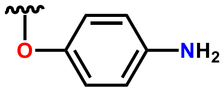	R_2 = 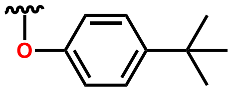	Drop-dry (with NGQDs)	Hydrazine	[99]

Table 1.2 continued:

Phthalocyanine	Central metal and R groups		Electrode modification/supporting material	Analyte(s)	Ref.
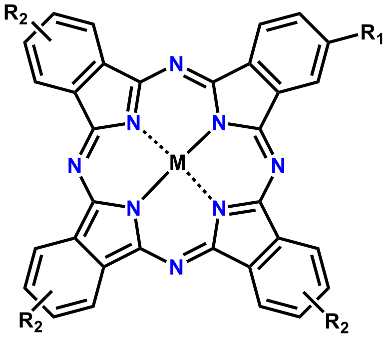	M = Co(II), R_1 = 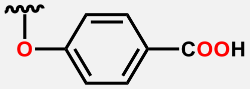	R_2 = 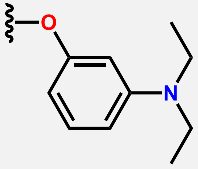	Drop-dry (with NGQDs)	Hydrazine	[99]
	M = Co(II), R_1 = 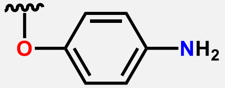	R_2 = 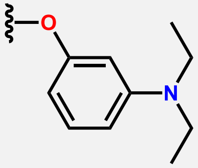			
	M = Co(II), R_1 = 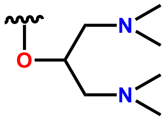	R_2 = 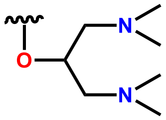	Drop-dry (with NGQDs)	Dopamine	[100]

Table 1.2 continued:

Phthalocyanine	Central metal and R groups		Electrode modification/supporting material	Analyte(s)	Ref.
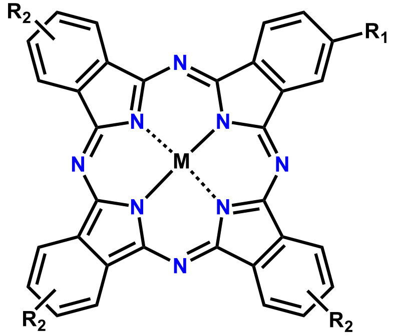	M = Co(II), R_1 = 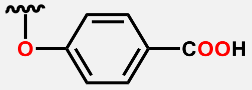	R_2 = 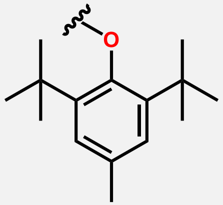	Drop-dry (with gCNQDs and GQDs)	L-cysteine and PSA	[101,102]
	M = Co(II), R_1 = 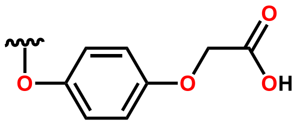	R_2 = 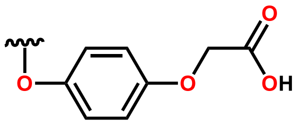	Drop-dry (with GQDs)	Hydrazine	[103]
	M = Fe(III), R_1 = None	R_2 = None	Drop-dry (with NH_2GQDs)	ORR	[104]

gCNQDs – Graphitic carbon nitride quantum dots; GQDs – graphene quantum dots; SNGQDs – sulphur and nitrogen co-doped graphene quantum dots; PPY – polypyrrole; rGQDs – reduced graphene quantum dots; NH_2GQDs – amino-functionalized graphene quantum dots; NGQDs – nitrogen-doped graphene quantum dots; HER2 – human epidermal growth factor receptor 2; PSA – prostate specific antigen; ORR – oxygen reduction reaction.

An important observation that can be made from looking at the Pcs presented in **Table 1.2** is that significant strides regarding the use of asymmetric Pcs in electrocatalysis have been made. And while that is the case, there remains a lack of uniformity in terms of the trends observed when comparing symmetric to asymmetric Pcs as some techniques suggest that the former are better whilst other techniques imply that the latter offer more desirable responses relative to their symmetric analogues [100]. An additional observation made from **Table 1.2** with respect to the asymmetric Pcs is that the coupling of substituents involves both electron-donating and electron-withdrawing functional groups which induces a push-pull effect (intramolecular charge transfer, ICT) [98-101,105-107].

Based on the observations outlined, it is evident that there are significant gaps in the literature pertaining to phthalocyanine-based push-pull systems in that the design thereof is to a certain degree, one-dimensional (i.e. alkyl substituents are coupled with a benzoic acid substituent), with a limited consideration for other acid-based derivatives. Furthermore, with the general approach being such that the A_3 component is composed of alkyl groups whilst the B in A_3B possesses the carboxylic acid, the desire to introduce secondary nanomaterials such as quantum dots or nanotubes through covalent means often presents the challenge of a Pc no longer retaining its ability to function as a push-pull system (or doing so but at a reduced level). The work presented in this thesis aims to address some of the current shortcomings that exist in the literature, and these are:

- Proof of concept – not all asymmetric Pcs fare better than their symmetric analogues.
- An attempt at establishing the ideal combination of substituents as far as asymmetric Pcs are concerned.

- Preservation of the push-pull effect whilst conjugating to NGQDs as they have shown to be good complementary materials in electrocatalysis (**Table 1.2**).
- Preservation of the push-pull effect whilst anchoring the Pc onto the electrode surface through click chemistry.

The fourth point is of great importance as while there are several Pcs that have been reported for electrocatalysis involving electrode modification through click chemistry, there are no accounts of such systems where the push-pull system is retained even after anchoring the Pc onto the electrode, which is one of the subjects explored in this work. **Table 1.3** provides a summary of alkyne-containing Pcs used in electrocatalysis with the majority being symmetrical in nature [9,34,64,108-113].

Table 1.3: Alkyne-functionaliized Pcs/MPcs for electrode modification through click chemistry.

Phthalocyanine	Central metal and R groups		Analyte(s)	Ref.
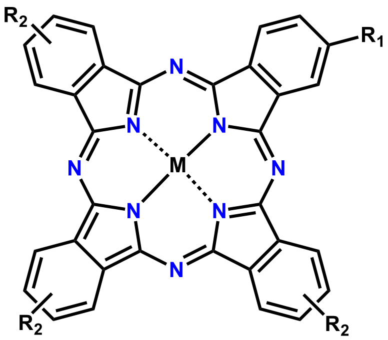	M = Mn(III), Fe(II), Ni(II) and Co(II) R_1 = 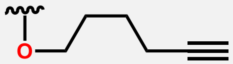	R_2 = 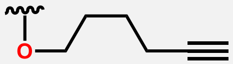	Hydrazine	[9,34,108]
	M = Mn(II), M = Mn(III)* and Co(II), R_1 = 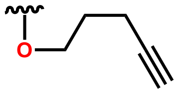	R_2 = 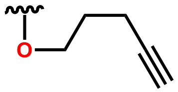	Eserine, diazinon, fenitrithion and ORR	[64,109-111]
	M = Co(II), R_1 = 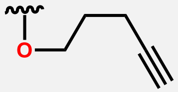	R_2 = 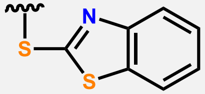	Hg^{2+}, Cu^{2+}, Pb^{2+} and Cd^{2+}	[112]
	M = Mn(III) and Co(II), R_1 = 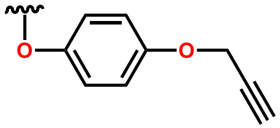	R_2 = 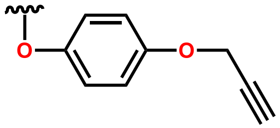	H_2O_2	[113]

*Alpha and beta tetra-substituted Pcs studied. ORR – oxygen reduction reaction.

1.3.6 Phthalocyanines reported in this thesis

In this thesis, the focus lies on substituted Pcs, both the symmetric and asymmetric variants. Previous reports have indicated that asymmetric Pcs possess better physicochemical properties than their symmetric counterparts [114,115]. However, it remains unknown as to whether this can be considered "true" for all asymmetric Pcs as there are multiple combinations of substituents that have not yet been explored. Based on the reasons outlined above, an explorative journey was undertaken where symmetric Pcs were compared to asymmetric Pcs.

The Pcs reported in this work are all new with the exception of complex **7** (**Table 1.4**) [116]. Furthermore, their application as electrocatalysts towards the electro-oxidation of hydrazine and nitrite is also investigated for the first time. The Pcs under study are classified into two groups, Pcs for the electrochemical sensing of hydrazine and those that were designed for the electrochemical sensing of nitrite (**Table 1.4**). The Pcs designed for the detection of hydrazine are composed primarily of alkyl-based substituents with the variation arising from the carboxylic acid-bearing substituent (complexes **1**-**5**). Regarding complexes **6** and **7**, the branched alkyl group (*tert*-butyl) was selected following the studies with the 15-carbon alkyl series having noted that the lengthy alkyl substituents in combination with cobalt as a central metal are met with a reduced/limited solubility in organic solvents.

The Pcs synthesized for the detection of nitrite possess paracetamol/acetaminophen as the dominant/primary substituent as it is composed of both electron-donating and electron-withdrawing groups that are situated within a close range, unlike the cardanol series (complexes **8**-**15**, **Table 1.4**) where the electron-donating and electron-withdrawing groups are further apart (which may hinder the desired push-pull effect).

With respect to the asymmetric component of the Pcs, the alkyne substituent was chosen to enable “clicking” onto the electrode surface. Furthermore, for the alkyne-containing Pcs (and their symmetric analogues), Pcs containing cobalt(II) and manganese(III) as central metals were synthesized. The amino substituent was selected for the purpose of forming a covalent bond to the NGQDs whilst Pcs with variations in the carboxylic acid substituent were also synthesized.

In summary, the Pcs were synthesized with the following purposes:

Pcs for hydrazine (complexes **1**-**7**)

- Evaluate the influence of varying the acid-bearing substituent.
- Evaluate the influence of reducing the chain length in the alkyl substituent.

Pcs for nitrite (complexes **8**-**15**)

- For the alkyne-containing Pcs, the methods of electrode modification were investigated in which adsorption was compared to covalent anchoring through click chemistry.
- The central metals were also compared against each other.
- For the amino-containing Pc, the inclusion of GQDs was studied in which the composites created through covalent means (amide bond) were compared to those created through non-covalent means (π-π interactions).
- In terms of the acid-containing Pcs, an assessment on varying the acid group was undertaken.

In each case, the asymmetric Pcs were compared with their symmetric counterparts. This was done to determine whether all asymmetric Pcs are better than symmetric Pcs or if there are occurrences where this is not the case.

Table 1.4: Phthalocyanines reported in this thesis.

Phthalocyanine	Complex name and number	R groups	Electrode modification / supporting material
	Hydrazine		
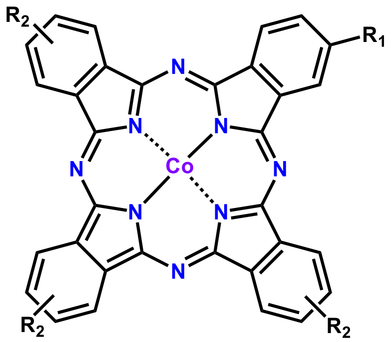	Tri-(3-pentadecylphenoxy)-mono-cinnamic acid cobalt(II) phthalocyanine, ***1*** (**new**)	R_1 = 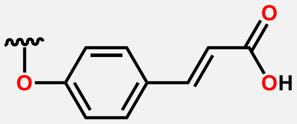 R_2 = 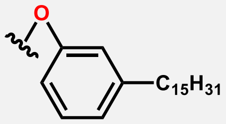	Drop-dry
	Tri-(3-pentadecylphenoxy)-mono-phenoxy acetic acid cobalt(II) phthalocyanine, ***2*** (**new**)	R_1 = 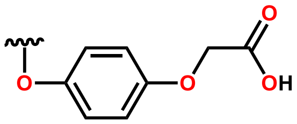 R_2 = 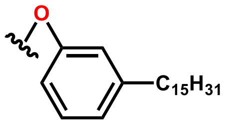	Drop-dry
	Tri-(3-pentadecylphenoxy)-mono-phenoxy propanoic acid cobalt(II) phthalocyanine, ***3*** (**new**)	R_1 = 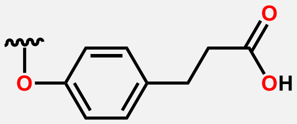 R_2 = 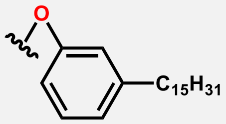	Drop-dry
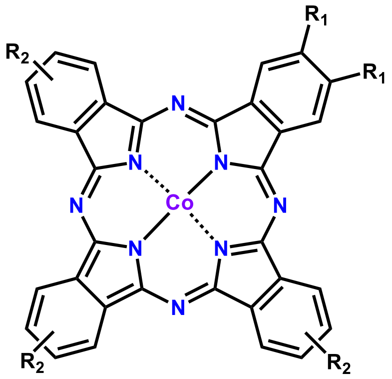	Tri-(3-pentadecylphenoxy)-mono-caffeic acid cobalt(II) phthalocyanine, ***4*** (**new**)	R_1 = 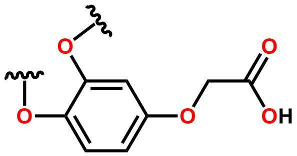 R_2 = 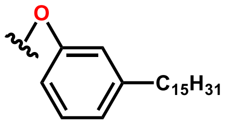	Drop-dry

Table 1.4 continued:

Phthalocyanine	Complex name and number	R groups		Electrode modification / supporting material
Hydrazine				
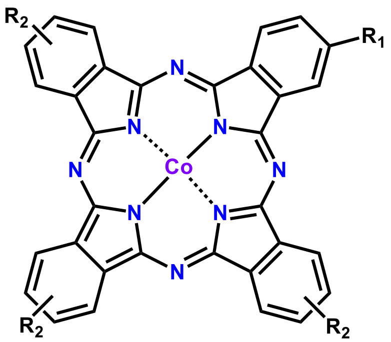	2,9,16,23-tetrakis-(3-pentadecylphenoxy) cobalt(II) phthalocyanine, ***5*** (**new**)	R_1 = 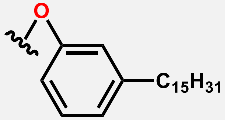	R_2 = 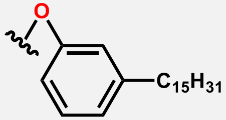	Drop-dry
	4-(tri-*tert*-butyl)-mono-phenoxy benzoic acid cobalt(II) phthalocyanine, ***6*** (**new**)	R_1 = 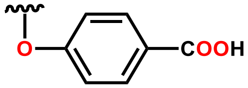	R_2 = 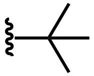	Drop-dry
	2,9,16,23-tetrakis-*tert*-butyl cobalt(II) phthalocyanine, ***7*** [116]	R_1 = 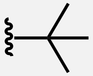	R_2 = 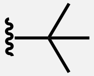	Drop-dry

Table 1.4 continued:

Phthalocyanine	**Complex name and number**	**R groups**		**Electrode modification / supporting material**
		Nitrite		
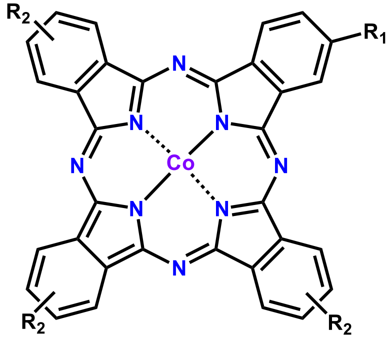	*Tris*-(4-acetamidophenoxy)-mono-(hex-5-yn-1-yloxy) cobalt(II) phthalocyanine, ***8*** (**new**)	R_1 = 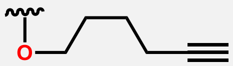	R_2 = 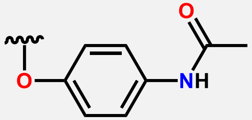	Drop-dry and covalent linking through click chemistry
	2,9,16,23-Tetrakis-acetamidophenoxy cobalt(II) phthalocyanine, ***9*** (**new**)	R_1 = 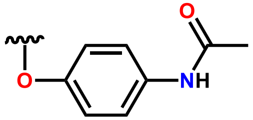	R_2 = 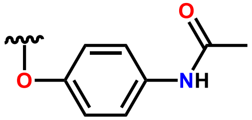	Drop-dry (with NGQDs)
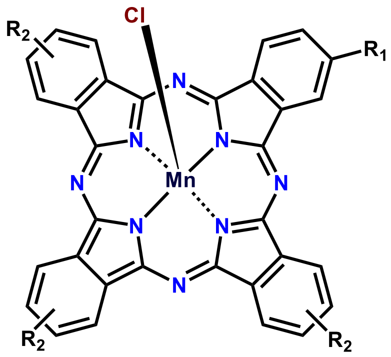	*Tris*-(4-acetamidophenoxy)-mono-(hex-5-yn-1-yloxy) manganese(III) chloride phthalocyanine, ***10*** (**new**)	R_1 = 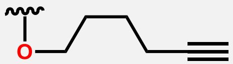	R_2 = 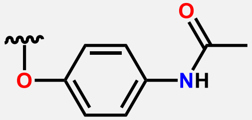	Drop-dry and covalent linking through click chemistry
	2,9,16,23-Tetrakis-acetamidophenoxy manganese(III) chloride phthalocyanine, ***11*** (**new**)	R_1 = 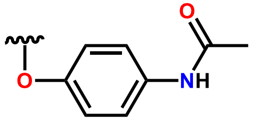	R_2 = 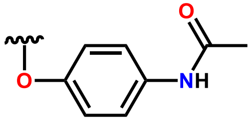	Drop-dry

Table 1.4 continued:

Phthalocyanine	Complex name and number	R groups		Electrode modification / supporting material
		Nitrite		
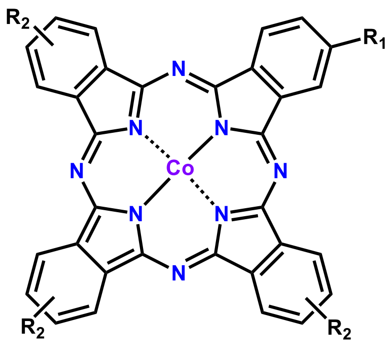	*Tris*-(4-acetamidophenoxy)-mono-aminophenoxy cobalt(II) phthalocyanine, ***12*** (**new**)	R_1 = 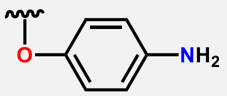	R_2 = 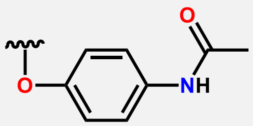	Drop-dry (with NGQDs)
	Tris-(4-acetamidophenoxy)-mono-phenoxy benzoic acid cobalt(II) phthalocyanine, ***13*** (**new**)	R_1 = 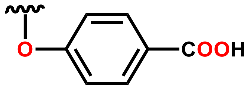	R_2 = 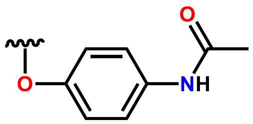	Drop-dry
	Tris-(4-acetamidophenoxy)-mono-phenoxy propanoic acid cobalt(II) phthalocyanine, ***14*** (**new**)	R_1 = 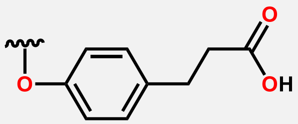	R_2 = 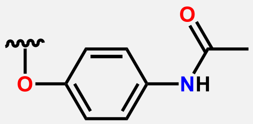	Drop-dry
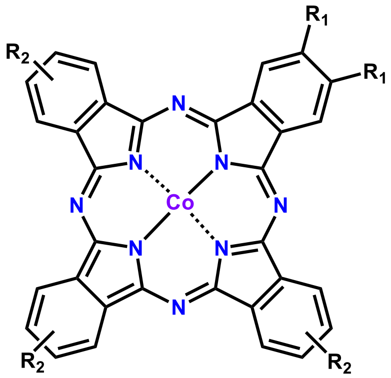	*Tris*-(4-acetamidophenoxy)-mono-caffeic acid cobalt(II) phthalocyanine, ***15*** (**new**)	R_1 = 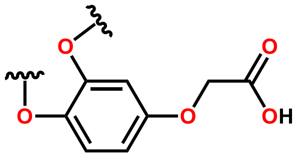	R_2 = 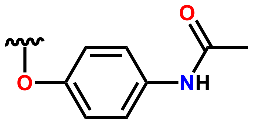	Drop-dry

1.4 Analytes

The efficiency of the Pcs as electrocatalysts was assessed using hydrazine and nitrite as test analytes (see **Fig. 1.8**). For hydrazine, the pentadecyl-based Pcs along with the *tert*-butyl-containing compounds were studied using a glassy carbon electrode as a support while for the acetaminophen-based Pcs, nitrite was selected as the analyte of choice.

1.4.1 Hydrazine

Hydrazines are a class of inorganic compounds characterized by two nitrogens joined by a single bond [**117**]. Common examples of these compounds include diamine, 1,1-dimethylhydrazine and 1,2-dimethylhydrazine [**117**]. Of interest in this thesis is diamine, which will be referred to as hydrazine from this point forward.

Hydrazine has significant uses in several industries including the polymer industry, pharmaceuticals, in the production of agrochemicals as well as a propellant of sorts for spacecrafts [**117**,**118**]. The highly industrialized use of the compound makes it a potential environmental risk as it is a flammable liquid with the potential to ignite at low temperatures [**118**]. In terms of exposure to humans, the most common sources may arise from working in environments that produce hydrazine or through the consumption of contaminated water with reports suggesting that overexposure may compromise the central nervous system, the kidneys and lungs [**117**]. Other studies involving animals have shown the adverse effects induced by exposure to hydrazine at concentrations as low as 0.5 ppm [**117**]. And while the concentration required to observe a response in humans may be higher, it is still important that there are analytical devices that can detect the compound at trace levels which has informed a substantial amount of the work in this thesis.

Phthalocyanine-based electrode systems for the detection of hydrazine have been studied extensively over the years, with the Pcs being applied as single entities or complemented with other nano or biomaterials [98,119-124]. Through a significant number of reports, the bulk of the work has been centred on both symmetric substituted and unsubstituted Pcs leaving asymmetric Pcs an understudied area [119,120,122], and more than that, the actual design of the probes in terms of pairing/coupling of substituents, and determining which combination may be considered ideal, and which may not. It is for these reasons that the work described in the later chapters was pursued.

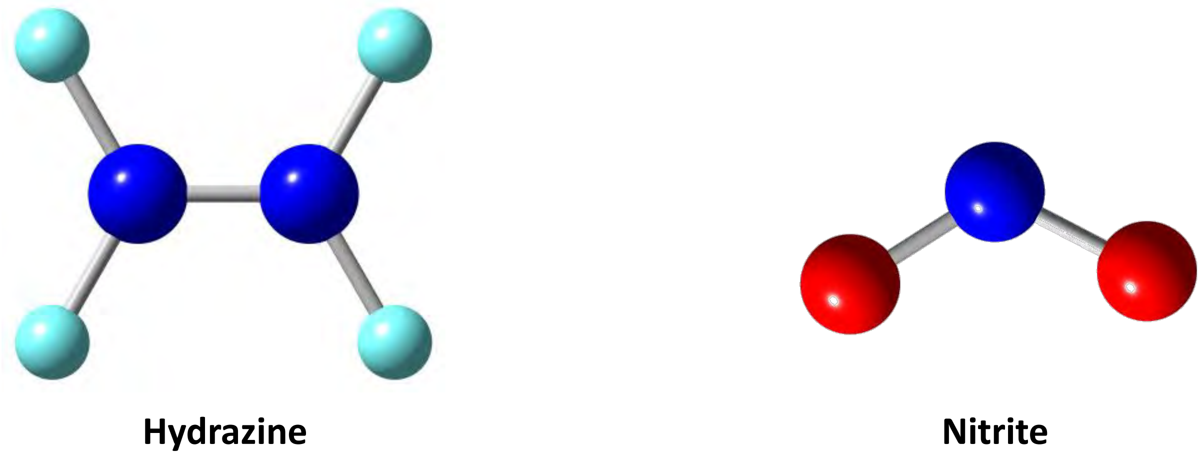

Hydrazine **Nitrite**

Fig. 1.8: Molecular structures for the analytes studied, hydrazine (N_2H_4) and nitrite (NO_2^-).

1.4.2 Nitrite

Nitrite, much like hydrazine, is an inorganic compound formed through the oxidation of ammonia by ammonia-oxidizing bacteria [125]. Although it is a naturally occurring compound, it can be created synthetically [126]. Nitrite and hydrazine are different in that there are no variations of the former, but they are alike in that they serve many purposes hence their use in various industries [117,118,127,128].

Despite its use in the curing of meat products and being an intermediate of natural processes, nitrite is toxic in that it affects blood transportation. Nitrite has the ability to bind with haemoglobin to form methemoglobin which prevents the cellular uptake of oxygen [125]. In addition to that, nitrite's ability to interact with other entities to form N-nitrosamines renders it a harmful substance that can be fatal past a certain limit as these nitrosamines are carcinogenic [129]. According to the World Health Organization (WHO), the maximum amount of nitrite allowed in drinking water is 3 mg/L which is considerably high in comparison to the maximum set by the European Community which is 0.1 mg/L [129]. The value set by the European Community coupled with what is known regarding the toxicity of nitrite is a clear indication that much like hydrazine, the need for accurate and rapid sensors remains principal.

The design of the electrocatalysts for nitrite was performed with a similar thought in mind as of those for hydrazine, establishing the most suitable combination of substituents for asymmetric Pcs as much has been done in terms of the symmetric Pcs for nitrite [129-132]. In terms of the electrocatalytic studies pertaining to nitrite, asymmetry was not the sole focus, other factors such as the central metal, the method of electrode modification as well as the inclusion of a type of nanomaterial were also considered. Ultimately, the Pcs reported in this work were selected for electrocatalysis as electrochemistry is a more viable option in terms of analytical devices as it is environmentally friendly and makes use of simple tools. Spectrophotometric methods have been reported to suffer from interferants as well as the harmful nature of reagents while chromatographic methods require specialized training [129].

1.5 Aims and objectives

1.5.1 Aims

The aim of the work presented in this thesis was to establish ideal combinations regarding the substituents in the syntheses of asymmetric Pcs and to assess whether all asymmetric Pcs may be considered better than their symmetric counterparts or not. This pursuit in establishing the "best" coupling of substituents was undertaken with the intention of improving the electrocatalytic response of Pcs to hydrazine and nitrite.

1.5.2 Objectives

In fulfilling these aims, the subsequent steps were followed:

- Syntheses of symmetric and asymmetric phthalocyanine complexes.
    - Characterization with spectroscopic and non-spectroscopic methods.
- Formation of nanocomposites where applicable/intended.
    - Characterization of composites.
- Electrochemical application of complexes.
    - Electrode modification and characterization of modified electrode surfaces.
    - Electrochemical sensing of hydrazine and nitrite, pH studies, determination of limits of detection, analyses of kinetic data and an assessment on the selectivity through the addition of potential interfering species or ions.
- Analyses of possible trends and the formulation of theories, conclusions and propositions for future work of a similar nature.

CHAPTER 2

EXPERIMENTAL

Details on the materials, synthetic procedures as well as electrode modification are provided in this chapter.

2. Experimental

2.1 Materials

2.1.1 Solvents

N,N-dimethylformamide (DMF), dimethyl sulfoxide (DMSO), tetrahydrofuran (THF), chloroform, dichloromethane (DCM), acetonitrile (ACN), ammonia, acetic acid, ethanol, methanol, 1-hexanol and cyclohexane were of analytical grade, sourced from either Merck or Sigma-Aldrich and used without further purification. The DMF was dried using activated molecular sieves for the studies involving the determination of extinction coefficients. Type I water from ELGA LabWater was used to prepare the aqueous solutions.

2.1.2 General materials

Hydrazine monohydrate, cobalt(II) chloride anhydrous, manganese(II) chloride anhydrous, 4-azidoaniline hydrochloride, triethylamine (TEA), tetrabutylammonium tetraborofluorate ($TBABF_4$), bromotris(triphenylphosphine)copper(I) ($Cu(PPh_3)_3Br$), 4-*tert*-butylphthalonitrile (**VII**), 1-ethyl-3-(3-dimethylaminopropyl)-carbodiimide (EDC), N-hydroxysuccinimide (NHS), α-cyano-4-hydroxycinnamic acid, Triton X-100 (TX), thionyl chloride, disodium hydrogen phosphate and monosodium phosphate were obtained from Sigma-Aldrich. Sodium hydroxide pellets were purchased from Minema while the sodium nitrite salt was purchased from Analar. The catalyst, 1,8-diazabicyclo[5.4.0]undec-7-ene (DBU) and phthalonitrile precursor, phthalimide, were procured from Merck.

2.1.3 Previously reported materials

The nitrogen-doped GQDs (NGQDs) (scheme shown in **Scheme A1**, **appendix**) [133], 4-(cinnamic acid) phthalonitrile (**I**) [134], 4-(3-pentadecylphenoxy) phthalonitrile (**II**) [135], 4-(4-

phenoxy)acetic acid phthalonitrile (**III**) [136], 4-(4-phenoxy)propanoic acid phthalonitrile (**IV**) [137], caffeic acid phthalonitrile (**V**) [138], 4-(4-phenoxy)benzoic acid phthalonitrile (**VI**) [139], 4-(hex-5-yn-oxy)phthalonitrile (**VIII**) [140], 4-(4-acetamidophenoxy)phthalonitrile (**IX**) [141], 4-(4-aminophenoxy)phthalonitrile (**X**) [142] and the 2,9,16,23-tetrakis-*tert*-butylphthalocyanine cobalt(II) (complex **7**) [116] were synthesised as reported in literature.

2.2 Equipment

2.2.1 Structural characterisation

- Absorption spectra were recorded using a Shimadzu UV–Vis 2550 spectrophotometer.
- Infra-red spectra were collected using a Bruker Alpha model FT-IR Spectrometer with a platinum universal attenuated total reflectance (ATR) sampling accessory.
- Raman spectra were obtained from a Bruker Vertex 70-Ram II Raman spectrometer fitted with a 1064 nm Nd:YAG laser and a liquid nitrogen cooled germanium detector.
- The mass spectral data was acquired from a Bruker AutoFLEXIII smart-beam TOF/TOF mass spectrometer using α-cyano-4-hydrocinnamic acid as the matrix.
- The elemental analysis was conducted using a Vario-Elementar Microcube ELIII.
- X-ray photoelectron spectroscopy (XPS) spectral analyses were conducted using an AXIS Ultra DLD (supplied by Kratos Analytical) using Al (monochromatic) anode equipped with a charge neutralizer.
- Size determination using dynamic light scattering (DLS) was performed using a Malvern Zetasizer nanoseries, Nano-ZS90.
- Transmission electron microscopy (TEM) images were obtained using a Zeiss Libra 120 TEM operating at 120 kV with a Megaview Olympus camera.

2.2.2 Electrochemical characterisation and application

- The electrochemical characterization (excluding electrochemical impedance spectroscopy) of the modified electrodes as well as electrochemical sensing of hydrazine and nitrite was facilitated by a Bioanalytical Systems 100W Electrochemical Analyzer using a three-electrode setup, where the glassy carbon electrode (GCE, 3 mm diameter) served as the working electrode, a platinum wire as the counter electrode and a silver/silver chloride (in 3.0 M KCl) wire as the reference electrode.
- Scanning electrochemical microscopy (SECM) experiments were conducted using a Uniscan Model 370 and a 25 mm Pt microelectrode (Uniscan) as the tip, a Pt counter electrode and Ag|AgCl wire as the pseudo-reference electrode.
    - Glassy carbon plates (GCP, Goodfellow, UK) of 1×1 cm and 2 mm thick were used as substrates for SECM.
- Electrochemical impedance spectroscopy (EIS) experiments were performed through the use of an Autolab potentiostat/galvanostat (PGSTAT302N model) operating using the NOVA 2.1 software.
    - The applied potential was set at 0.24 V, at an amplitude of 1.0×10^{-5} A_{RMS} with the frequency ranging from 0.1 to 105 Hz.
- All solutions were deaerated by bubbling argon gas prior to the experiments with the electrochemical cell being retained under an argon atmosphere throughout the duration of the experiments. All experiments were carried out at room temperature.

2.2.3 Theoretical procedure (DFT calculations)

All theoretical calculations were performed with the Gaussian09 program [143] running on an Intel/Linux cluster. The calculations were carried out at the B3LYP/6-31G(d) level for the geometry optimization through the inclusion of an SCF=QC protocol. Visualization of all the theoretical calculations was performed by the Chemcraft 1.8 software.

2.3 Syntheses

2.3.1 Synthesis of tri-(3-pentadecylphenoxy)-mono-cinnamic acid cobalt(II) phthalocyanine (complex 1), *Scheme 3.1*

Complex **1** was obtained through mixing phthalonitrile **II** (0.30 g, 0.70 mmol), phthalonitrile **I** (0.067 g, 0.23 mmol), and $CoCl_2$ (0.15 g, 1.2 mmol) of in the presence of dry *N,N*-dimethylformamide (DMF, 8 mL). To this mixture, DBU (0.5 mL) was added and the mixture was allowed to reflux for 24 h in an argon atmosphere. Upon completion, the reaction mixture was allowed to cool to room temperature and precipitated from the DMF using ethanol and water at a volumetric ratio of 1:1. The solid was dried in an oven at 60 °C and purified through column chromatography. The desired product, complex **1**, which happened to be the fourth fraction, was extracted using tetrahydrofuran, dried under vacuum and recrystallized further in ethanol. Yield: 52.1 mg, 13.0 % (w/w); UV/vis (tetrahydrofuran, THF): λ_{max}/nm (log Ɛ): 664 (3.90), 604 (3.35), 327 (3.41). IR [(KBr), ν_{max}/cm^{-1}]: 740 (aromatic $C\text{-}H_{str}$), 1090 (C-O-C) 1240 (C-N), 1466 (C=C-H), 1596 (C=C), 2851, 2918 (aliphatic $C\text{-}H_{str}$). Anal. calc. for $C_{104}H_{124}CoN_8O_6{\bullet}3H_2O$: C, 74.5; H, 7.69; N, 6.83. Found: C, 73.6; H, 8.96; N, 6.60. MS (MALDI-TOF) (m/z): calc.: 1640.90 amu; found: 1641.35 amu $[M+H]^+$.

2.3.2 Synthesis of tri-(3-pentadecylphenoxy)-mono-phenoxy acetic acid cobalt(II) phthalocyanine (complex 2), *Scheme 3.1*

The synthesis of complex **2** was achieved through refluxing a mixture composed of phthalonitriles **II** (0.30 g, 0.70 mmol) and **III** (0.070 g, 0.24 mmol), $CoCl_2$ (0.15 g, 1.2 mmol), DBU (5 mL) and DMF (8 mL) for a period of 24 h. The crude sample was precipitated using water and ethanol (v/v 1:1) after cooling and then dried in an oven at 60 °C. The desired product was separated from the crude mixture using column chromatography in which the third fraction was eluted using chloroform to produce complex **2** which was further recrystallized using ethanol. Yield: 18.9 mg, 7.06 % (w/w); UV/vis (THF): λ_{max}/nm (log Ɛ): 664 (5.02), 602 (4.41), 329 (4.72). IR [(KBr), ν_{max}/cm^{-1}]: 744, 807 (aromatic C-H_{str}), 1091 (C-O-C) 1250 (C-N), 1460 (C=C-H), 1598 (C=C), 2849, 2918 (aliphatic C-H_{str}). Anal. calc. for $C_{103}H_{124}CoN_8O_7$: C, 75.2; H, 7.60; N, 6.81. Found: C, 74.3; H, 7.69; N, 6.11. MS (MALDI-TOF) (m/z): calc.: 1644.90 amu; found: 1644.54 amu $[M]^+$.

2.3.3 Syntheses of tri-(3-pentadecylphenoxy)-mono-phenoxy propanoic acid cobalt(II) phthalocyanine and 2,9,16,23-tetrakis-(3-pentadecylphenoxy) cobalt(II) phthalocyanine (complexes 3 and 5), *Scheme 3.1*

Into a 25 mL round bottom flask, phthalonitrile **II** (0.30 g, 0.70 mmol), phthalonitrile **IV** (0.112 g, 0.38 mmol), $CoCl_2$ (0.15 g, 1.2 mmol), DBU (0.5 mL) and 1-hexanol (8 mL) were added. The reaction mixture was refluxed under an inert atmosphere for 18 h and upon cooling to room temperature, precipitated using water and ethanol (v/v 1:1). The crude solid was dried in an oven at 60 °C and purified through extensive column chromatography. The first green fraction (following elution with chloroform and methanol (v/v 9:1) was found out to be the symmetrical complex **5** (2,9,16,23-tetrakis(3-pentadecylphenoxy) cobalt (II) phthalocyanine). The intended product (complex **3**), fraction two, was extracted from the mixture using THF. Further purification was carried out in which complex **3** was extracted using cyclohexane whilst silica gel (SiO_{60}) served as the stationary phase.

Complex **3**: Yield: 21.1 mg, 3.33 % (w/w); UV/vis (THF): λ_{max}/nm (log Ɛ): 664 (4.75), 603 (4.17), 330 (4.58). IR [(KBr), ν_{max}/cm^{-1}]: 742, 799 (aromatic C-H_{str}), 1093 (C-O-C) 1252 (C-N), 1460

(C=C-H), 1598 (C=C), 2851, 2920 (aliphatic C-H$_{str}$). Anal. calc. for $C_{104}H_{126}CoN_8O_6$: C, 76.0; H, 7.73; N, 6.82. Found: C, 75.4; H, 6.73; N, 6.10. MS (MALDI-TOF) (*m/z*): calc.: 1642.92 amu; found: 1644.84 amu $[M+2H]^+$.

Complex **5**: Yield: 70.4 mg, 5.56 % (w/w); λ_{max}/nm (log Ɛ): 665 (4.33), 605 (3.92), 320 (4.59). IR [(KBr), ν_{max}/cm^{-1}]: 744, 793 (aromatic C-H$_{str}$), 1091 (C-O-C), 1240 (C-N), 1468 (C=C-H), 1588 (C=C), 1721 (C=O), 2851, 2918 (aliphatic C-H$_{str}$). Anal. calc. for $C_{116}H_{152}CoN_8O_4 \bullet 3H_2O$: C, 75.94; H, 8.62; N, 6.11. Found: C, 75.5; H, 8.50; N, 6.11. MS (MALDI-TOF) (*m/z*): calc.: 1781.13 amu; found: 1781.13 amu $[M]^+$.

2.3.4 Synthesis of tri-(3-pentadecylphenoxy)-mono-caffeic acid cobalt(II) phthalocyanine (complex 4), *Scheme 3.1*

Through refluxing phthalonitriles **II** (0.30 g, 0.70 mmol) and **V** (0.11 g, 0.33 mmol) in the presence of $CoCl_2$ (0.15 g, 1.2 mmol), DBU (0.5 mL) and dry DMF (8 mL) in an argon-based atmosphere for a period of 18 h, complex **4** was synthesized. Prior to eluting the desired compound from gel chromatography with cyclohexane as the mobile phase, the crude product was precipitated using water and ethanol (v/v 1:1) and then dried in an oven at 60 °C. Following purification through column chromatography, the newly formed complex was recrystallized in ethanol and dried further under vacuum. Yield: 21.1 mg, 3.51 % (w/w); UV/vis (THF): λ_{max}/nm (log Ɛ): 664 (4.81), 604 (4.42), 327 (4.71). IR [(KBr), ν_{max}/cm^{-1}]: 740, 801 (aromatic C-H$_{str}$), 1091 (C-O-C), 1250 (C-N), 1458 (C=C-H), 1584 (C=C), 1702 (C=O), 2847, 2916 (aliphatic C-H$_{str}$). Anal. calc. for $C_{104}H_{122}CoN_8O_7$: C, 75.5; H, 7.43; N, 6.77. Found: C, 75.1; H, 7.69; N, 6.01. MS (MALDI-TOF) (m/z): calc.: 1654.88 amu; found: 1655.87 amu $[M+H]^+$.

2.3.5 Synthesis of 4-(tri-*tert*-butyl)-mono phenoxy benzoic acid cobalt(II) phthalocyanine (complex 6), *Scheme 3.2*

Phthalonitriles **VII** (0.40 g, 2.2 mmol) and **VI** (0.12 g, 0.44 mmol) along with $CoCl_2$ (0.14 g, 1.1 mmol) were added to dry DMF (8.0 mL) in the presence of DBU (0.5 mL). The mixture was refluxed for 18 h in an argon atmosphere. Following the end of the 18 h period, the product was left to cool to room temperature after which the crude sample was precipitated using methanol and then dried in an oven at 60 °C. The crude product was washed several times with THF and purified further through column chromatography where the desired compound was eluted as the first fraction with THF (in which SiO_{60} served as the stationary phase). Yield: 30.0 mg, 7.92 % (w/w); UV/vis (DMF): λ_{max}/nm (log Ɛ): 664 (4.65), 604 (4.14), 328 (4.48). IR [(KBr), ν_{max}/cm^{-1}]: 687 (aromatic C-H_{str}), 1091 (C-O-C), 1231 (C-N), 1366 (C-H_{bend}), 1594 (C=C), 1643 (C=O), 2926 (aliphatic C-H_{str}), 3236, 3361 (-OH_{COOH}). Anal. calc. for $C_{51}H_{44}CoN_8O_3$•$2H_2O$: C, 67.2; N, 12.3. Found: C, 67.2; N, 11.6. MS (MALDI-TOF) (m/z): calc.: 875.29 amu; found: 876.98 amu $[M+H]^+$.

2.3.6 Syntheses of *tris*-(4-acetamidophenoxy)-mono-(hex-5-yn-1-yloxy) cobalt(II) phthalocyanine and 2,9,16,23-tetrakis-acetamidophenoxy cobalt(II) phthalocyanine (complexes 8 and 9), *Scheme 3.3*

Phthalonitriles **IX** (0.40 g, 1.4 mmol) and **VIII** (0.065 g, 0.29 mmol) along with the metal salt, $CoCl_2$ (0.094 g, 0.72 mmol), were added to dry DMF (15 mL) in the presence of DBU (0.5 mL). The mixture was refluxed over a period of 18 h in an argon atmosphere. Following the completion of the reaction, the product was left to cool to room temperature after which the crude sample was precipitated using methanol and water and then dried in an oven at 120 °C. The asymmetric compound (**8**, obtained as the second fraction) was separated from its symmetric counterpart (**9**) and other impurities using column chromatography using THF and methanol as the mobile phase (v/v 9:1) and SiO_{60} as the stationary phase. Yield: 39.4 mg, 12.3 % (w/w); UV/vis (DMF): λ_{max}/nm (log Ɛ): 667 (4.86), 608 (4.31), 327 (4.71). IR [(KBr), ν_{max}/cm^{-1}]: 746, 795 (aromatic C-H$_{str}$), 1087 (C-O-C), 1258 (C-N), 1464 (C=C), 1501 (C-H), 1537 (N-H), 1662 (C=O), 2849, 2916 (aliphatic C-H$_{str}$), 3273 (C≡C-H). Anal. calc. for $C_{62}H_{45}CoN_{11}O_7 \bullet 5H_2O$: C, 61.8; H, 4.80; N, 12.8. Found: C, 61.6; H, 3.60; N, 12.4. MS (MALDI-TOF) (m/z): calc.: 1114.28 amu; found: 1114.34 amu $[M]^+$.

Complex **9** was obtained as a one of the side-products from the synthesis of complex **8**. It was eluted as the first fraction using THF as the mobile phase and SiO_{60} as the stationary phase. Yield: 138 mg, 41.0 % (w/w); UV/vis (DMF): λ_{max}/nm (log Ɛ): 672 (4.66), 611 (4.16), 328 (4.52). IR [(KBr), ν_{max}/cm^{-1}]: 746 (aromatic C-H$_{str}$), 1089 (C-O-C), 1223 (C-N), 1465 (C=C), 1501 (C-H), 1525 (N-H), 1655 (C=O), 2924 (aliphatic C-H$_{str}$). Anal. calc. for $C_{64}H_{44}CoN_{12}O_8 \bullet 2H_2O$: C, 63.8; H, 4.02; N, 14.0. Found: C, 63.4; H, 3.78; N, 14.0. MS (MALDI-TOF) (m/z): calc.: 1167.27 amu; found: 1169.03 amu $[M+2H]^+$.

2.3.7 Syntheses of *tris*-(4-acetamidophenoxy)-mono-(hex-5-yn-1-yloxy) manganese(III) chloride phthalocyanine and 2,9,16,23-tetrakis-acetamidophenoxy manganese(III) chloride phthalocyanine (complexes 10 and 11), *Scheme 3.3*

The synthesis of complex **10** was achieved in the same way as that of complex **8** where the stoichiometric ratios between the phthalonitriles were retained as 1:5 between phthalonitriles **IX** and **VIII**. The only changes made were that of the metal salt where $MnCl_2$ (0.11 g, 0.89 mmol) was used and that for the precipitation process of the crude product only water was used. The dried compound was purified using column chromatography where SiO_{60} served as the stationary phase while tetrahydrofuran and methanol (v/v 9:1) was used as the eluent. Yield: 12.6 mg, 3.81 % (w/w); UV/vis (DMF): λ_{max}/nm (log Ɛ): 723 (4.67), 651 (3.96), 362 (4.34). IR [(KBr), ν_{max}/cm^{-1}]: 744, 801 (aromatic C-H$_{str}$), 1072 (C-O-C), 1225 (C-N), 1472 (C=C), 1501 (C-H), 1541 (N-H), 1660 (C=O), 2853, 2918 (aliphatic C-H$_{str}$), 3255 (C≡C-H). Anal. calc. for $C_{62}H_{45}ClMnN_{11}O_7 \bullet 4H_2O$: C, 61.1; H, 4.38; N, 12.6. Found: C, 61.1; H, 3.49; N, 11.9. MS (MALDI-TOF) (m/z): calc.: 1145.26 amu; found: 1110.41 amu [M-Cl]$^+$.

Similar to complex **9**, complex **11** was one of the side-products in the synthesis of complex **10**. The compound was also eluted as the first fraction using THF as the mobile phase and SiO_{60} as the stationary phase. Yield: 27.0 mg, 7.81 % (w/w); UV/vis (DMF): λ_{max}/nm (log Ɛ): 721 (3.96), 640 (3.50), 380 (3.96). IR [(KBr), ν_{max}/cm^{-1}]: 740 (aromatic C-H$_{str}$), 1079 (C-O-C), 1231 (C-N), 1459 (C=C), 1501 (C-H), 1543 (N-H), 1658 (C=O), 2851, 2919 (aliphatic C-H$_{str}$). Anal. calc. for $C_{64}H_{44}ClMnN_{12}O_8$: C, 64.1; H, 3.70; N, 14.0. Found: C, 64.1; H, 3.66; N, 12.1. MS (MALDI-TOF) (m/z): calc.: 1198.25 amu; found: 1163.70 amu [M-Cl]$^+$.

2.3.8 Synthesis of *tris*-(4-acetamidophenoxy)-mono-aminophenoxy cobalt(II) phthalocyanine (complex 12), *Scheme 3.3*

Phthalonitriles **X** (0.14 g, 0.58 mmol) and **IX** (0.40 g, 1.44 mmol), along with $CoCl_2$ (0.094 g, 0.72 mmol), were added to dry DMF (15 mL) containing DBU (0.5 mL). The mixture was refluxed over a period of 24 h in an argon atmosphere. Upon completion, the product was cooled to room temperature after which the crude sample was precipitated using methanol and water (v/v 1:1) and then dried in an oven at 60 °C. The desired compound was obtained as the first fraction using THF as the mobile phase and SiO_{60} as the stationary phase. Yield: 58.0 mg, 8.66 % (w/w); UV/vis (DMF): λ_{max}/nm (log Ɛ): 665 (4.86), 604 (4.37), 326(4.80). IR [(KBr), vmax/cm^{-1}]: 740 (aromatic C-H$_{str}$), 1089 (C-O-C), 1225 (C-N), 1462 (C=C), 1501 (C-H), 1662 (C=O), 2865, 2922 (aliphatic C-H$_{str}$), 3257 (N-H). Anal. calc. for $C_{62}H_{42}CoN_{12}O_7 \bullet 2H_2O$: C, 64.1; H, 3.99; N, 14.5. Found: C, 64.0; H, 3.56; N, 13.3. MS (MALDI-TOF) (m/z): calc.: 1126.27 amu; found: 1126.14 amu $[M]^+$.

2.3.9 Synthesis of *tris*-(4-acetamidophenoxy)-mono-phenoxy benzoic acid cobalt(II) phthalocyanine (complex 13), *Scheme 3.3*

Phthalonitriles **IX** (0.40 g, 1.5 mmol) and **VI** (0.076 g, 0.29 mmol), and $CoCl_2$ (0.094 g, 0.72 mmol) were added to dry DMF (10 mL) and DBU (0.5 mL). The mixture was refluxed over a period of 24 h in an argon atmosphere. Following the completion of the reaction, the product was allowed to cool to room temperature after which the crude sample was precipitated using methanol and water and then dried in an oven at 60 °C. The desired compound was obtained as the fourth fraction where silica gel (SiO_{60}) served as the stationary phase and a solvent mixture of DMF and acetic acid served as the mobile phase (v/v 9:1). Yield: 60.4 mg, 15.9 % (w/w); UV/vis (DMF): λ_{max}/nm (log Ɛ): 668 (4.14), 609 (3.72), 325 (4.04). IR [(KBr), ν_{max}/cm^{-1}]: 746 (aromatic C-H_{str}), 1089 (C-O-C), 1225 (O-C_{str}), 1401 (-OH_{bend}), 1503 (C-H), 1660 (C=O), 3053 (C=H). Anal. calc. for $C_{63}H_{49}CoN_{11}O_9 \bullet 4H_2O$: C, 61.7; N, 12.6. Found: C, 61.6; N, 11.7. MS (MALDI-TOF) (m/z): calc.: 1154.24 amu; found: 1155.82 amu $[M+H]^+$.

2.3.10 Synthesis of *tris*-(4-acetamidophenoxy)-mono-phenoxy propanoic acid cobalt(II) phthalocyanine (complex 14), *Scheme 3.3*

The synthesis of complex **14** was the same as for complex **13** except phthalonitrile **IV** (0.10 g, 0.36 mmol) was used instead of phthalonitrile **VI**. The amounts of all the other reagents were the same as well as reaction conditions and purification methods, except for complex **14** hot methanol was used for the final purification Yield: 49.7 mg, 13.0 % (w/w); UV/vis (DMF): λ_{max}/nm (log Ɛ): 667 (4.42), 610 (4.08), 324 (4.41). IR [(KBr), ν_{max}/cm^{-1}]: 746 (aromatic C-H_{str}), 1091 (C-O-C), 1229 (O-C_{str}), 1403 (-OH_{bend}), 1503 (C-H), 1656 (C=O),2936 (aliphatic C-H_{str}), 3051 (C=H). Anal. calc. for $C_{65}H_{45}CoN_{11}O_9$•$3H_2O$: C, 63.1; N, 12.5. Found: C, 62.2; N, 12.4. MS (MALDI-TOF) (m/z): calc.: 1182.27 amu; found: 1182.76 amu $[M]^+$.

2.3.11 Synthesis of *tris*-(4-acetamidophenoxy)-mono-caffeic acid cobalt(II) phthalocyanine (complex 15), *Scheme 3.3*

The synthesis of complex **15** was slightly different to that of **13** and **14** as follows: to a 25 mL round bottom flask, phthalonitriles **IX** (0.42 g, 1.5 mmol) and **V** (0.14 g, 0.46 mmol), $CoCl_2$ (0.094 g, 0.72 mmol) and 10 mL DMF were added. The mixture was allowed to stir at 150 °C for a period of 2 h after which 0.5 mL of DBU was added. The mixture was further refluxed over a period of 18 h in an argon atmosphere. The rest of the purification is as explained above for **13** and **14**, except **15** was collected as the fourth fraction on the silica column and hot methanol was used for final purification. Yield: 86.5 mg, 22.7 % (w/w); UV/vis (DMF + 5 % TX): λ_{max}/nm (log Ɛ): 674 (4.59), 606 (4.04), 342 (4.37). IR [(KBr), ν_{max}/cm^{-1}]: 742 (aromatic C-H_{str}), 1091 (C-O-C), 1225 (O-C_{str}), 1401 (-OH_{bend}), 1501 (C-H), 1541 (N-H), 1660 (C=O), 2855, 2916 (aliphatic C-H_{str}). (MALDI-TOF) (m/z): calc.: 1194.24 amu; found: 1196.44 amu $[M+2H]^+$.

2.4 Formation of conjugates

The influence of combining NGQDs with the cobalt(II) Pcs (CoPc/s) was studied using two of the complexes synthesized, complexes **9** (symmetric) and **12** (asymmetric). In addition to assessing the significance of symmetry/asymmetry, an analysis on how the composite is formed was also performed. This was done through forming the composites in two ways, through covalent interactions and non-covalent means (π-π stacking). π-π stacking was performed on both complexes, **9** and **12** whilst covalent linkage was reserved for complex **12** as it possesses the primary amine which enables amide bond formation with the carboxylic acid groups from the NGQDs.

2.4.1 Conjugation through π-π stacking, *Scheme 3.4*

The approach undertaken in creating the CoPc-NGQDs composites through π-π stacking was adopted from a previous study involving similar CoPcs [96]. Briefly, for each CoPc derivative, 3.2 mg (2.74×10^{-6} mol for **9**, and 2.84×10^{-6} mol for **12**) was dissolved in DMF (1.0 mL), whilst separately, 3.2 mg of the NGQDs were dissolved in 1.0 mL of water. Subsequently, the two solutions were mixed together and sonicated at room temperature for a period of 4 h followed by constant stirring at room temperature for 5 days. Ethanol was used for precipitating and washing (twice) the conjugates which were then dried under vacuum. These conjugates from this point forward are referred to as **9πNGQDs** and **12πNGQDs**, where the number refers to the CoPc complex, and the "π" symbol denoting π-π stacking of the CoPc to the NGQDs.

2.4.2 Conjugation through covalent linking, *Scheme 3.5*

The method of conjugating the NGQDs to complex **12** through covalent interactions was adopted from a study by Achadu and colleagues [144]. An amide bond was formed using the primary amine (NH_2) from complex **12** and the carboxylic acid groups (COOH) from the NGQDs. Briefly, complex **12** (4.0 mg, 3.56×10^{-6} mol) was dissolved in DMF (1.0 mL), and separately, NGQDs (4.0 mg) were dissolved in water (2.0 mL). To the NGQDs solution, the coupling agents NHS (0.10 g, 8.69×10^{-4} mol) and EDC (0.10 g, 6.44×10^{-4} mol) were added and sonicated until everything was dissolved. To the NGQDs mixture, complex **12** (in DMF) was added and the resultant mixture was sonicated further for an additional 4 h after which it was left to stir at room temperature for period of 48 h. Following that, the conjugate was precipitated with ethanol, and washed twice with ethanol before drying under vacuum. The covalently linked conjugate is, from this point forward, referred to as **12@NGQDs**.

2.5 Electrode modification

The predominant method of electrode modification selected was that of drop-drying/adsorption. This was performed for all the probes investigated. An additional method for the alkyne-containing Pcs was also explored where the Pcs were anchored covalently onto the electrode surface. The Pcs for which this was performed are complexes **8** and **10** with the complete list of the modified electrode surfaces presented in **Table 4.1.**

2.5.1 Modification through adsorption (drop-drying)

Prior to surface modification of the electrode, the GCE was cleaned by polishing in a slurry of alumina nanopowder (Sigma-Aldrich) on a SiC-emery paper and rinsed with Millipore water several times. The electrode was further treated to ultra-sonication in 1.0 M of HCl and rinsed with Millipore water again. In preparing the Pcs as single entities, for complexes **1**-**5**, 1.0 mg of each was dissolved in 1.0 mL of THF whilst for complexes **6**-**15**, 1.0 mg was dissolved in 1.0 mL of DMF from which 10 µL was dropped onto the electrode surface followed by drying in an oven at 60 °C overnight. The modified electrodes are referred to as **GCE-PcA** where the GCE denotes the glassy carbon electrode, “Pc” refers to the complex and “A” symbolizes the method of modification which in this case, is adsorption.

With respect to the conjugates, 1.0 mg of the conjugate(s) (or the NGQDs alone), was dissolved in 1.0 mL of DMF (1.0 mL of water for the NGQDs). This was followed by electrode modification using the same volume and drying protocol explained for the Pc complexes. The electrodes fashioned from the nanocomposites are from hereon, referred to as and **GCE-9πNGQDs**, **GCE-12πNGQDs** and **GCE-12@NGQDs** for the corresponding π and covalently formed conjugates.

Modification of the glassy carbon plates (GCP) was achieved in the same manner with the naming convention being "**GCP**-**PcA**" where "GCP" refers to the glassy carbon plate, "Pc" the complex and "A", the method of electrode modification adopted.

2.5.2 Modification through covalent anchoring ("clicking")

The cleaning of the electrode surface was achieved in the same way described for modification through adsorption. The method undertaken for the formation of a triazole bond was as reported by Nxele and Mpeta [34,145] with a few modifications. As expressed already, only complexes **8** and **10** were involved in this kind of electrode modification as they possess the necessary functional group (an alkyne terminal). Briefly, $TBABF_4$ (0.01 M) and 4-azidoaniline hydrochloride (0.1 mM) were prepared in a mixture of acetonitrile (0.1 M) and 1.0 M HCl (96:4). In this solution, three successive cyclic voltammetric scans were performed (from −1000 mV to +200 mV) to graft the bare electrode where the surface was seemingly passivated by the introduction of azide-bearing constituents. Following the grafting, the electrodes were immersed in a solution composed of $Cu(PPh_3)_3Br$ (2.0 mM), Pc (0.14 mM) in DMF (0.5 mL) and triethylamine (0.5 mL). The electrodes were left suspended in the solution for approximately 18 h after which they were rinsed with ethanol, and Millipore water, dried in ambient conditions and applied as electrocatalysts. The electrode modified with complex **8** is denoted as **GCE-8C** while that altered with complex **10**, is referenced as **GCE-10C** (where "C" represents clicking).

In modifying the glassy carbon plates, the same protocol adopted for the modification of the GCE was applied. The modified carbon plates are referred to as **GCP**-**8C** and **GCP-10C** where the "C" following the complex number denotes the method of surface modification, clicking.

2.6 Attempted syntheses

Attempts at synthesizing binuclear CoPcs were made however, none of the attempted structures were met with success (**Schemes 2.1** and **2.2**). Complex **18** was observed in the preliminary analysis using mass spectroscopy however, the tetra-substituted Pc (complex **9**) could not be separated from the binuclear Pc using chromatographic methods.

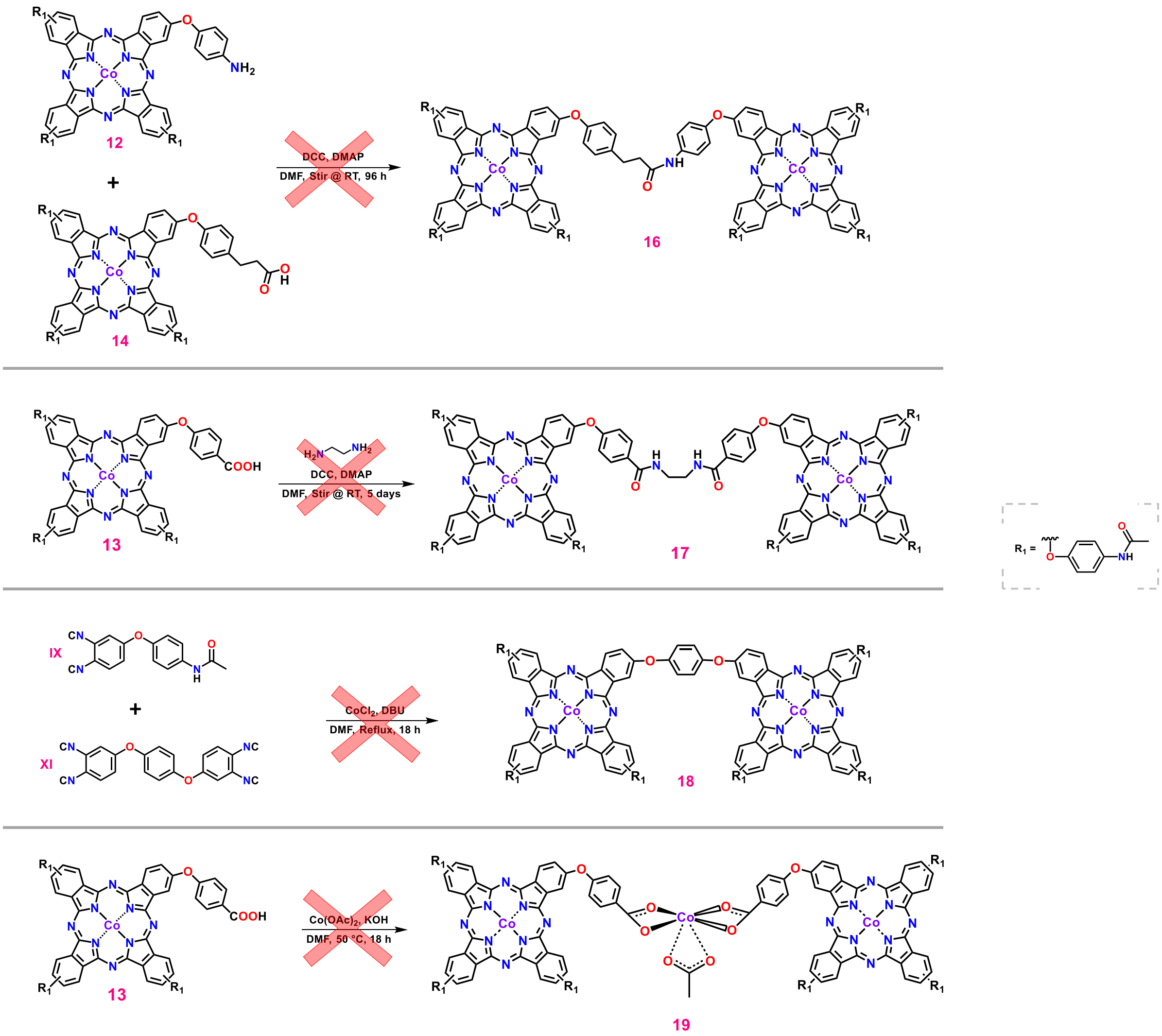

Scheme 2.1: Synthetic routes for the attempted complexes, **16**-**19**. (DCC = dicyclohexyl carbodiimide; DMAP = 4-dimethylaminopyridine; DMF = *N,N*-dimethylformamide; DBU = 1,8-diazabicyclo(5.4.0)undec-7-ene).

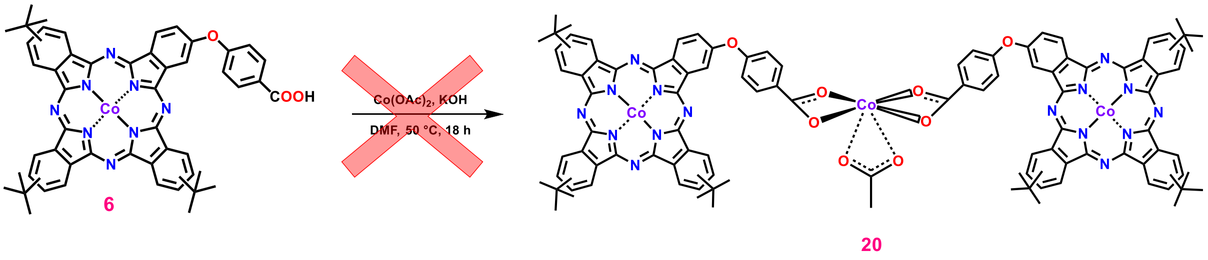

Scheme 2.2: Synthetic route for the attempted complex **20**. (DMF = *N,N*-dimethylformamide).

RESULTS AND DISCUSSION

The following chapters are based on the publications listed in the Publications' section:

- **Chapter 3** – Characterisation of the synthesized materials.
- **Chapter 4** – Characterisation of the modified electrodes.
- **Chapter 5** – Electrochemical studies on the detection of hydrazine and nitrite using the synthesized materials.

PUBLICATIONS

1. **R. Nkhahle**, T. Nyokong. Creating the ideal push-pull system for electrocatalysis: A comparative study on symmetrical and asymmetrical cardanol-based cobalt phthalocyanines, **Electroanalysis,** *33* (2021) 11.
2. **R. Nkhahle**, T. Nyokong. Electrochemical detection of nitrite on electrodes modified by click chemistry using asymmetrical Co(II) and Mn(II) phthalocyanines containing push-pull substituents, **Journal of the Electrochemical Society,** *168* (2021) 117514 (Issue on Women in Electrochemistry).
3. **R. Nkhahle**, T. Nyokong, Assessing the electrocatalytic activity of a localized push-pull system in cobalt phthalocyanine/graphene quantum dot hybrids, **Materials Chemistry and Physics,** *280* (2022) 125842.
4. **R. Nkhahle**, Nthabeleng Molupe, John Mack, T. Nyokong. Correlating theory with experimental data on the effect of symmetry on the electrocatalytic behaviour of Co phthalocyanines, **Inorganica Chimica Acta**, *554* (2023) 121548.

Other publications unrelated to the work in this thesis

1. K. E. Sekhosana, **R. Nkhahle**, T. Nyokong **A**nalytical detection and electrocatalysis of paracetamol in aqueous media using rare-earth double-decker phthalocyaninato chelates as electrochemically active materials, **Chemistry Select**, *5* (2020) 9857.
2. S. R. Nxele, **R. Nkhahle**, T. Nyokong. The composites of asymmetric Co phthalocyanines-graphitic carbon nitride quantum dots-aptamer as specific electrochemical sensors for the detection of prostate specific antigen: Effects of ring substituents, **Journal of Electroanalytical Chemistry**, *900* (2021) 115730.
3. S. Nxele, **R. Nkhahle**, T. Nyokong. The synergistic effects of coupling Au nanoparticles with an alkynyl Co(II) phthalocyanine on the detection of prostate specific antigen, **Talanta**, *237* (2021) 122948.

CHAPTER 3

CHARACTERISATION OF MATERIALS

A detailed discussion based on the characterisation of the phthalocyanine complexes and the conjugates is provided in this chapter.

3. Synthesis and characterisation

3.1 Phthalocyanine complexes

The synthetic route applied in the syntheses of the asymmetric complexes involved the use of similar methodologies previously reported [78]. Variations in the stoichiometric ratios were made in an attempt to improve the yields however, none exceeded 1:5 depite prior studies reporting the use of ratios of 1:9 or more [78]. *N,N*-dimethylformamide (DMF) was chosen as the solvent for all the reactions with the exception of complex **3** (and consequently, complex **5**). Complex **3** and **5** were obtained using 1-hexanol as the primary attempt with DMF was unsuccessful. The reaction times were set at either 18 or 24 h to ensure that sufficient time is provided for the materials to react without potentially degrading the products due to a high level of heat over a prolonged period of time. The yields obtained for the symmetric complexes were higher than those observed for the primary asymmetric compounds. Overall, however, the A_3B complexes with the acetaminophen substituent (complexes **8**, **10** and **12**-**15**), had better yields in comparison to the A_3B Pcs with alkyl-dominated substituents (complexes **1**-**4** and **6**). The synthetic routes for complexes **1**-**6** and **8**-**15** are shown in **Schemes 3.1**, **3.2** and **3.3**.

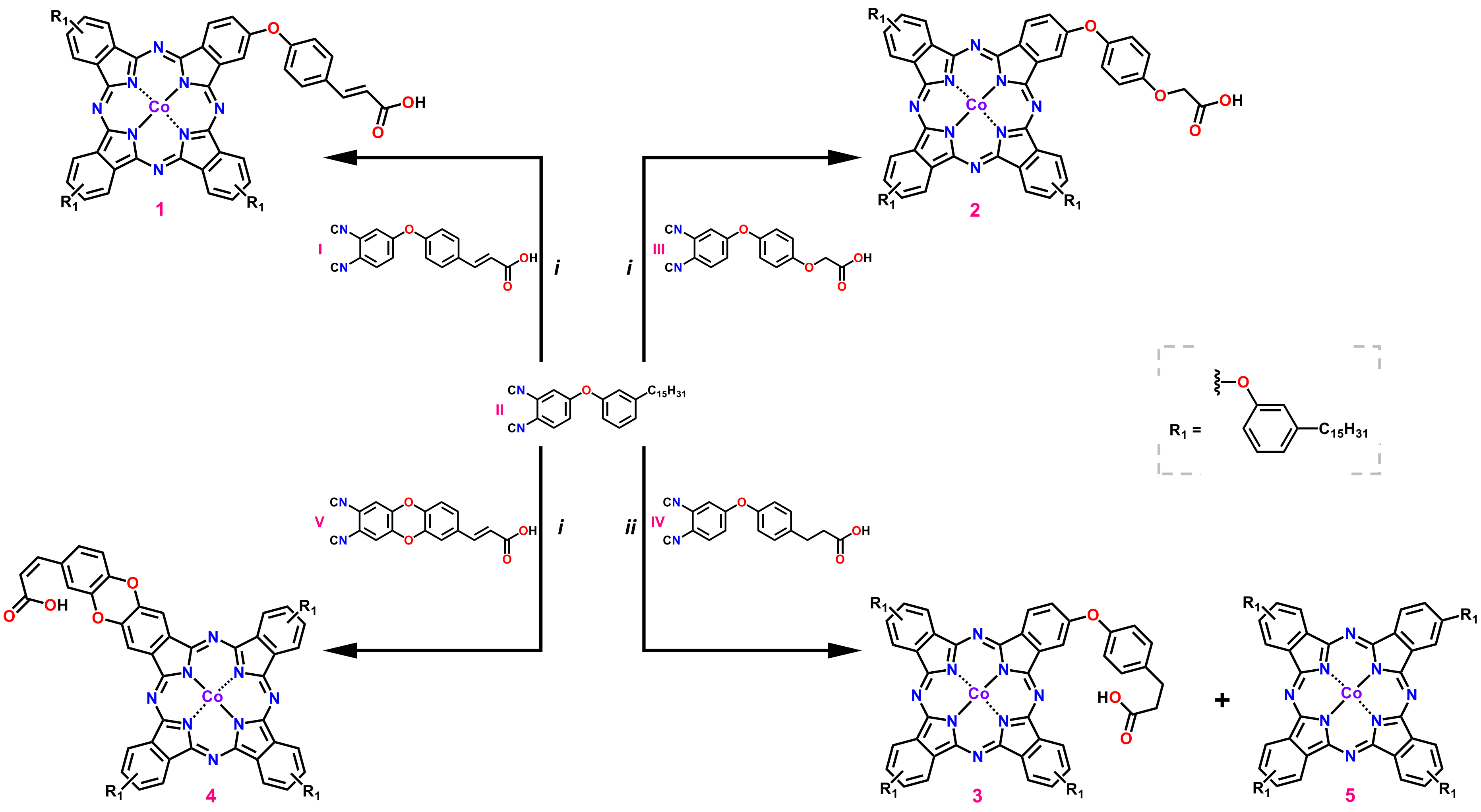

Scheme 3.1: Synthetic routes for complexes **1**-**5**. *i* – $CoCl_2$,1,8-diazabicyclo[5.4.0]undec-7-ene (DBU), *N,N*-dimethylformamide (DMF); *ii* – $CoCl_2$,DBU, 1-hexanol.

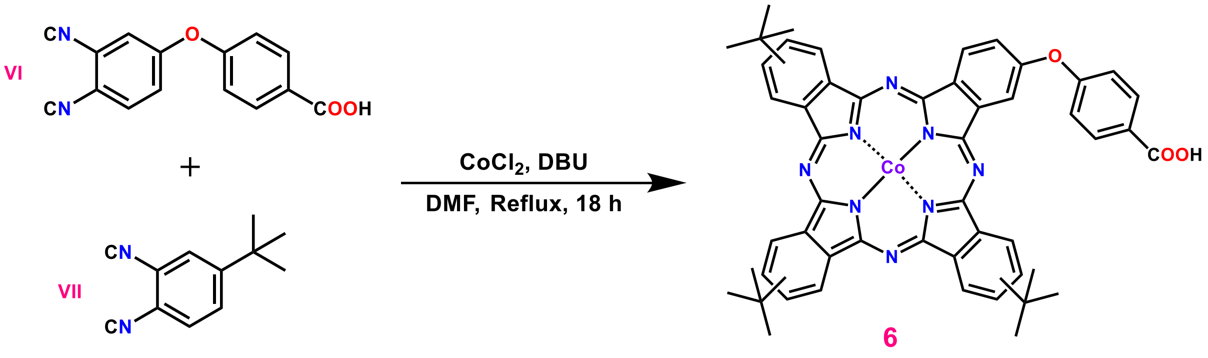

Scheme 3.2: Synthetic route for complex **6**.

Characterisation of the synthesized complexes was performed using a wide range of spectroscopic techniques such as mass spectroscopy, Fourier-transform infrared and absorption spectroscopy. Elemental analyses was the only thermogravimetric method used as it is considered significant in evaluating the purity of organic compounds.

Based on the mass spectral analyses, all the desired compounds were synthesized and purified to a satisfactory level as suggested by the ionization signals obtained. **Table 3.1** provides a summary of the atomic masses expected and the experimental results obtained (**Figs. A1-A15**). For the majority of the complexes, the mass recorded was not too different from that which was anticipated with the difference largely arising from the addition of one or two protons. The manganese complexes (complexes **10** and **11**) bore the greatest of differences as the ionization peak was that of the complexes in the absence of the axial ligand, chlorine (**Table 3.1**).

The Q-band maxima for all the complexes studied are presented in **Table 3.1** with some of the absorption spectra showcased in **Fig. 3.1**. As witnessed from the data in **Table 3.1**, the differences in the maximum Q-band absorption for the cobalt complexes is of a negligible magnitude with a few exceptions. Significant differences in the positions of the Q-band however, were found to exist between the cobalt and manganese complexes.

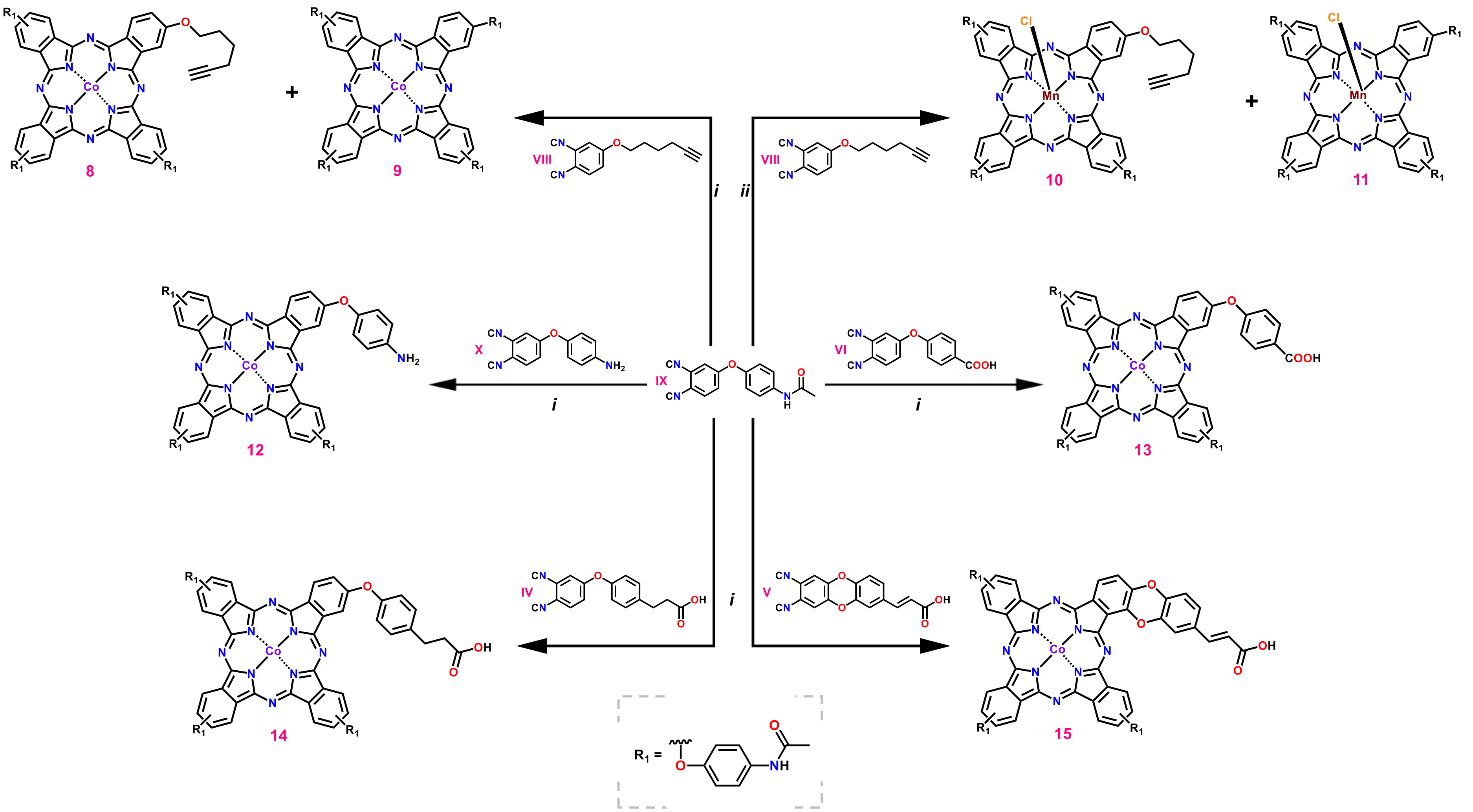

Scheme 3.3: Synthetic routes for complexes **8**-**15**. *i* – $CoCl_2$,1,8-diazabicyclo[5.4.0]undec-7-ene (DBU), *N,N*-dimethylformamide (DMF); *ii* – $MnCl_2$, DBU, DMF.

From the CoPcs alone, only complexes **9** and **15** registered a Q-band maxima that exceeds 670 nm with values of 672 nm and 674 nm respectively, being observed for the two complexes. A notable observation was made for complex **15** in that the Pc is aggregated as seen with the broad Q-band in **Fig. 3.1B**. This aggregation, however, was resolved with the addition of the surfactant Triton X-100 hence the appearance of a monomeric Q-band (**Fig. 3.1B**). Regarding the rest of the CoPcs, the differences in Q-band maxima did not exceed 5 nm (**Table 3.1**). Compared to the CoPcs, the manganese Pcs (MnPcs) exhibited a strong redshift with the maximum Q-band absorbances being recorded at wavelengths of 723 nm and 721 nm for complexes **10** and **11**, respectively (**Table 3.1**).

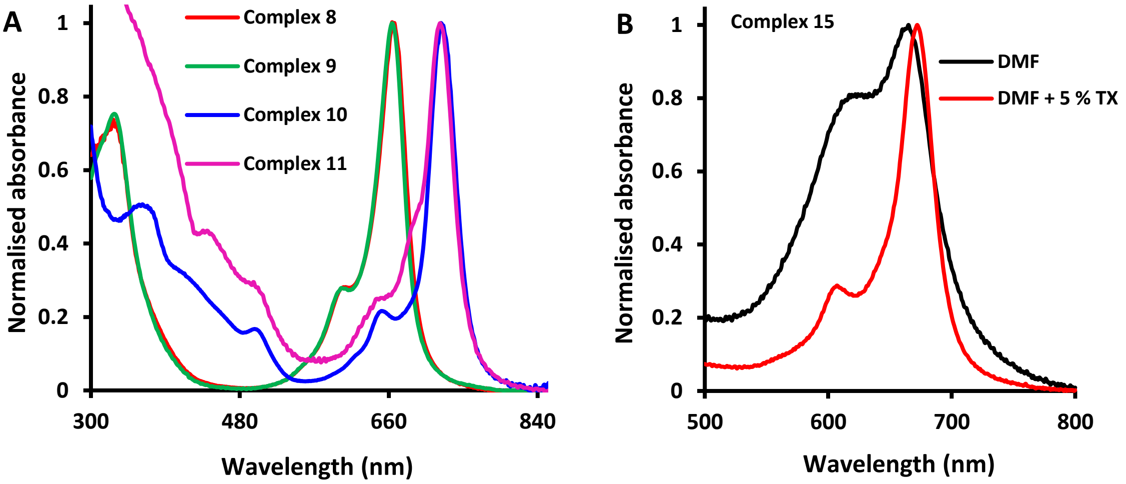

Fig. 3.1: A selection of the absorption spectra of some complexes synthesized where in (**A**), complexes **8**-**11** are in DMF and (**B**) is the absorption spectra of complex **15** in DMF, in the absence and presence of Triton X-100 (TX, ~ 10^{-5} M).

Although the MnPcs were synthesized from an Mn^{2+} salt, the products themselves, complexes **10** and **11**, did not assume this oxidation state but rather that of Mn^{3+} (as suggested by the Q-band maxima, **Table 3.1**). According to the literature, the change from Mn^{2+} to Mn^{3+} is not an anomaly but rather a common occurrence where MnPcs are purified under aerobic conditions (i.e. ambient air) [146]. Overall, there were no significant differences between the symmetric Pcs and the symmetric counterparts (**Table 3.1**).

Table 3.1: A summary of the mass spectral results as well the Q-band maxima from the absorption spectra of the complexes synthesized.

Complex	Expected mass (m/z)	Mass observed (m/z)	Q-band maxima (nm)
1	1640.90	1641.35	664 (THF)
2	1644.90	1644.54	664 (THF
3	1642.92	1644.84	664 (THF)
4	1654.88	1655.87	664 (THF
5	1781.13	1781.13	665 (THF)
6	875.29	876.98	664 (DMF)
7[a]	795.90	795.93	666 (DMF)
8	1114.28	1114.34	667 (DMF)
9	1167.27	1169.03	672 (DMF)
10	1145.26	1110.41	723 (DMF)
11	1198.25	1163.70	721 (DMF)
12	1126.27	1126.14	665 (DMF)
13	1154.24	1155.82	668 (DMF)
14	1182.27	1182.76	667 (DMF)
15[b]	1194.24	1196.44	674 (DMF)

a – Q-band maximum previously reported in THF at 661 nm [116]; b – Q-band reported in DMF and 5 % Triton X-100.

Fourier-transform infrared spectroscopy (FT-IR) was employed to assess the presence of the anticipated functional groups (and the disappearance of others where a reaction has taken place). In the synthesis of all the Pcs, the primary indication that the cyclotetramerization of the phthalonitrile had taken place was identified through the disappearance of the nitrile peak which is observed at approximately 2230 cm^{-1} (phthalonitrile **VIII** in **Fig. 3.2** as an example). In addition to the disappearance of the nitrile peak, stretching frequencies related to the phthalonitrile derivatives employed were also identified (**8** and **10** in **Fig. 3.2** as examples).

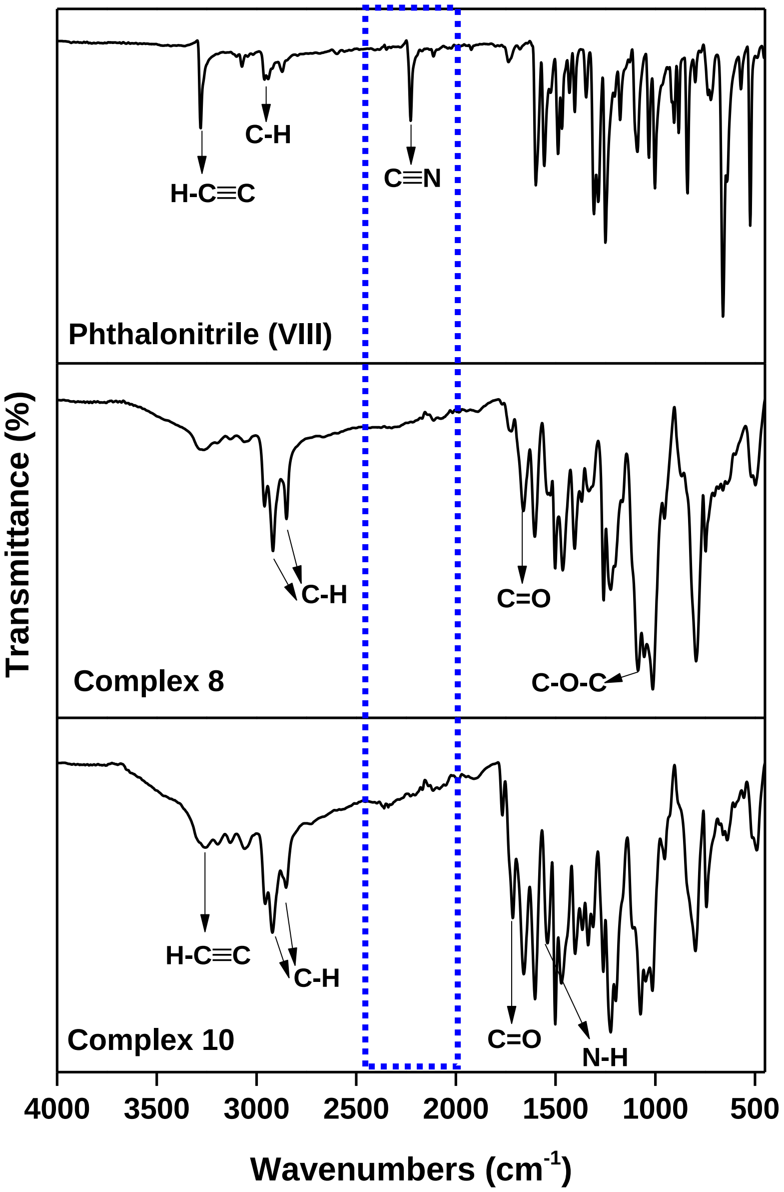

Fig. 3.2: Infrared spectra of complexes **8** and **10** demonstrating the disappearance of the nitrile peak following cyclization of phthalonitrile **VIII**.

For complexes **1**-**6**, stretching frequencies associated with aliphatic groups were observed at the relevant frequencies such as 2850 cm^{-1} and 2918 cm^{-1} due to the pentadecylphenoxy and *tert*-butyl substituents. Broad bands that are a trait of the-OH stretch from carboxylic acids were also observed between the 3000 cm^{-1} and 3500 cm^{-1} region for complexes **1**-**4** and **6**. Regarding complexes **8**-**15**, the carbonyl stretch (C=O) presented itself around the 1660 cm^{-1} region with minor shifts in the different complexes. The amide stretch (-NH), also due to the acetaminophen substituent, appeared at approximately 3257 cm^{-1} in which it overlapped with other functional groups depending on the complex. The elemental analyses also provided confirmation that the compounds of interest had been obtained and purified to a satisfactory level with the values suggesting that some Pcs exist as hydrates [147]. Furthermore, nuclear magnetic resonance (NMR) studies were not conducted due to the paramagnetic nature of the metals used.

3.2 Characterisation of the composites

The ease in which the Pcs and NGQDs were merged into singular nanocomposites through π-π stacking was facilitated by the structural makeup of the NGQDs which consists of planar sheets dominated by a network of *sp*^{2} carbons (**Scheme 3.4**). Complex **12** was also linked to the NGQDs through a covalent bond (an amide bond, **Scheme 3.5**). Using high resolution XPS spectra for C 1s, O 1s, and N 1s, the presence of -NH, -COOH, and -OH groups on the surface of NGQDs has been established [148], hence their depiction in **Schemes S1, 3.4** and **3.5**.

The formation of the amide bond was achieved through the activation of the carboxylic acid terminals on the NGQDs with 1-ethyl-3-(3-dimethylaminopropyl)carbodiimide (EDC) and N-hydroxysuccinimide (NHS) after which, the -NH$_2$ terminal from complex **12** was able to form a new bond with the NGQDs (**Scheme 3.5**). The time applied for the covalent linking was shorter than that which was applied in the π-π stacking to reduce the likelihood of having a composite that is dominated largely by π-π interactions. Although not intended, it is important to note that π-π interactions are also a possibility in addition to the covalent linkage.

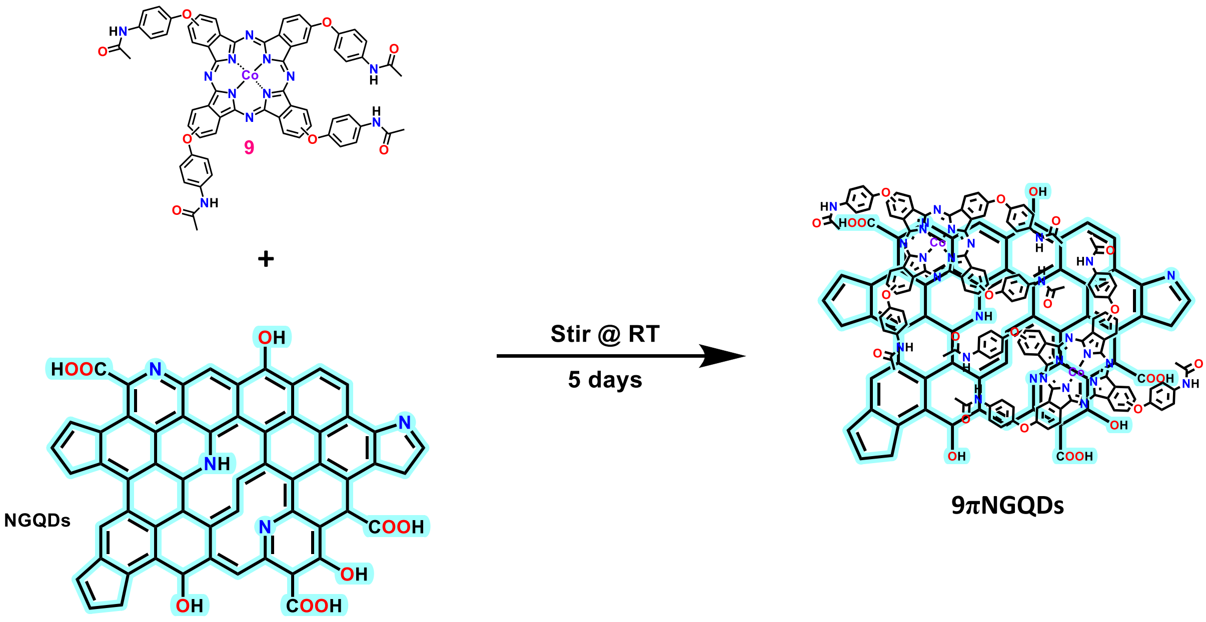

Scheme 3.4: An illustration of how the π-π stacked conjugates were prepared (complex **9** used as the example).

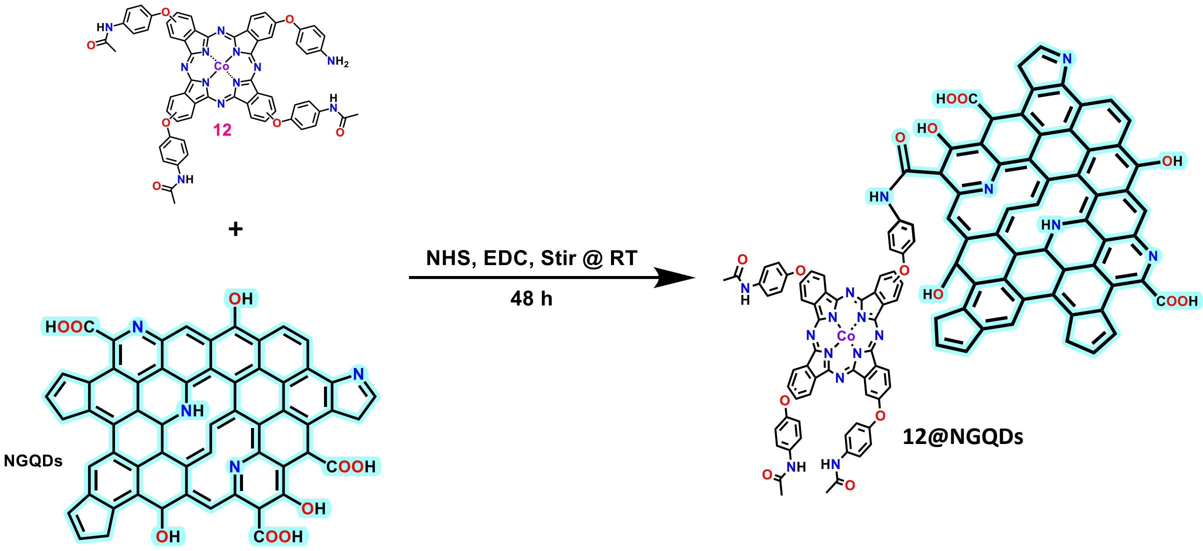

Scheme 3.5: An illustration of how complex **12** was covalently linked to the NGQDs. (NHS = N-Hydroxysuccinimide; EDC = ethyl(dimethylaminopropyl) carbodiimide).

The absorption spectra of complexes **9** and **12** are presented in **Fig. 3.3** alongside that of the conjugates. As observable in **Fig. 3.3**, with respect to the conjugates, the absorption spectra were marked by some spectral shifts of the Q-bands relative to the complexes on their own (**Fig. 3.3A** for complex **9** and **Fig. 3.3B** for complex **12**, **Table 3.2**). For **9πNGQDs**, a blue shift in the Q-band was observed relative to that of complex **9** alone whilst in the case of the composites derived from the asymmetric complex, **12**, for both **12πNGQDs** and **12@NGQDs**, a red shift in the Q-bands was observed (in comparison to complex **12**, **Table 3.2**).

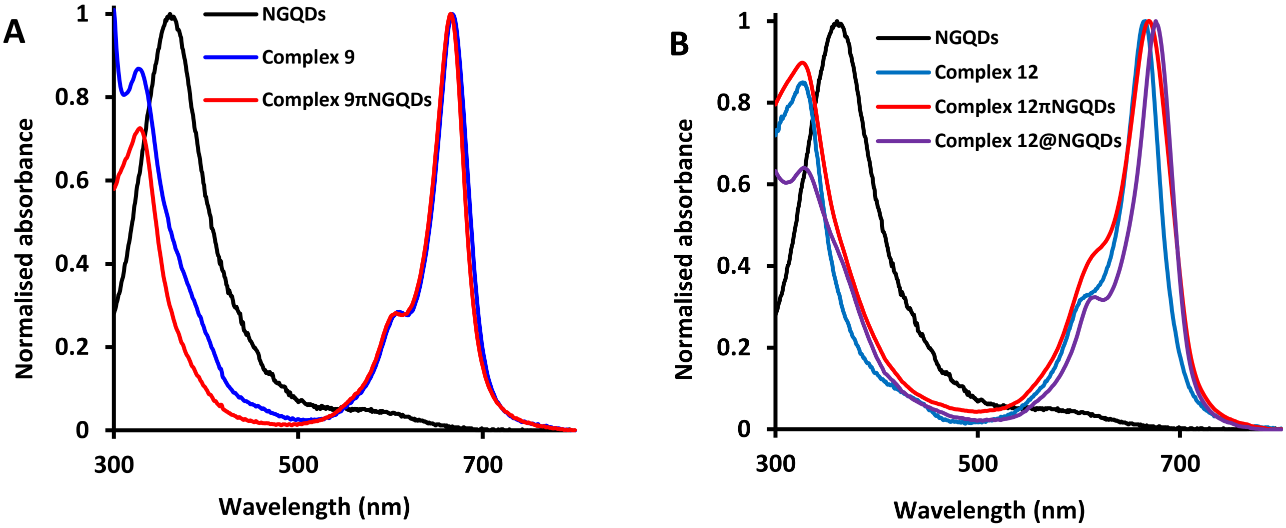

Fig. 3.3: Absorption spectra for complexes **9** (**A**) and **12** (**B**) and their corresponding conjugates in DMF, and the NGQDs in water.

Red shifts in porphyrin-graphene oxide nanoconjugates have been reported to be the result of molecular flattening [149]. The blue shift in **Fig. 3.3A** is an indication of an interaction of Pcs with the surface of the NGQDs. Similar blue shifts upon conjugation of semi-conductor quantum dots to porphyrins have been reported and these were attributed to surface plasma changes as the porphyrin is deposited onto the surface of the quantum dots [150]. For all conjugates, the Q-band retains its characteristic trait of an intense absorption which suggests that conjugation does not have an adverse influence on the structural integrity of the Pc molecule. The increase in absorbance below 400 nm is due to the absorption by NGQDs in **Figs. 3.3A** and **B**.

Consequently, the UV-Vis spectra were applied in determining the loading of Pc to the NGQDs using a method reported in the literature [151], through monitoring the absorbance of the Q-band of the Pc before and after conjugation. The loading for each conjugate was determined with the results presented in **Table 3.2**, where it can be seen that complex **9** in **9πNGQDs** has a better loading than its asymmetric counterparts in **12πNGQDs** and **12@NGQDs**. The loading for complex **12** was lower in the covalently linked conjugate than it was for the π-stacked conjugate which may be due to the spatial orientation of the structures in question.

Table 3.2: A summary of the changes observed following conjugation between the complexes and the NGQDs. (*All absorption spectra in DMF*).

Complex/ nanocomposite	Q band (nm)	DLS size (nm)*	Pc loading (µg Pc /mg Pc-GQDs)	Raman I_D/I_G ratio
9	672	-	-	-
9πNGQDs	665	36.2	80	0.31
NGQDs	-	1.7 (2.4)	-	0.16
12	665	-	-	-
12πNGQDs	670	26.9	20	0.39
12@NGQDs	676	37.1	10	0.43

*Average TEM size in brackets.

The infrared (IR) spectra of the NGQDs, alongside that of complex **12** and the covalently linked conjugate are displayed in **Fig. 3.4**. Functional groups from the paracetamol substituent for complex **12** are observed at 2865 cm^{-1} and 2922 cm^{-1} arising from the aliphatic carbons (**Fig. 3.4**). Due to the similarities in neighbouring atoms, the N-H stretch frequency observed at 3257 cm^{-1} is assigned to either that of the amine group (from the phenoxy substituent) or that present in the paracetamol-based substituent (**Fig. 3.4**). Other functional groups arising from the Pc's main framework (with aromatic-based functional groups possibly overlapping with the phenyl rings in the substituents) are due to stretching/vibrational frequencies at 680 cm^{-1} (aromatic C-H$_{str}$), 1225 cm^{-1} (C-N) and 1462 cm^{-1} (C=C) respectively (**Fig. 3.4**).

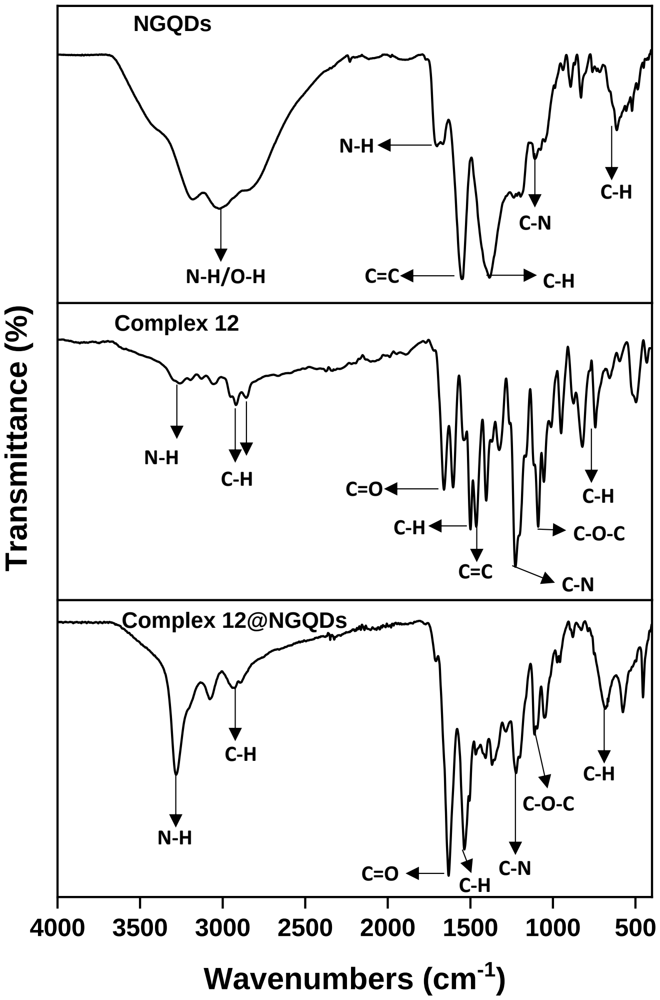

Fig. 3.4: FT-IR spectra of the NGQDs, complex **12** and the corresponding conjugate formed through covalent linking, **12@NGQDs**.

The FT-IR spectrum associated with the covalently linked conjugate, **12@NGQDs**, has traits of both components with subtle differences, suggesting an enmeshment of the two (**Fig. 3.4**). Of interest in this case, are stretching/vibrational frequencies associated with the amide group. Looking at **12@NGQDs**, tentative assignments marked by shifts in stretching or vibrational modes are made where the stretching frequency at 3279 cm^{-1} is assigned to an N-H amide-based stretch with greater transmittance suggesting the presence/creation of more amide bonds. A stretch of medium intensity at 1113 cm^{-1} is ascribed to the C-O stretch (in C-O-C), a slight shift towards a higher frequency relative to when complex **12** is on its own at 1089 cm^{-1} (**Fig. 3.4**). In addition to all the observations reported above, an intense carbonyl stretch makes its appearance at 1630 cm^{-1} (**Fig. 3.4**).

Due to the fact that complex **12** has amide bonds on its own which stem from the acetaminophen substituent, an additional technique was employed to verify the formation of the amide bond between complex **12** and the NGQDs. The X-ray photoelectron spectra (XPS) are shown in **Fig. 3.5** (% atomic compositions shown in **Table 3.3**) which include wide scans of complex **12**, the NGQDs and the conjugate, **12@NGQDs**, as well as the deconvoluted spectra for the O 1s region. The general observation that can be made regarding the wide scans is that one can roughly estimate the presence or quantity of a certain element based on the intensities each element registers. Prior to conjugation, complex **12** has a lower atomic concentration of oxygen and nitrogen than the NGQDs. Following conjugation, the atomic concentration of nitrogen in the conjugate is higher than that observed in complex **12** and the NGQDs separately. Regarding the atomic concentration of oxygen, the value observed in the conjugate is lower than that in the NGQDs alone as the formation of an amide bond is accompanied by the loss of the -OH group from the carboxylic acid terminals (**Table 3.3**).

The O 1s region in complex **12** was deconvoluted to two bands, where the first one at a lower binding energy of 529.5 eV (5007 cps) was assigned to the ether group (C-O-C) while the second one, at a higher binding energy of 530.6 eV (5089 cps), was assigned to the carbonyl oxygen (N-(C=O)) (**Fig. 3.5D**). Three bands, similar to Shi and colleagues [152], were observed in the analysis of the O 1s spectrum associated with the NGQDs (**Fig. 3.5B**). Peak binding energies were observed at 530.4 eV (18660 cps), 531.1 eV (16449 cps) and 532.1 eV (9552 cps) which were assigned to C-O, C=O, (O=C)-O) groups, respectively (**Fig. 3.5B**). The covalently formed conjugate, **12@NGQDs**, yielded five bands upon deconvolution with assignments being made as follows: 528.6 eV (4086 cps) for C-O-C, 529.3 eV (7892 cps) for N-(C=O), 530.0 eV (9965 cps) for C-O, 531.0 eV (6798 cps) for C=O and 532.4 eV (3419 cps for (O=C)-O, (**Fig. 3.5F**). What is of importance in this instance is the increase in the intensity of the band associated with the amide carbonyl N-(C=O) from 5089 cps for complex **12** alone to 7892 cps for **12@NGQDs**. There was a decrease in the intensity of the band assigned to the (O=C)-O group in the carboxylic acid of NGQDs (from 9552 cps to 3419 cps of the conjugate), which was ascribed to the loss of the -OH upon the formation of the amide bond. Overall, there was a general decline in all the other bands due to a decrease in the original starting material.

Table 3.3: Atomic percentages from the XPS analyses.

	% C	**% N**	**% O**
Complex 12	93.3	2.35	4.37
NGQDs	67.0	6.94	36.1
12@NGQDs	69.1	15.1	15.8

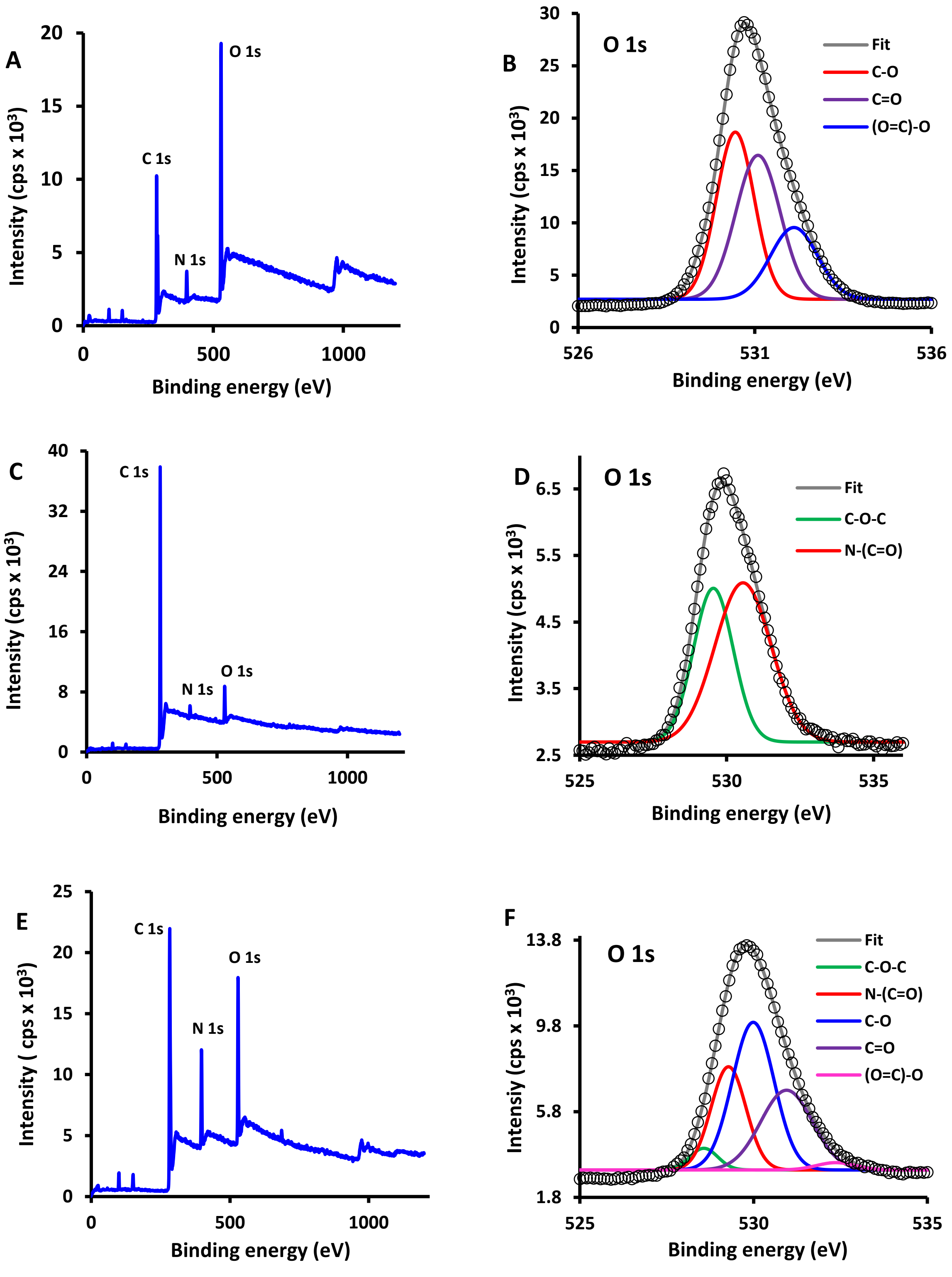

Fig. 3.5: XPS wide scans for the NGQDs (**A**), complex **12** (**C**) and the covalently linked conjugate, **12@NGQDs** (**E**), and the corresponding deconvoluted O 1s spectra (**B**, **D**, and **F**).

An assessment of the order/disorder of the graphene network that forms the NGQDs was performed (using Raman spectroscopy) to better understand the effects that conjugation has on the graphene matrix. Shifts in both the D and G bands were observed (**Fig. 3.6**). The Raman spectral shifts towards either the blue or red regions are attributed to the differences in the forces (compressive versus tensile) that act on the graphene framework [153,154].

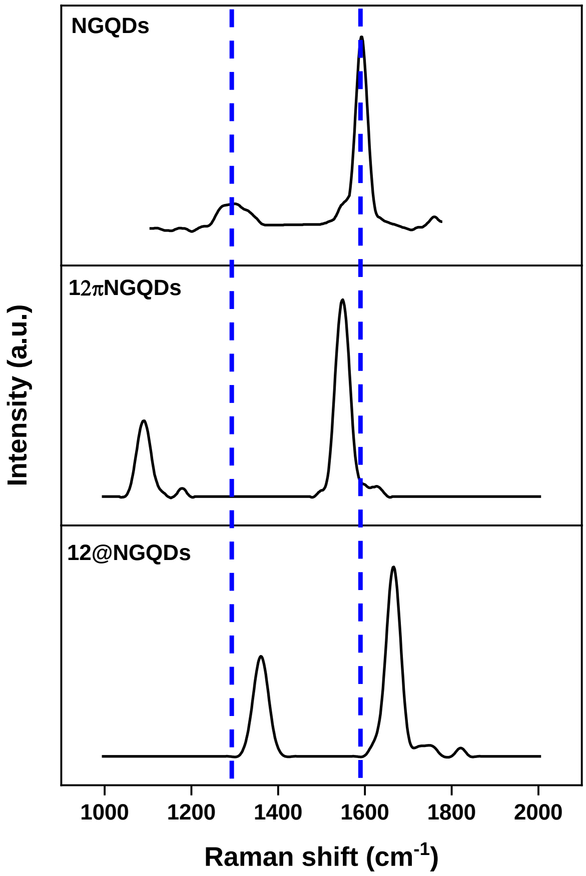

Fig. 3.6: Raman spectra for complex **12** and its respective conjugates, **12πNGQDs** and **12@NGQDs**.

Compressive forces are those that result in pushing atoms towards each other while tensile forces stretch bonds, resulting in atoms being pulled further from each other. The change in I_D/I_G ratios along with the Raman shifts in both the D and G bands are ascribed to the interactions between the NGQDs and complexes (**9** and **12**) after conjugation. The effects of conjugation of carbon nanomaterials are often quantified by the I_D/I_G ratio where a low I_D/I_G ratio is often associated with a low level of disorder whilst a high I_D/I_G ratio corresponds to a high level of disorder in the graphene network. The I_D/I_G ratios observed were greater than that of the NGQDs alone. The I_D/I_G ratios presented in **Table 3.2** are as follows: 0.16, 0.31, 0.39 and 0.43 and for the NGQDs, **9πNGQDs**, **12πNGQDs** and **12@NGQDs** respectively. Lower I_D/I_G values were recorded for the π-stacked conjugates relative to the composite derived from covalent linking. This may be due to the Pc and their substituents assuming spatial positions that cause minimal strain to the graphene matrix, unlike the covalently formed nanocomposite which may result in the occurrence of pulling forces (tensile forces) caused by the formation of new bonds between the NGQDs and the Pc.

The average size of the NGQDs was determined using both transmission electron microscopy (TEM) and dynamic light scattering (DLS) (**Figs. 3.7** and **A16** in the appendix). From the TEM image showing monodispersed particles in **Fig. A16**, the average size distribution was 2.4 nm whilst an average size of 1.7 nm was recorded using DLS (**Table 3.2**). While it is often the case that the DLS size exceeds the TEM size due to the dispersing agent possibly increasing the hydrodynamic diameter, this was not the case [155]. This observation, however, is not an isolated one as similar reports based on ceramic nanoparticles have made where the TEM size is slightly greater than the DLS size [155]. In estimating the average size of the conjugates, DLS alone was used as the conjugates are insoluble in ethanol and acetone, which are considered to be the more suitable of solvents in the preparation of samples for TEM analysis [156]. In addition to that, other organic solvents such as DMF form solvent layers upon drying which may damage the support layer on the TEM grid [157].

From the TEM micrographs in **Fig. 3.7**, the average particle size of the NGQDs following conjugation to the complexes was shown to have increased from 1.7 nm to between 26.9 nm and 37.1 nm (**Table 3.2**). In addition to influences from the dispersant, an enhancement in the electron density after conjugation may also account for the sizes observed. Taking these factors into consideration, these sizes may not necessarily reflect the actual size of a single nanocomposite as these elements promote the formation of clusters (conjugates may be smaller). These clusters, often referred to as aggregates, are a common occurrence in Pc-GQDs or other Pc-nanoparticle composites [**158**,**159**].

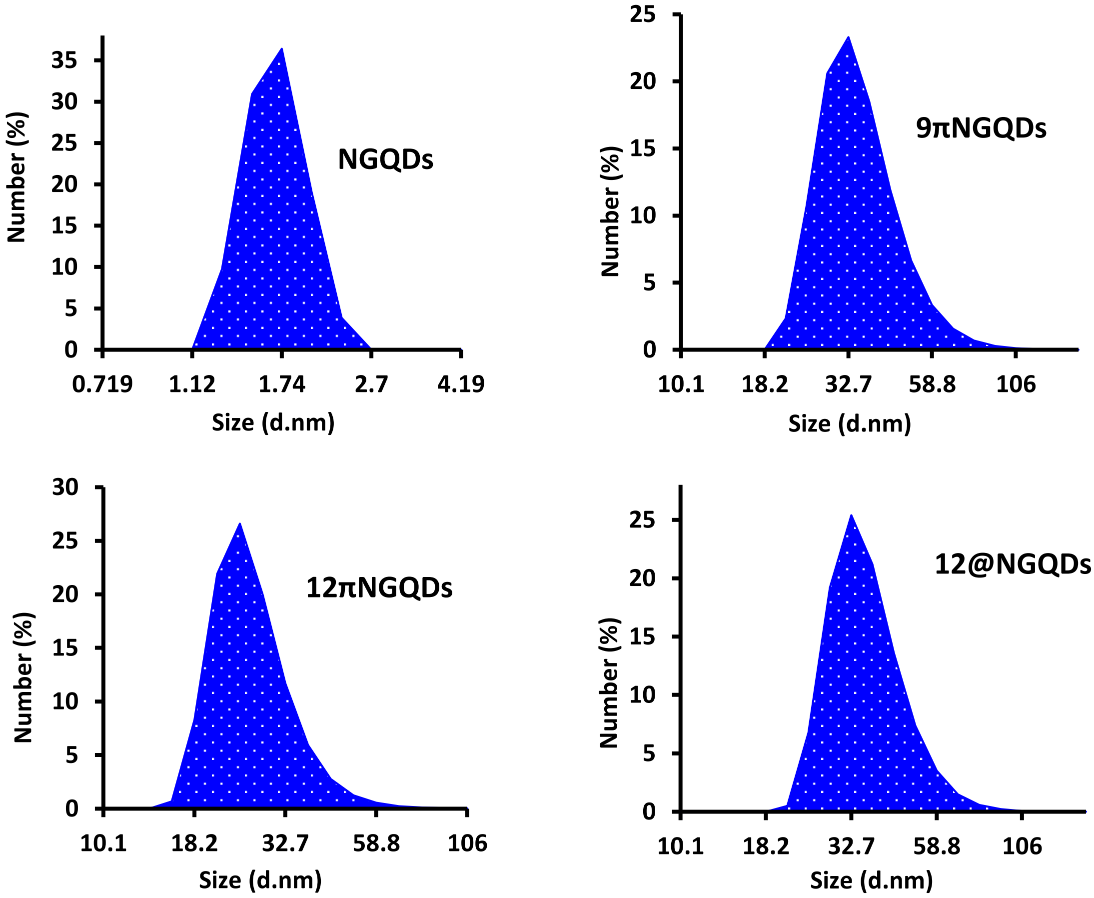

Fig. 3.7: DLS area plots illustrating the average particle sizes for the NGQDs and their conjugates with the CoPcs, complex **9** and **12**.

3.3 Summary of chapter

Cobalt and manganese phthalocyanines along with the NGQD-conjugates were synthesized/prepared and characterised using an array of spectroscopic techniques. The results obtained from the characterisation confirmed that the proposed structures were synthesized and purified to a satisfactory level. The IR spectra showed the disappearance of the nitrile stretching frequency in the phthalonitrile precursors indicating that cyclization was successful. The mass spectral data was also in support of the expected atomic masses for the complexes synthesized. Apart from one Pc, a monomeric Q-band was observed for all the Pcs. The aggregation observed in the one Pc, complex **15**, was resolved through the addition of Triton X-100. Furthermore, with respect to the MnPcs, the observed redshifts in the Q-band maxima were used to correctly assign the oxidation state of the central metal, Mn^{3+}. An analysis of the nanocomposites was also performed with the spectral information observed from the absorption spectra, the IR, Raman and XPS all confirming that indeed the conjugation was achieved.

CHAPTER 4

ELECTRODE CHARACTERISATION

Chapter 4 provides a detailed discussion on the results obtained from the characterized electrode surfaces.

4. Characterisation of the modified electrodes

4.1 Characterisation in a ferrocyanide-ferricyanide solution

The methods applied in modifying the electrodes are described extensively in **Chapter 2**. In this section, the focus lies on the characterization of the modified electrode surfaces. Upon modification, characterization of the electrodes was performed using several electrochemical techniques including cyclic voltammetry (CV), electrochemical impedance spectroscopy (EIS), scanning electrochemical microscopy (SECM), linear sweep voltammetry (LSV) and chronocoulometry. The electron-transferring abilities of the designed probes were studied using a ferrocyanide-ferricyanide solution ($[Fe(CN)_6]^{3-/4-}$, in 0.1 M KCl as the redox mediator. Although there are other redox probes available such as ruthenium-based redox mediators, the iron-based probe was selected due to its high stability, reversibility and as well as sensitivity to the surface kinetics of the electrode used in these studies, a glassy carbon electrode (GCE) [160-162]. Cyclic voltammetry was applied in the electrolytic media to assess the activity of the probes in those solutions, to aid in distinguishing the electrochemical responses in the absence and presence of the analytes under study. LSV and chronocoulometry were used in determining the active electrode area and surface coverage, Γ.

Regarding the electrodes surfaces modified through click chemistry, an additional non-electrochemical characterization technique was applied to ensure that the triazole ring was formed as intended. In the same way that the electrode was modified, glassy carbon plates were subjected to the same treatment and analysed using X-ray photoelectron spectroscopy (XPS). The mechanism describing the way in which click chemistry proceeds is described pictorially in **Scheme 4.1**.

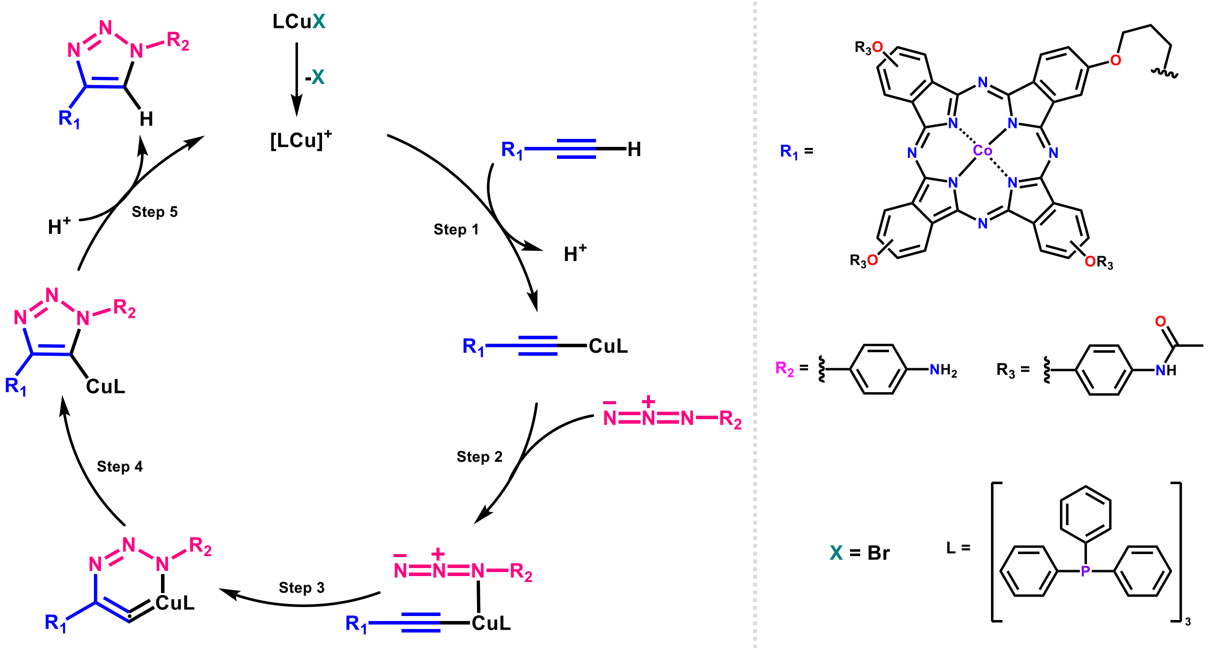

Scheme 4.1: Mechanism illustrating how the triazole ring is formed by means of the Sharpless copper (I) catalysed azide-alkyne cycloaddition reaction (complex **8** used as an example).

The mechanism describing how the triazole ring is formed can be described as follows [**163**]:

- **Step 1**: Deprotonation of the alkyne terminal followed by coordination of the copper catalyst with the alkyne group.
- **Step 2**: A displacement of one of the copper ligands by the azide group occurs where the azide takes the place of one of the ligands.
- **Step 3**: An unstable six-membered ring is formed where the triple bonds in both the alkyne and azide groups are converted in double bonds.
- **Step 4**: Stabilization through contraction of the six-membered ring into a five-membered ring takes place.
- **Step 5**: Protonolysis of the copper catalyst takes place after which the end product is formed (the triazole ring).

4.1.1 Cyclic voltammetry

Cyclic voltammetry is one of the simplest tools used to gauge the electron-transporting behaviour of electrode surfaces. By looking at the profile of the cyclic voltammogram, inferences as to whether the electron processes are reversible, quasi-reversible or irreversible in their nature can be made [164]. Quantitatively, by obtaining the difference between the peak anodic potential and peak cathodic potential (ΔE_p), greater certainty can be applied to these inferences.

Theoretically, an electrode with desirable electron-transferring abilities possesses a ΔE_p value of approximately 60 mV or closer [165]. Coincidentally, this value is also used as a marker to assess the cleanliness of an electrode surface as it is often subject to change once the surface has been altered chemically or otherwise. In most cases, following the introduction of an electrocatalyst onto the surface, the ΔE_p value increases suggesting slow electron-transportation abilities. Apart from either an increase or decrease in the ΔE_p value, some methods of electrode modification such as grafting yield voltammograms that are synonymous with complete surface passivation as there is neither an anodic nor cathodic signal observed. Nonetheless, these observations, particularly those where there is either an increment in the ΔE_p value or the absence of definitive redox signals, have minimal implications as to how the modified electrode surface will respond to the analyte under study. A summary of the ΔE_p values of all the probes investigated is provided in **Table 4.1** with cyclic voltammograms of some of the electrodes being presented in **Fig. 4.1**.

Table 4.1: ΔE_p and resistance-to-charge (R_{CT}) values for all modified electrodes in $[Fe(CN)_6]^{3-/4-}$ (in 0.1 M KCl).

Probe	ΔE_p (mV) (vs Ag|AgCl)	R_{CT} (kΩ)	Γ (mol/cm^2)	Γ (mol/cm^2)^d
Bare GCE	73	0.18	c	c
GCE-NGQDs	187	4.51	c	c
GCE-1A	341	20.6	2.72×10^{-7}	3.40×10^{-10}
GCE-2A	204	27.5	2.22×10^{-7}	2.88×10^{-10}
GCE-3A	a	24.7	1.65×10^{-7}	1.39×10^{-10}
GCE-4A	a	24.1	c	c
GCE-5A	285	36.5	3.65×10^{-6}	2.62×10^{-9}
GCE-6A	224	26.5	2.92×10^{-7}	2.93×10^{-10}
GCE-7A	332	28.9	3.72×10^{-7}	5.25×10^{-10}
GCE-8A	266	74.3	2.10×10^{-7}	2.47×10^{-10}
GCE-8C	a	b	c	c
GCE-9A	275	30.4	8.40×10^{-7}	1.18×10^{-10}
GCE-9πNGQDs	106	19.4	1.31×10^{-7}	2.47×10^{-10}
GCE-10A	483	323	6.57×10^{-8}	8.48×10^{-11}
GCE-10C	a	b	c	c
GCE-11A	486	361	c	c
GCE-12A	109	19.1	1.32×10^{-7}	1.24×10^{-10}
GCE-12πNGQDs	612	28.2	6.08×10^{-8}	1.22×10^{-10}
GCE-12@NGQDs	446	22.0	8.69×10^{-8}	1.14×10^{-10}
GCE-13A	401	14.4	7.77×10^{-8}	1.17×10^{-10}
GCE-14A	407	14.9	6.28×10^{-8}	8.69×10^{-11}
GCE-15A	413	15.0	6.39×10^{-8}	9.66×10^{-11}

a – No reverse peak; b – not determined; c – no peak/signal in the buffer, d – surface coverage determined from geometric area of electrode.

The ΔE_p values shown in **Table 4.1** present no definitive trend as far as the substituents of the Pcs are concerned except that all the probes are seemingly poor conductors (i.e. high ΔE_p values) with the exception of the bare GCE (ΔE_p = 73 mV). The electrodes modified through click chemistry yielded no redox signals as illustrated in **Fig. 4.1** with **GCE-8C** provided as an example (hence the absence of a ΔE_p value in **Table 4.1**).

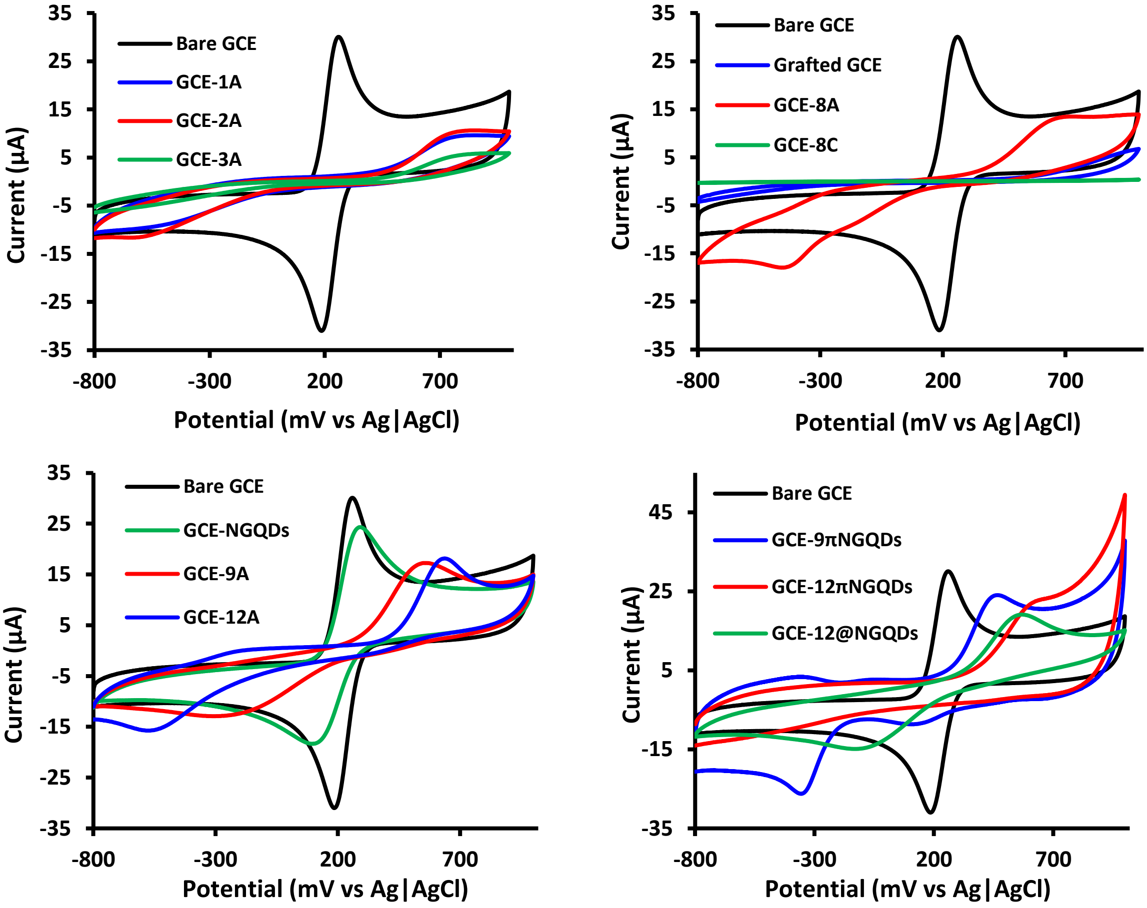

Fig. 4.1: Cyclic voltammograms of the bare and some of the modified electrodes in 1 mM $Fe(CN)_6^{3-/4-}$ (in 0.1 M KCl), all at a scan rate of 100 mV/s.

With respect to the ΔE_p values, the overall summary regarding the analysis of the electrodes in the ferri-/ferrocyanide redox probe can be described as follows:

- The bare GCE appears a good conductor of electrons as the value observed was 73 mV, which is close to the Nernstian value for a surface studied in the $Fe(CN)_6]^{3-/4-}$ redox couple.
- Regarding the series of pentadecylphenoxy-substituted complexes, the order of electrodes in terms of the lowest to the highest ΔE_p value is as follows:

  GCE-2A > **GCE-5A** > **GCE-1A**

  - No definitive redox signals were observed for **GCE-3A** and **GCE-4A**.
- As for the *tert*-butyl bearing Pcs, the asymmetric complex yielded a lower ΔE_p value than its symmetrical counterpart (**GCE-6A** > **GCE-7A**), which may suggest that the reduction in symmetry improves the electrode kinetics.
- With respect to the Pcs that possess acetaminophen as the primary substituents, the order of electrodes regarding the most desirable (lowest ΔE_p) was as follows:

  GCE-12A > **GCE-8A** > **GCE-9A** > **GCE-13A** > **GCE-14A** > **GCE-15A** > **GCE-10A** > **GCE-11A**

  - No definitive redox signals were observed for **GCE-8C** and **GCE-10C**.
- Overall, in terms of the Pcs alone, complex **12** in **GCE-12A** displayed the most desirable of electron-transferring abilities with a ΔE_p value of 109 mV.
  - The highest ΔE_p value was recorded for **GCE-11A** with a value of 486 mV which may be due to the axially ligated central metal (i.e. Mn^{3+} fosters slower electron transportation relative to Co^{2+}).
  - In general, the CoPcs had lower ΔE_p values than the MnPcs (comparing **GCE-8A** with **GCE-10A**, and **GCE-9A** with **GCE-11A**).

- In terms of the ΔE_p, from the lowest to the largest, the probes fashioned from the nanocomposites were ranked as follows:

  GCE-9πNGQDs > **GCE-12@NGQDS** > **GCE-12πNGQDs**

  - The addition of NGQDs improved the electron-transferring abilities for the symmetric complex (**GCE-9πNGQDs** > **GCE-9A**) and seemed to have an adverse effect on that of the asymmetric complex **12** for both probes involving the covalent and non-covalent conjugates (**GCE-12@NGQDs** and **GCE-12πNGQDs**).
  - The covalently formed composite **GCE-12@NGQDs** produced a lower ΔE_p than the π-stacked conjugate in **GCE-12πNGQDs** which may be attributed to the lower loading (in terms of the quantity of the Pc within the whole nanocomposite) for the former as recorded in **Table 3.2**.

4.1.2 Electrochemical impedance spectroscopy (EIS)

Electrochemical impedance spectroscopy is an analytical technique used to characterize electrode surfaces by measuring either the impedance or capacitance of a particular surface in solution [166]. Based on the impedance or resistance-to-charge (R_{CT}) value, inferences on the electron-transportation abilities of the electrodes under investigation can be made [166]. Quite often, a large R_{CT} value, usually distinguished by a Nyquist plot bearing a large semi-circle, is associated with poor or limited electron-transferring abilities [167]. From **Fig. 4.2** (Nyquist plots fitted using a Randles-Sevcik equivalent circuit with the inclusion of a Warburg constant) and the R_{CT} values recorded in **Table 4.1**, deductions were made as follows:

- A low R_{CT} value of 0.18 kΩ was registered for the bare GCE, showing good conductivity.

- In terms of the Pcs alone, complex **13** in **GCE-13A** displayed the most desirable of electron-transfer abilities with an R_{CT} value of 14.4 kΩ.
    - The highest R_{CT} value was recorded for **GCE-11A** with a value of 361 kΩ which corresponds with the ΔE_p value.
- Regarding the series of pentadecylphenoxy-substituted complexes, the order of electrodes in terms of the most favourable R_{CT} value (i.e. lowest) is as follows:

GCE-1A > **GCE-4A** > **GCE-3A** > **GCE-2A** > **GCE-5A**

- As for the *tert*-butyl bearing Pcs, the asymmetric complex yielded a lower R_{CT} value than its symmetrical counterpart (**GCE-6A** > **GCE-7A**), demonstrating the benefits of asymmetry.
- With respect to the Pcs that possess acetaminophen as the primary substituents, the order of electrodes regarding the most desirable (i.e. a low R_{CT}) is as follows:

GCE-13A > **GCE-14A** ≥ **GCE-15A** > **GCE-12A** > **GCE-9A** > **GCE-8A** > **GCE-10A** > **GCE-11A**

-
    - The above observation confirms that **GCE-11A** is indeed dominated by slower electron kinetics as witnessed with the ΔE_p value as well.
- Relative to the complexes alone, the NGQDs yielded the lowest R_{CT} value (4.51 kΩ) which may be attributed to the similarities in the arrangement of atoms between the bare GCE and the NGQDs.
- The probes fashioned from the nanocomposites followed the same order as the results for the ΔE_p and were ranked as follows:

GCE-9πNGQDs > **GCE-12@NGQDS** > **GCE-12πNGQDs**

-
    - The addition of NGQDs improved the electron-transferring abilities for the symmetric complex (**GCE-9πNGQDs** > **GCE-9A**) and seemed to have an adverse

effect on that of the asymmetric complex **12** for both probes involving the covalent and non-covalent conjugates (**GCE-12@NGQDs** and **GCE-12πNGQDs**).

- The covalently formed composite **GCE-12@NGQDs** produced a lower R_{CT} than the π-stacked conjugate in **GCE-12πNGQDs** which may be ascribed either to the loading as recorded in **Table 3.2**, the nature of the conjugate (i.e. π-stacked versus covalently linked) or a combination of the two.
- The results observed for the nanocomposites were in good agreement with the ΔE_p results observed.

Quite often, a large ΔE_p value is accompanied by a large R_{CT} value as both are predictors of charge transferring capabilities however [167], this trend was not necessarily linear in the electrodes presented. The manner in which the EIS results were in agreement with the ΔE_p values was in an isolated form where the results are agreeable in terms of the complexes on their own and their corresponding conjugates, and not taking into consideration all probes (**Table 4.1**). Looking at the summary of these observations in **Table 4.1**, it is evident that while the two techniques are considered complementary to one another, the difference in their sensitivities is useful in unmasking factors which may or may not contribute to the discrepancies observed. These differences may be ascribed to the $Fe(CN)_6^{3-/4-}$ redox probe kinetics and/or a technique's sensitivity to the concentration of the electrolyte, or simply non-ideal behaviour [168]. In addition to those factors, deviations from Ohm's law caused by electron-electron short-range repulsion as well as the deviations from the desired carbon nanostructure may account for the discrepancies observed in the ΔE_p and R_{CT} values [169,170].

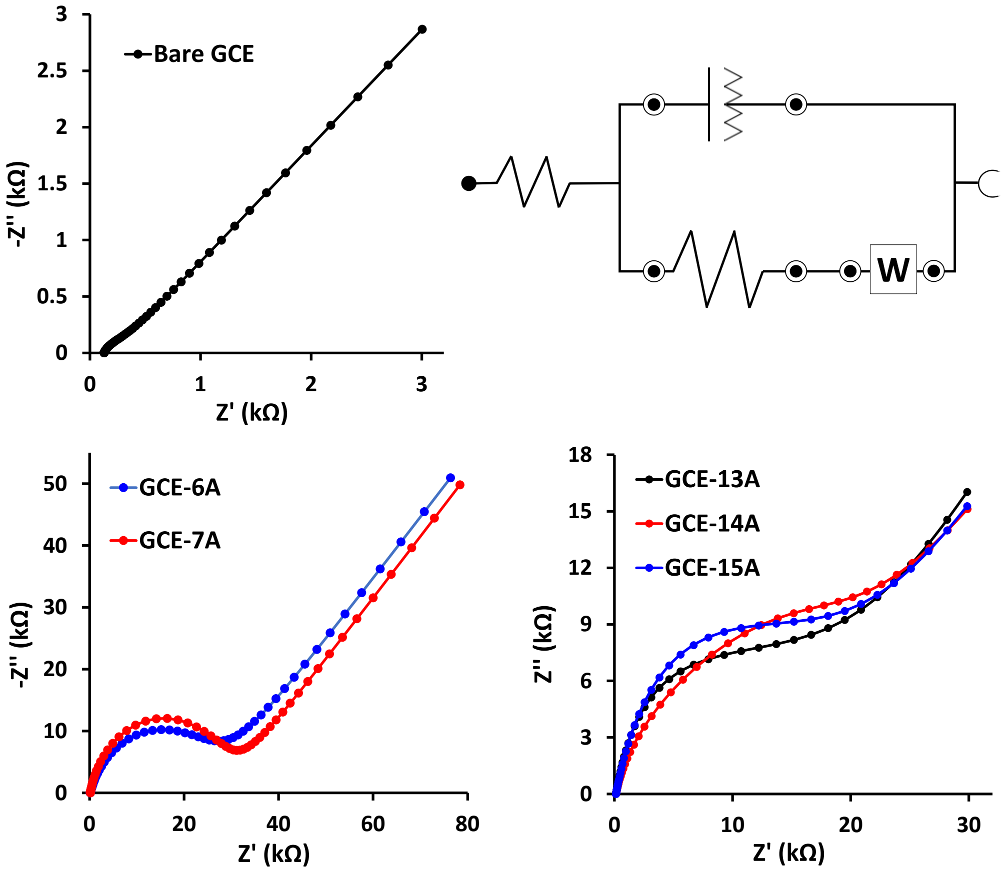

Fig. 4.2: Nyquist plots obtained from the electrodes characterized in 1 mM Fe(CN)$_6^{3-/4-}$ (in 0.1 M KCl) and the Randles-Sevcik circuit used for fitting.

4.1.3 Scanning electrochemical microscopy (SECM)

Scanning electrochemical microscopy (SECM) is an analytical technique used to characterize electrodes at the microscopic level [171]. The technique makes use of an ultra-micro electrode (UME) to record the current generated from the electrochemical interactions between the UME and the relevant material (**Fig. 4.3**) [171]. In a feedback type of system, through the introduction of a redox probe, a Fe^{3+}/Fe^{2+} redox mediator in this case, the conductivity of an electrode surface can be assessed through observing the change in the current [171,172]. When the redox probe is oxidized or reduced, and produces the corresponding product, a positive feedback response will be observed through an increment in the current of the UME. In the event that the substrate is inactive (i.e. an insulator), where neither oxidation or reduction take place, and the current decreases, a negative feedback response is recorded [171].

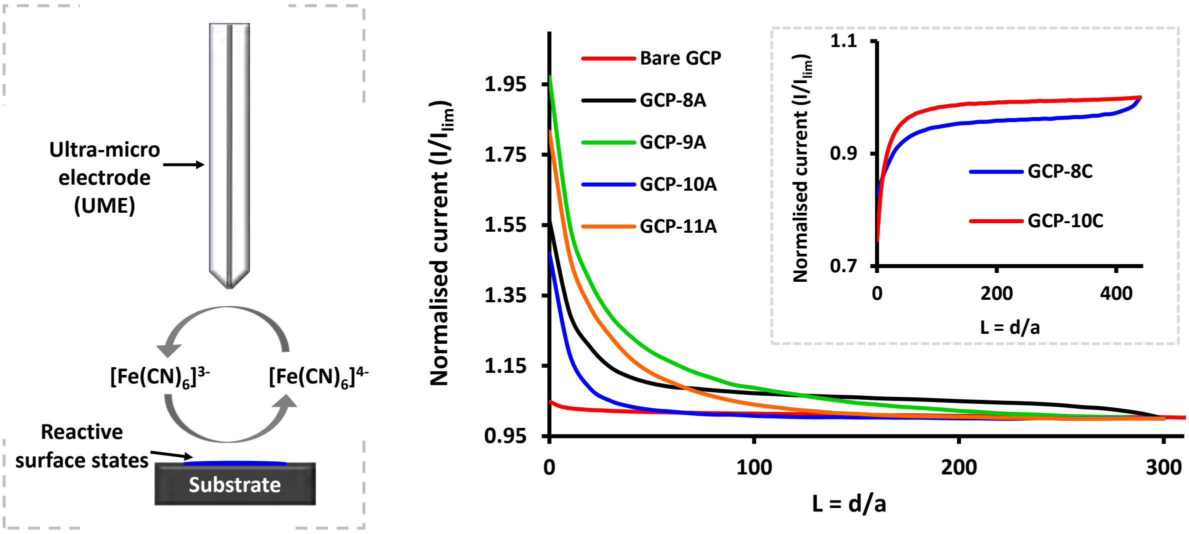

Fig. 4.3: Schematic diagram of the primary components of SECM (with the substrate being the modified carbon plate) and the resulting approach curves of probes investigated in 1 mM $[Fe(CN)6]^{3-}/^{4-}$in 0.1 M KCl at -1.5 V Inset: approach curve for the clicked plates, **GCP-8C** and **GCP-10C**. (L = d/a represents the ratio of tip-substrate to UME tip radius).

Looking at the approach curves in **Fig. 4.3**, the approach curves for the carbon plates modified through adsorption all follow a trajectory that is synonymous with conductive surfaces with a significantly higher current than the bare carbon plate, while the surfaces altered through click-chemistry produce a profile that corresponds with non-conductive surfaces. Similar observations involving an iron Pc (FePc) have been made where the Pc after being clicked onto a glassy carbon plate produces the same profile as that which is observed in the inset in **Fig. 4.3** [108]. The observations made in **Fig. 4.3** are all in support of the cyclic voltammograms presented in **Fig. 4.1** in that the adsorbed surfaces elicit conductive behaviour whilst the clicked surfaces, appear to be insulators in their nature. Variations in the approach curve profiles were observed for the other electrode surfaces in which some followed those of an insulator (**GCP-8C** and **GCP-10C**) whilst other substrates indicated conductive behaviour.

4.2 Characterisation in the buffers

The analysis of the modified electrodes was also performed in the buffer solutions prior to the addition of the analyte(s). Cyclic voltammetry was used to identify the presence of any redox peaks in the buffer solution/aqueous medium before adding the analyte. The purpose of this was to ascertain that there no contaminants in the buffer solution/aqueous medium that may yield a signal that may interfere with the one observed following the addition of the analytes.

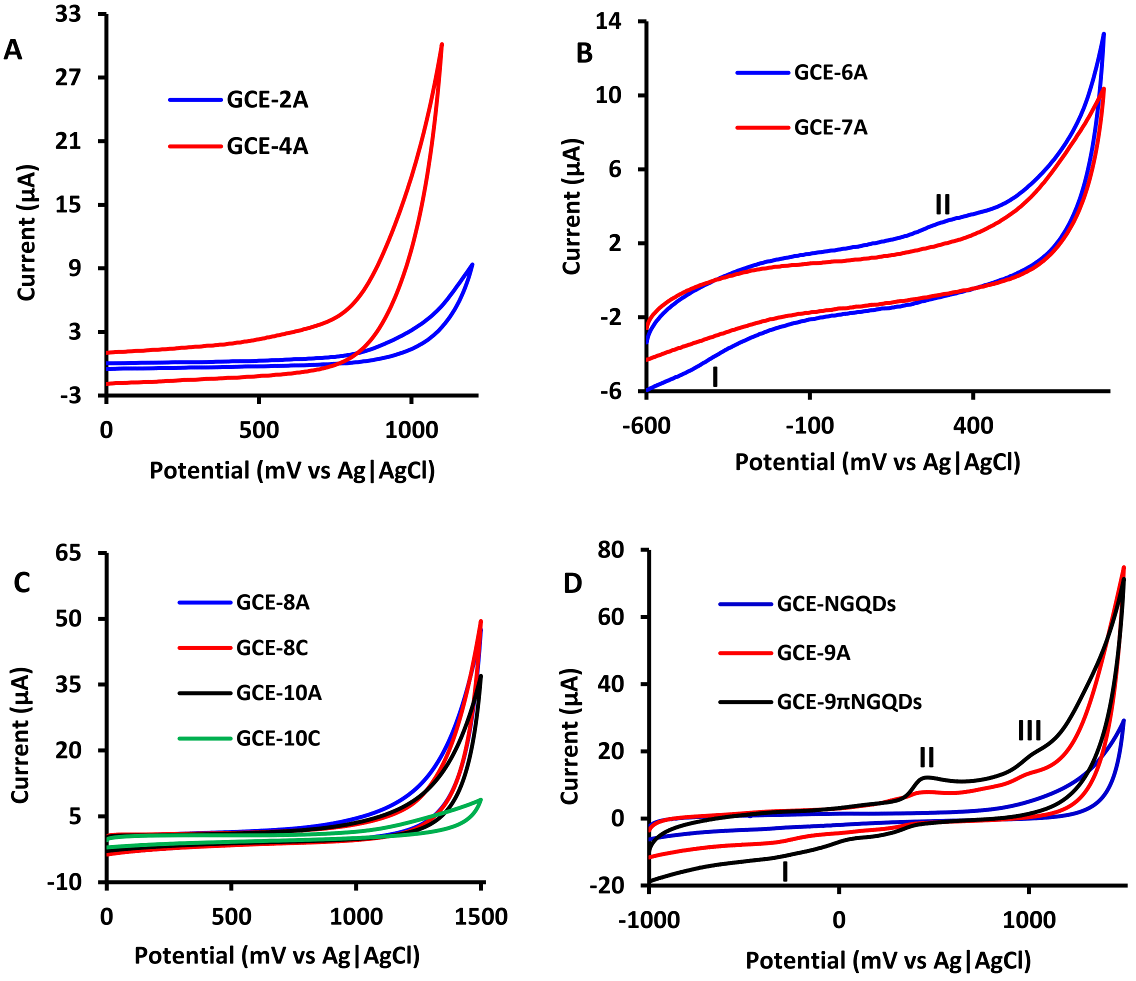

Fig. 4.4: Cyclic voltammograms of the modified electrodes in 0.1 M NaOH and (**A** and **B**) and in 0.1 M PBS, pH 7.5 (**C** and **D**), in the absence of the analytes.

This was also to ensure that the electrochemical responses observed are the result of the analytes and nothing else. The cyclic voltammograms in **Fig. 4.4** are of the modified electrodes in the absence of the analytes where **Figs. 4.4A** and **4.4B** are in 0.1 M NaOH (for the electrocatalysis of hydrazine) and **Figs. 4.4C** and **4.4D** are in 0.1 M of a phosphate buffer solution (PBS, for the electrochemical oxidation of nitrite).

The voltammograms in **Fig. 4.4A** present no redox signals whilst some redox activity is observed in **Fig. 4.4B** from **GCE-6A**. Despite being in the same medium, 0.1 M NaOH, it is evident that the probes are different hence different voltammetric responses are observed. The redox peaks labelled **I** and **II** in **Fig. 4.4B** were, based on the literature, assigned to $Co^{II}Pc^{-2}/Co^{I}Pc^{-2}$ and $Co^{III}Pc^{-2}/Co^{II}Pc^{-2}$ processes, respectively [173].

The observations made in PBS were not uniform either as some of the probes appeared active even in the absence of the analyte (**Fig. 4.4D**). Looking at **Fig.4.4D**, the peak labelled **I** was assigned to $Co^{II}Pc^{-2}/Co^{I}Pc^{-2}$, an observation that has been previously reported in CoPc containing electrodes [173]. The peaks labelled **II** were ascribed to $Co^{III}Pc^{-2}/Co^{II}Pc^{-2}$ processes while **III** were proposed to be due to ring-based processes [173]. Regarding the MnPc in **GCE-11A** (not shown in **Fig. 4.4**), a redox signal at approximately 60 mV was observed and was assigned to the $Mn^{III}Pc^{-2}/Mn^{II}Pc^{-2}$ redox couple based on previous literature involving similar MnPcs (**Table 4.2**) [91].

4.3 Determination of the surface coverage

Chronocoulometric experiments were carried out in the redox probe to enable the determination of the effective area of the electrode. In order to oxidize $Fe(CN)_6^{3-}$ (*aq*) to $Fe(CN)_6^{4-}$ (*aq*), the potential was stepped from 0.0 V to 1.0 V which produced a chronocoulometric graph (**Fig. 4.5A**, **GCE-12A** as an example). This figure (**Fig. 4.5A**) was converted to a charge (C) vs time$^{1/2}$ (s) graph (**Fig. 4.5B**) and further used to determine the surface area of the electrode from the integrated Cottrell equation (**Eq. 4.1**) [173]:

$$Q = \frac{2nFAD^{1/2}C_o t^{1/2}}{\pi^{1/2}} \tag{4.1}$$

In which the slope is equivalent $2nFAD^{1/2}C_o\pi^{-1/2}$. By equating the slope to $2nFAD^{1/2}C_o\pi^{-1/2}$ and using values from the literature where n is equivalent to 1, D is equal to 7.6 x 10^{-6} cm^2/s [174,175], F being Faraday's constant, A being the area and C_o being the concentration of the ferri-/ferrocyanide solution, the electrode area was determined for all the electrodes.

In combination with the area obtained from using **Eq. 4.1**, the effective surface coverage was calculated from equation 4.2 (**Eq. 4.2**) as expressed in previous reports [173]:

$$\Gamma = \frac{Q}{nFA} \tag{4.2}$$

where Γ represents the surface coverage, Q the electrical charge integrated from the area assigned to the Co$^{II/III}$ process (Mn$^{II/III}$ for the MnPcs were applicable), from the linear sweep voltammetry (**Fig. 4.6**), n the number of electrons involved (n = 1), F being Faraday's constant and A, the effective area (calculated using **Eq. 4.1**).

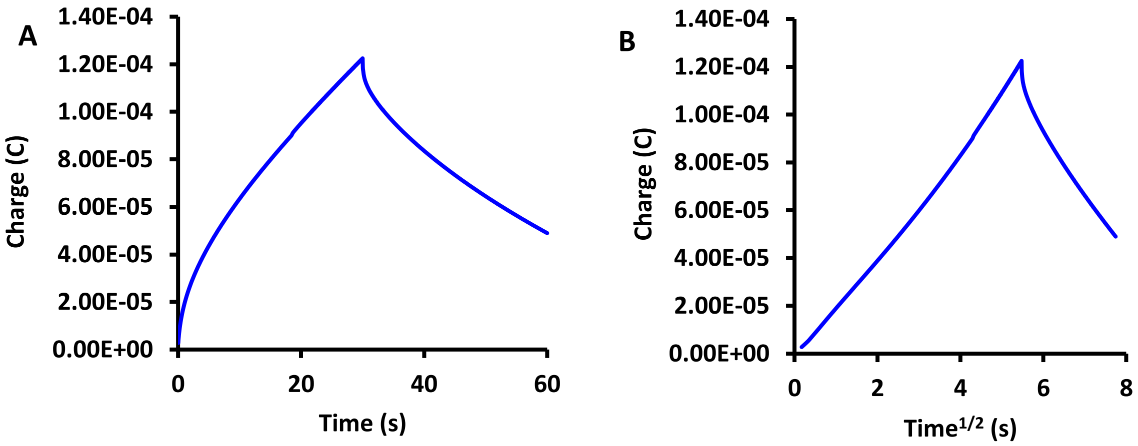

Fig. 4.5: Chronocoulometric data for **GCE-12A** in 1.0 mM ferricyanide in 0.1 M of KCl (**A**) and its converted counterpart (**B**).

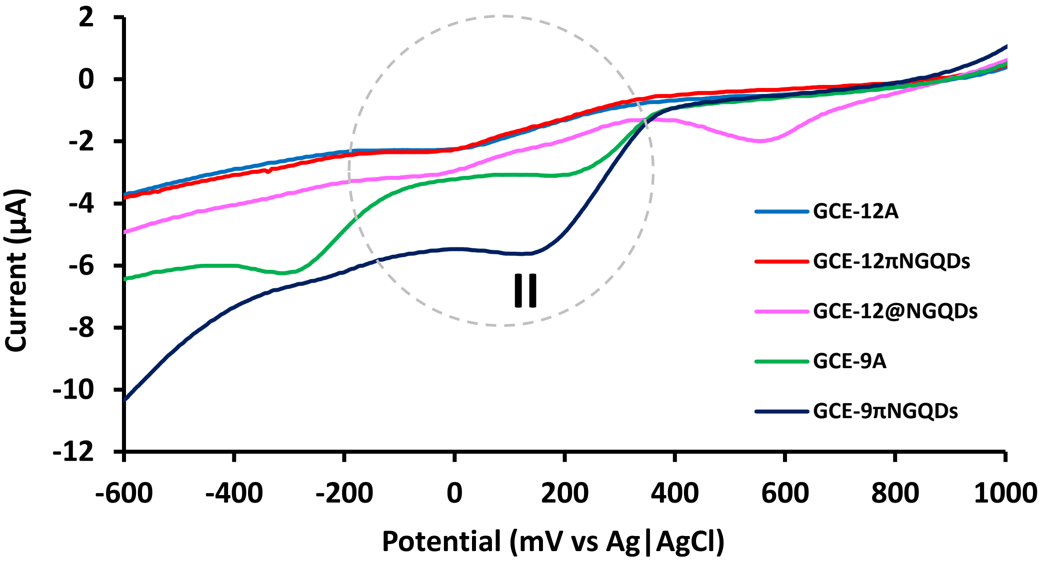

Fig. 4.6: Linear sweep voltammograms of a selection of the modified electrodes in the absence of nitrite at a scan rate of 50 mV/s (in 0.1 M PBS, pH 7.5).

The Γ values estimated ranged from 8.69 × 10^{-8} mol/cm^2 to 3.65 × 10^{-6} mol/cm^2 with the bulk of the electrodes possessing an exponential of 10^{-7}, which is a significant difference relative to what has been reported for similar phthalocyanine-modified electrodes (**Table 4.1**) [101,102,176]. Γ values that fall within the 10^{-10}–10^{-11} mol/cm^2 range are often ascribed to Pcs assuming a monolayer on the electrode surface where the Pc molecules are in a flat position whilst those that are higher are associated with electrodes derived from polymeric materials [176-178]. Such values were recorded when the area used was the geometric area of the electrode (0.071 cm^2) instead of that derived from the Cottrell equation (**Table 4.1**). In the context of the subsequent discussions however, the effective surface coverage involving the Cottrell equation was chosen.

The electrodes in **Table 4.1** all seem to possess a high surface coverage with exponentials of either 10^{-7} or 10^{-8} (with the exception of **GCE-5A** where the exponential is 10^{-6} which is higher). These results were attributed to electrode surfaces in which the film on the electrode surface is not a monolayer but rather a multi-layered film [178,179]. One reason that may account for this multi-layered film is the presence of a solvent layer on the electrode surface following the drying process. In comparing the Pcs alone, **GCE-9A** and **GCE-12A** to their corresponding conjugates, **GCE-9πNGQDs**, **GCE-12πNGQDs** and **GCE-12@NGQDs**, respectively, a lower surface coverage was observed for electrodes derived from the conjugates which may imply that the inclusion of NGQDs favours the formation of monolayers rather than multi-layers when adsorbed onto a glassy carbon electrode surface (**Table 4.1**). These observations however, are comparable to other electrode surfaces in which carbon-based nanomaterials have been coupled with Pcs [178]. The surface coverage was not determined for **GCE-4A**, **GCE-8C**, **GCE-10C** and **GCE-11A** as these electrodes did not produce any redox signals in the buffer.

4.4 Confirmation of triazole ring formation

Confirmation of the formation of the triazole ring through clicking was obtained through X-ray photoelectron spectroscopy (XPS). The spectra in **Fig. 4.7** are those of the deconvoluted C 1s (**Figs. 4.7A** and **4.7C**) and N 1s (**Figs. 4.7B** and **4.7D**) high resolution scans for complex **10** on its own and after clicking onto the glassy carbon plate. Looking at complex **10** on its own, deconvolution of the C 1s spectrum yielded two bands while the N 1s spectrum produced four (**Figs. 4.7A** and **4.7B**). The C 1s band that registered its maximum at 281.7 eV was assigned to sp^2-hybridized carbon atoms (sp^2 C) whilst that which displayed its maximum at 282.6 eV was attributed to sp^3-hybridized carbon atom (sp^3 C) (**Fig. 4.7A**, **Table 4.2**). While it is often the norm to assign sp^3 C to a higher binding energy than sp^2 C, these assignments are tentative as it is possible for it to be the other way around due to the type of material(s) presented [180].

The N 1s spectrum was deconvoluted to four peaks with maximum intensity at the following binding energies: 395.6 eV, 396.5 eV, 397.3 eV and 398.9 eV. The two bands with maximum binding energies at 396.5 eV and 397.3 eV were assigned to the nitrogen atoms bound directly to the metal ion (N_α, 397.3 eV) and the nitrogen atoms next to those bound to the metal centre (N_β, 396.5 eV). The maximum intensity for the amide nitrogen from the paracetamol substituent was observed at a binding energy of 398.9 eV, a slight deviation from the norm where amide bonds often register maximum binding energies between 399.6 and 399.9 eV or more [181].

Table 4.2: Fitting parameters for the C 1s and N 1s XPS spectra for complex **10** presented in **Fig. 4.7**.

Description[a]	**Fitting peaks**	**Bonds**	**Peak binding energy (eV)**
C 1s – (10)	C 1s	C=C/C=O/C=N	281.7
	C 1s	C-C/C-H	282.6
N 1s – (10)	N 1s	Satellite	395.6
	N 1s	N_β	396.5
	N 1s	N_α	397.3
	N 1s	N-(C=O)	398.9
C 1s – (10 Clicked)	C 1s	C=C/C=O/C=N	282.2
	C 1s	C-C/C-H	282.6
	C 1s	C=C-H	283.2
	C 1s	C-N	283.7
N 1s – (10 Clicked)	N 1s	N_β	394.7
	N 1s	N_α	397.2
	N 1s	N-(C=O)	399.9
	N 1s	N=N	401.8
	N 1s	N-N-C (R_3N)	405.3

a – Complex numbers in brackets.

The band that reached its peak maximum at a lower binding energy (395.6 eV), was attributed to a satellite shake-up which is the result of an electron which has been ejected from the core of the atom interacting with an electron in the valence band. Consequently, due to this interaction, the electron in the valence band is “shaken up” (excited) and the energy of the core electron is reduced, and a satellite band is observed at a slightly lower binding energy than where the core electron would have appeared (**Fig. 4.7B**, **Table 4.2**) [182].

With respect to the azide-bearing moiety grafted onto the carbon plate, three distinct bands were observed upon deconvolution. Based on a study involving a ferrocene-bearing azide [183], the assignments were made as follows: the inner nitrogen was assigned to the peak at the lowest binding energy (399.3 eV), the central nitrogen was assigned to that which registers its maximum at 400.9 eV and the outer nitrogen, assigned to the peak at 403.0 eV (**Fig. 4.7E**). Consequently, similar to Fortgang and colleagues, the disappearance of the central nitrogen in $-N=\mathbf{N}^{+}=N^{-}$ was used to confirm whether the cycloaddition reaction had taken place or not [183].

In **Fig. 4.7C**, the general intensity of the deconvoluted spectra exceeds that of complex **10** alone as seen in **Fig. 4.7A** (because the Pc is clicked onto a carbon plate). In addition to an increment in the intensity, the deconvolution of the C 1s region of the clicked carbon plate (complex **10** as an example) yielded four peaks with maximum intensities at 282.2 eV, 282.6 eV, 283.2 eV and 283.7 eV. The first two appearing at 282.2 eV and 282.6 were assigned to the sp^2 C and sp^3 C from the complex whilst the last two, with the higher binding energies, were ascribed to the carbon atoms that form part of the triazole ring (**Table 4.2**).

The N 1s spectra for the clicked complex **10**, in **Fig. 4.7D**, was deconvoluted to five peaks instead of four for the Pc alone. An important note to make is that upon clicking onto the carbon plate, the Pc complex assumes a change in the chemical environment resulting in a change in the chemical states and consequently, affecting the positions at which the peak binding energies are observed [184]. The deconvolution of the N 1s region in **Fig. 4.7D** was marked by the loss of the satellite where the first two peaks with their maxima at 394.7 eV and 397.2 eV, were ascribed to the beta and alpha nitrogen atoms. Two additional bands were observed with maximum intensities at 401.8 eV and 405.3 eV, these were attributed to the triazole ring (hence confirming that the click reaction was successful) with the peak appearing at 401.8 eV assigned to the azo-group (N=N) whilst that appearing at a higher binding energy, 405.3 eV, was assigned to the tertiary amine group (R_3N) (**Fig. 4.7D**, **Table 4.2**).

In comparing the grafted carbon plate with the clicked sample, a shift towards higher binding energies is observed for the latter with the peak associated with the outer nitrogen (403.0 eV) appearing to have completely collapsed as it assumes its new position within the five-membered triazole ring. Furthermore, the intensity of the peaks observed on the carbon plate (**Fig. 4.7E**) are generally higher than those of the clicked plate (**Fig. 4.7D**), further supporting the notion that the Pc has been successfully anchored onto the surface.

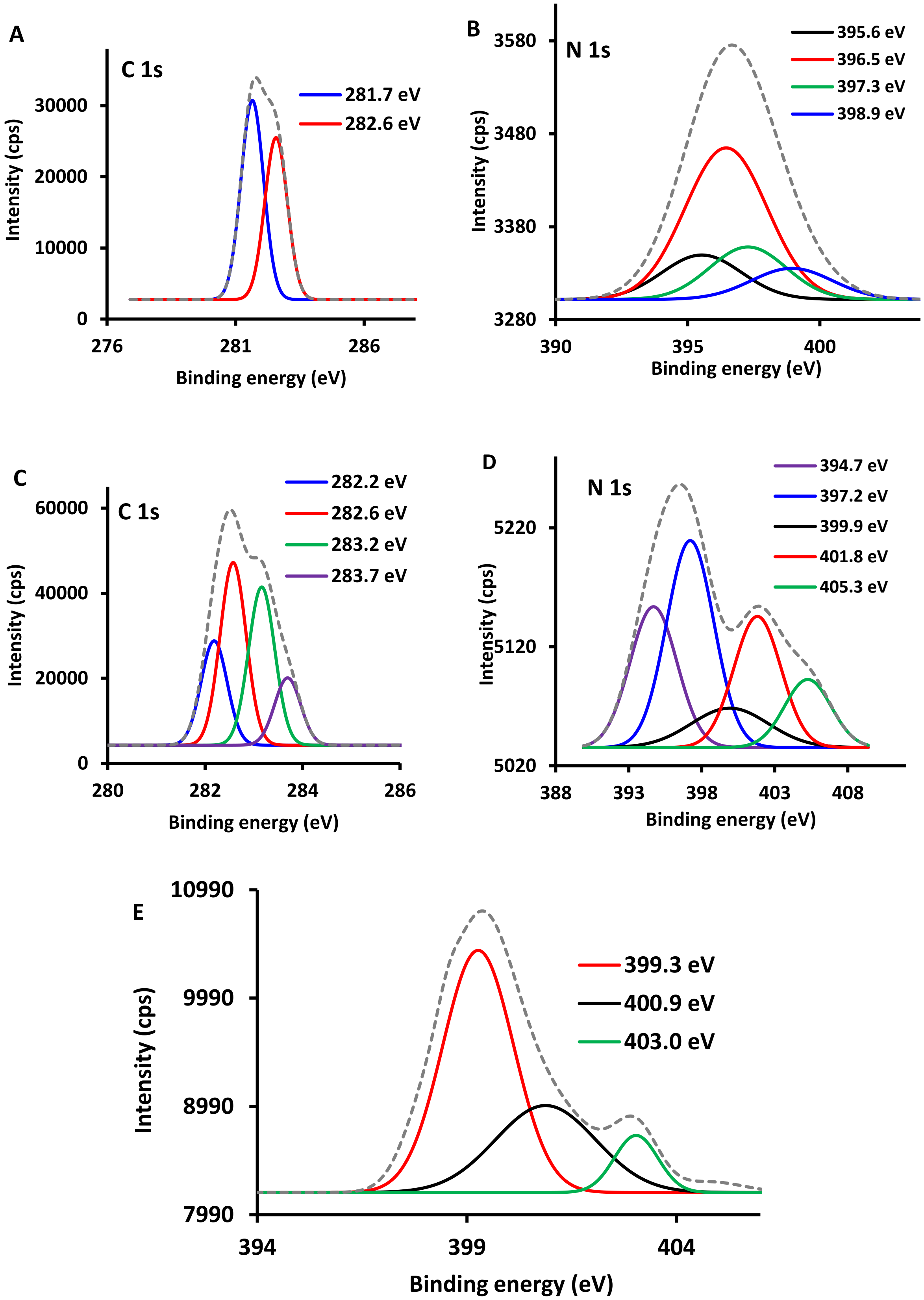

Fig. 4.7: Deconvoluted high resolution C 1s and N 1s spectra of complex **10** before (**A** and **B**) and after (**C** and **D**) it has been clicked onto a glassy carbon plate, and the deconvoluted N 1s XPS spectrum of a grafted carbon plate (**E**).

4.5 Summary of chapter

This chapter is based on the characterisation of the modified electrode surfaces using the appropriate/relevant electrochemical techniques. What is evident from the results, despite the redox probe being the same in all the electrochemical techniques, is that there is a lack of uniformity in that trends are observed in clusters (i.e. the type of substituents employed, the central metal, method of electrode modification, presence/absence of nanomaterials), more so for the cyclic voltammetric and EIS data as they produce quantitative results. Nonetheless, all the techniques applied demonstrated that the electrode surface was indeed altered with the XPS being used as a complementary technique where electrode modification was posited to have taken place through the formation of a covalent bond in the form of a triazole ring.

CHAPTER 5

SENSING

Detailed discussions on the electrocatalysis of hydrazine and nitrite are provided in this chapter.

5. Electrochemical sensing

In assessing the electrocatalytic activity of the designed probes, voltammetric and amperometric techniques were applied. The electrochemical behaviour of the electrocatalysts was studied through observing multiple indicators including the peak oxidation potential (E_p), peak catalytic current (I_p) as well as the limits of detection (LoD). Other variables such as the Tafel slopes and catalytic rates were also determined to aid in understanding the interactions between the modified electrodes and the analytes.

5.1 Electro-oxidation of hydrazine

5.1.1 Voltammetric analyses

Cyclic voltammetry was used in identifying the general responsiveness of the probes towards hydrazine. Ideally, a good electrocatalyst is marked by its ability to reduce the oxidation potential as well as enhance the peak catalytic current [9]. The cyclic voltammograms of some of the probes studied are shown in **Fig. 5.1** with distinct differences in the general E_p positions and I_p intensities being observable (**bare GCE** shown in **Fig. A17** eliciting no response). From **Fig. 5.1** alone, it is evident that the electrodes modified with the pentadecylphenoxy containing substituents elicit a better response in terms of the peak current in comparison to electrodes that possess the *tert*-butyl bearing electrocatalysts. In terms of the E_p however, the opposite was observed.

From the summary provided in **Table 5.1**, with respect to the E_p, the following deductions regarding the voltammetric response to hydrazine were made:

- The probes fabricated from the *tert*-butyl complexes elicited the better response as they had the lower oxidation potentials (**GCE-6A** and **GCE-7A**).

  - The asymmetric complex in **GCE-6A** produced a lower E_p value than its symmetric counterpart in **GCE-7A**, demonstrating the advantages of asymmetry.
  - The dip observed in the reverse cycles for **GCE-6A** and **GCE-7A** in **Fig. 5.1**, as described in previous reports, is due to the regeneration of the catalyst [96].
- Regarding the pentadecylphenoxy-based probes, **GCE-2A** and **GCE-3A** yielded the most favourable results with E_p values of 701 mV and 709 mV, respectively.
  - All asymmetric catalysts with the exception of **GCE-1A** performed better than the probe derived from the symmetric complex, complex **5** (**GCE-5A**).
- The overall order in terms of the most favourable to the lease favourable for the E_p values recorded in the electro-oxidation of hydrazine are as follows:

GCE-6A > **GCE-7A** > **GCE-2A** > **GCE-3A** > **GCE-4A** > **GCE-5A** > **GCE-1A**

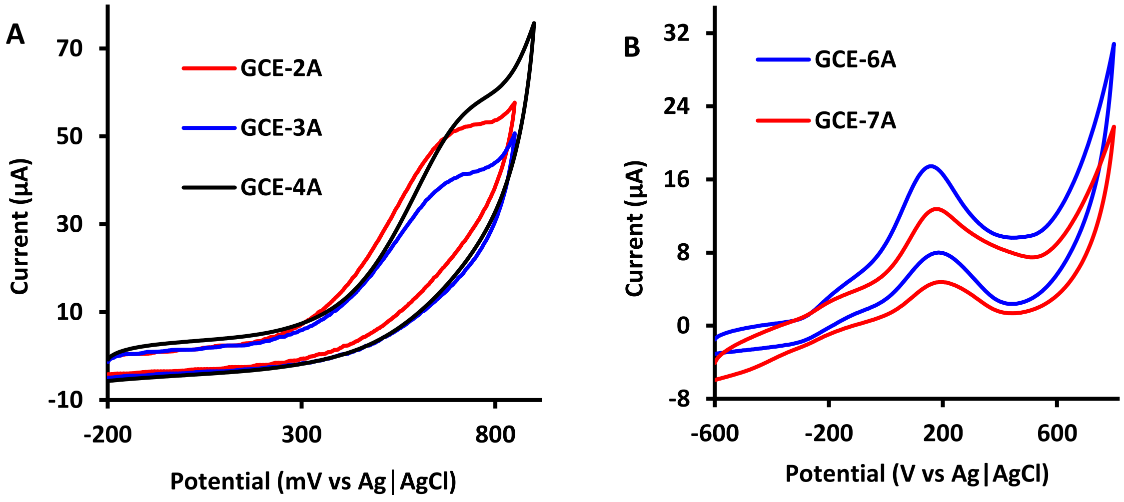

Fig. 5.1: Cyclic voltammograms of some the probes investigated in the electro-oxidation of hydrazine where (**A**) are the voltammetric responses in the presence of 1.0 mM of hydrazine and (**B**) presents the electrochemical response in the presence of 2.0 mM of hydrazine. All in 0.1 M NaOH at a scan rate of 100 mV/s.

With respect to the peak current (I_p), the observations were made as such:

- All pentadecylphenoxy-based probes produced a greater I_p value than the *tert*-butyl-based probes.
    - A greater concentration of hydrazine was required to produce a measurable signal from **GCE-6A** and **GCE-7A**.
- All the asymmetric complexes performed better than their symmetric analogues.
- In ranking the probes based on the I_p values recorded, the electrodes were ranked as follows:

GCE-4A > **GCE-2A** > **GCE-3A** > **GCE-1A** > **GCE-5A** > **GCE-6A** > **GCE-7A**

The voltammetric results observed suggest that asymmetric Pcs, in the general sense, are better than their symmetric derivatives however, this is not applicable to all asymmetric Pcs as substituents do not always complement each other or function in a cohesive manner. The electrodes derived from the *tert*-butyl Pcs, **GCE-6A** and **GCE-7A**, produced the lower oxidation potentials which were attributed largely to the direct bond between the Pc skeleton and the substituents (C-C). The direct bond is posited to have enabled the substituents' electron-donating nature to come into full effect resulting in an improvement in which the Pc is oxidized and consequently, lowering the potential at which hydrazine is oxidized [185].

Looking at the background correct current (I_p) and how it relates to the surface coverage (Γ), it is evident that the I_p is influenced by other factors not limited to the surface coverage as the Γ values in **Table 5.1** are fairly similar for the probes investigated. Although there are minimal differences in the Γ values, the pentadecylphenoxy-based electrodes (**GCE-1A** – **GCE-5A**) possess higher I_p values than those derived from the *tert*-butyl complexes, **GCE-6A** and **GCE-7A** (**Table 5.1**). These findings suggest that the I_p is largely dependent on the substituents more than it is on the surface coverage (**Tables 4.1** and **5.1**). This is supported by a previous study involving an unsubstituted CoPc with a surface coverage of 5 × 10^{-11} mol/cm^2 eliciting a similar I_p to **GCE-6A** and **GCE-7A** (where the scale on the *y*-axis was presented in mA and the concentration measured was 2.6 mM) (**Fig. 5.1A**) [186]. Another reason that may account for the differences in the I_p value as far as the substituents are concerned is that **GCE-1A** – **GCE-5A** are derived from phenoxy-based substituent which provides additional π bonds which are known to be more reactive than sigma bonds which are the type that dominate the *tert*-butyl substituent [187]. Overall, it appears that while the *tert*-butyl substituent is useful in lowering the E_p, it serves primarily as an agent of enhancing solubility rather than driving electron-transferring processes (hence the low I_p values registered) [74].

Table 5.1: A summary of the voltammetric data obtained in the electrocatalysis of hydrazine in 0.1 M NaOH, in the presence of 1.0 mM of hydrazine.

Probe	***Γ* (mol/cm^2)**	**E_p (mV) vs Ag|AgCl**	**Background corrected current, I_p (µA)**	**Tafel slope (mV decade^{-1})^a**
GCE-1A	2.72 × 10^{-7}	983	17.4	129 (331)
GCE-2A	2.22 × 10^{-7}	701	43.0	221 (268)
GCE-3A	1.65 × 10^{-7}	709	32.7	168 (422)
GCE-4A	c	734	47.9	265 (294)
GCE-5A	3.65 × 10^{-6}	980	10.1	350 (91.9)
GCE-6A^b	2.92 × 10^{-7}	139	6.16	135
GCE-7A^b	3.72 × 10^{-7}	167	5.51	114

a – Values in brackets obtained from **Eq. 5.1**; b – I_p recorded in 2.0 mM of hydrazine; c – no peak/signal in the buffer.

5.1.1.1 Kinetic studies on hydrazine-electrode interactions

Electrode kinetics is the term used to describe the rate at which an electron moves between the electrode and the species in solution [188]. By studying the interactions between the electrode surface and analyte, deductions regarding the mode of transport to and from the electrode can be made. Furthermore, an extensive analysis on the kinetics may provide insights into the possible mechanisms that are taking place between the analyte and electrode surface [189].

The reaction mechanisms used to describe how an analyte interacts with the electrode surface is described as diffusion or adsorption-controlled amongst others [190]. Diffusion-controlled processes involve the transportation of molecules through a medium (before making contact with the interface) where the reactants are separated from the products [190]. Adsorption-based processes on the other hand are those that involve the direct transportation from the bulk phase to the interface [190]. In determining which of the two processes was involved regarding the electro-oxidation of hydrazine, cyclic voltammetric scans were performed in which the concentration of hydrazine was kept the same with the scan rates being varied (**GCE-3A** provided as an example in **Fig. 5.2A**). From the data obtained from the voltammograms in **Fig. 5.2A**, plots of log I_p vs log v were drawn. Using the slope from the plots, the electrode-analyte processes where established. For diffusion-controlled processes, a slope of 0.5 is obtained whilst a slope of 1 or close to 1 is associated with adsorption-based activity [191-193]. The electrodes presented in **Table 5.1** (**GCE-1A** – **GCE-7A**) all produced a slope of 0.5 suggesting diffusion-based interactions between the electrodes and the analyte, hydrazine.

One of the ways in which the reaction mechanism can be determined is through a Tafel analysis where the Tafel slope is determined [194]. Tafel slope values that are synonymous with a single electron transfer process range from 60 to 120 mV/decade [195]. A Tafel slope that exceeds 120 mV/decade is reported to possess no kinetic meaning and may be the result of adsorption of either the products and/or intermediates onto the modified electrode surface [173,196,197]. Using the same approach as Mohammadizadeh and colleagues by plotting the log of the onset current against the potential in the region where the onset potential is obesrved, the Tafel slopes were determined with the values presented in **Table 5.1** (**Fig. 5.3**) [198].

A secondary approach to determining the Tafel slopes was explored using **Fig. 5.2C** and the following equation, **Eq. 5.1** [199]:

$$\mathrm{E_p} = \frac{b}{2}\log v + constant \qquad (\mathbf{5.1})$$

Where $\mathrm{E_p}$ is equated to the slope in **Fig. 5.2C** and b is the Tafel slope. In comparing the Tafel slopes from the two methods for **GCE-1A** – **GCE-5A**, the differences were vast which may be attributed to the regions from which the slopes are derived. The first method using the onset potential involves the lower overpotentials whilst the latter is dominated by the higher overpotentials. This observation where an electrode produces different Tafel slopes based on the location of the overpotential (low versus high) has been identified in iron electrodes [200]. Another reason that may account for the differences between the two methods is the surface coverage, where it is suggested that an inconsistent surface coverage may produce variations in the Tafel slope values [201]. Taking into consideration that the electrode kinetics are better evaluated at lower scan rates, the first method entailing the use of the onset potential was used as the primary method of determining the Tafel slopes for all the electrodes.

Using this method, the Tafel slopes determined ranged from 114 to 350 mV/decade with **GCE-7A** falling within the 120 mV/decade window for a single-electron process (**Table 5.1**). **GCE-1A** and **GCE-6A** also produced values close to the desired range with Tafel slopes of 129 and 135, respectively (**Table 5.1**). The other electrodes produced Tafel slopes so high that they are incomparable to those that have been previously reported for CoPcs used in the electrocatalysis of hydrazine [98]. Nonetheless, with theoretical calculations indicating that the electrochemical reaction between CoPcs and hydrazine is largely driven by the central metal, cobalt in this case, the mechanism in which the electrooxidation of hydrazine proceeds, for **GCE-1A** until **GCE-5A**, was described as follows (**Eqs. 5.2**-**5.4**) [119]:

$$[\mathrm{CoPc(I)}]^- \rightarrow \mathrm{Co(II)Pc} + e^- \quad \mathbf{(5.2)}$$

$$\mathrm{Co(II)Pc} + N_2H_4 + OH^- \rightarrow [\mathrm{Co(I)Pc{-}N_2H_3}]^- + H_2O \quad \mathbf{(5.3)}$$

$$[\mathrm{Co(I)Pc{-}N_2H_3}]^- \rightarrow [\mathrm{Co(I)Pc}]^- + {}^{\bullet}N_2H_3 \quad \mathbf{(5.4)}$$

$${}^{\bullet}N_2H_3 + 3OH^- \rightarrow N_2 + 3e^- + 3H_2O \quad \mathbf{(5.5)}$$

where the second step involves coordination of the hydrazine molecule to the cobalt atom (**Eq. 5.3**), the coordination then results in a reduction of the cobalt metal from Co^{2+} to Co^+, followed by a disproportionation of the CoPc-hydrazine complex to produce a hydrazine radical (**Eq. 5.4**). The final step involves the hydrazine radical reacting with the hydroxide ions in solution to produce more stable molecules, nitrogen gas and water (**Eq. 5.5**).

Based on a theoretical study by Geraldo and colleagues, a second mechanism shown by **Eqs. 5.6-5.10** was proposed for **GCE-6A** and **GCE-7A** [202]:

$$N_2H_4 + \mathrm{Co(II)Pc} \rightleftharpoons [\mathrm{Co(I)Pc}^- \text{-} (N_2H_4)^+] \quad \mathbf{(5.6)}$$

$$[\mathrm{Co(I)Pc}^- \text{-} (N_2H_4)^+] + OH^- \rightarrow \mathrm{Co(II)Pc} + {}^{\bullet}N_2H_3 + e^- + H_2O\ (\mathit{rds}) \quad \mathbf{(5.7)}$$

$$^{\bullet}N_2H_3 \rightarrow {}^{\bullet}N_2H_2 + e^- + H^+ \quad (\mathbf{5.8})$$

$$^{\bullet}N_2H_2 \rightarrow {}^{\bullet}N_2H + e^- + H^+ \quad (\mathbf{5.9})$$

$$^{\bullet}N_2H \rightarrow N_2 + e^- + H^+ \quad (\mathbf{5.10})$$

(*rds* = rate determining step)

where the first step involves coordination of the hydrazine molecule to the cobalt atom (**Eq. 5.6**), the coordination then results in a reduction of the cobalt metal from Co^{2+} to Co^{+}, followed by a disproportionation of the CoPc-hydrazine complex to produce a hydrazine radical (**Eq. 5.7**). The $^{\bullet}N_2H_3$ radical then reacts in successive steps losing one electron and one proton at a time through steps (**5.8**)–(**5.10**) resulting in the making of nitrogen as the final product of the reaction.

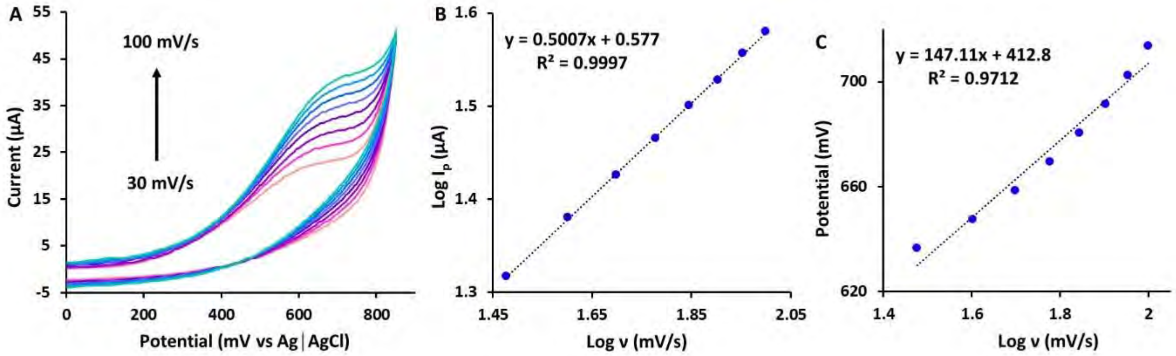

Fig. 5.2: (A) is an illustration of the cyclic voltammograms of **GCE-3A** at various scan rates (**B**) is the plot of the log I_p against the log v and (**C**) is the plot of potential vs log *v*. All in the presence of 1.0 mM of hydrazine in 0.1 M NaOH.

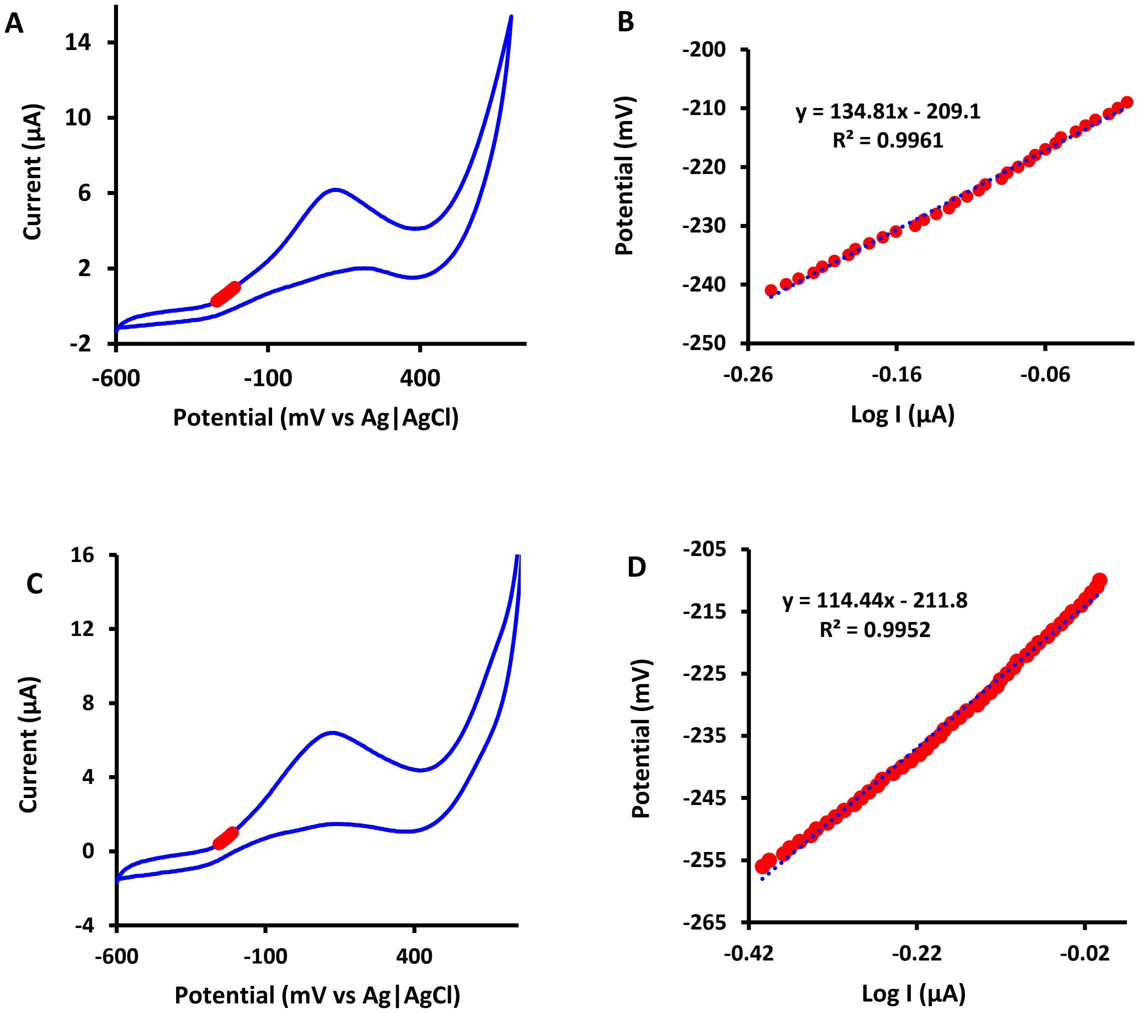

Fig. 5.3: Cyclic voltammograms recorded at 10 mV/s for **GCE-6A** (**A**) and **GCE-7A** (**C**) in 2.0 mM hydrazine, in 0.1 M NaOH and the corresponding Tafel plots (**B** and **D**). The points in pink/red are the points used to produce the Tafel plot (**A** and **C**).

5.1.1.2 Stability studies

In determining which of the probes provide the most stable electrochemical response in the presence of the analyte, multiple cyclic voltammetric scans were carried out at a fixed scan rate and concentration of hydrazine. The overall observation made with respect to the stability of the probes is that the asymmetrical molecules render modified electrodes more stable than their symmetrical counterpart, **GCE-5A** (**GCE-2A** and **GCE-5A** provided as examples in **Figs. 5.4A** and **5.4B**). Of the asymmetric probes studied, **GCE-1A**, **GCE-2A**, **GCE-3A** and **GCE-4A**, none presented any instability as the percentage difference between the first and twentieth scan did not exceed 3 % (**Fig. 5.4A**, **GCE-2A** as an example).

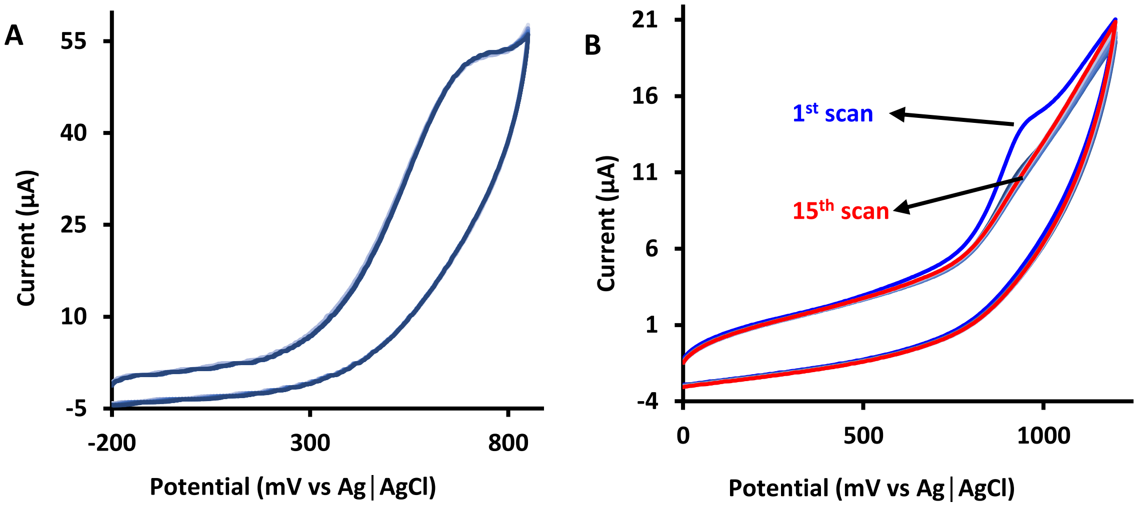

Fig. 5.4: Stability scans for **GCE-2A** (**A**) and **GCE-5A** (**B**) at 100 mV/s in the presence of 1.0 mM of hydrazine in 0.1 M NaOH.

Following 20 consecutive scans, the oxidation peak in **GCE-2A** retains its original position in terms of the oxidation potential and the peak catalytic current while the observation made for **GCE-5A** is a gradual disappearance of the oxidation peak as the number of scans is increased (**Figs. 5.4A** and **5.4B**). The probes fashioned from the *tert*-butyl containing complexes, **GCE-6A** and **GCE-7A**, were also found to be unstable with a noticeable decline in the I_p as the number of voltammetric scans increased. A decline of approximately 39 % was recorded for **GCE-6A** while **GCE-7A**’s I_p decreased by almost 25 % after twenty consecutive scans. And while some of the probes studied demonstrated great stability, further studies regarding identifying potential interferants were not performed due to the absence well-defined cyclic voltammograms (**GCE-6A** and **GCE-7A** possess better profiles compared to **GCE-2A**, **GCE-3A** and **GCE-4A**, **Fig. 5.1**).

5.1.2 Chronoamperometric analyses

5.1.2.1 Limits of detection

The chronoamperometric changes in response to increments in concentration of the analyte are shown in **Fig. 5.5A** (**GCE-2A** as an example) where the inset illustrates the linear relationship between the concentration and the current obtained from the chronoamperograms (**Fig. 5.5A**). The slope in the inset in **Fig. 5.5A**, which is also considered the sensitivity, is derived from a response versus concentration plot where the current at a specific time (1.02 s in this case) is plotted against the changes in the concentration of hydrazine. Using the slope from the inset in conjunction with the 3δ/s equation (where δ is standard deviation of the blank and s is the slope of the calibration curve in **Fig. 5.5**'s inset), the limits of detection (LoD) were determined for all the probes studied with the results presented in **Table 5.2**.

Table 5.2: Electrochemical summary of the chronoamperometric results obtained in the electrochemical sensing of hydrazine.

Probe	Sensitivity (μA/mM)	LoD (μM)	*k* ($M^{-1}s^{-1}$)
GCE-1A	0.86 (± 0.1)	65.8 (± 7.9)	6.66
GCE-2A	60.6 (± 0.4)	26.1 (± 0.2)	3.25
GCE-3A	60.9 (± 0.5)	5.10 (± 0.04)	5.81×10^1
GCE-4A	10.7 (± 0.2)	10.2 (± 0.2)	5.43×10^1
GCE-5A	3.80 (± 0.3)	14.9 (± 1.1)	6.00×10^2
GCE-6A	5.52 (± 0.3)	14.4 (± 0.7)	1.25×10^2
GCE-7A	3.00 (± 0.3)	54.1 (± 5.1)	1.37×10^2

*Values in brackets represent average standard deviations where *n=3*.

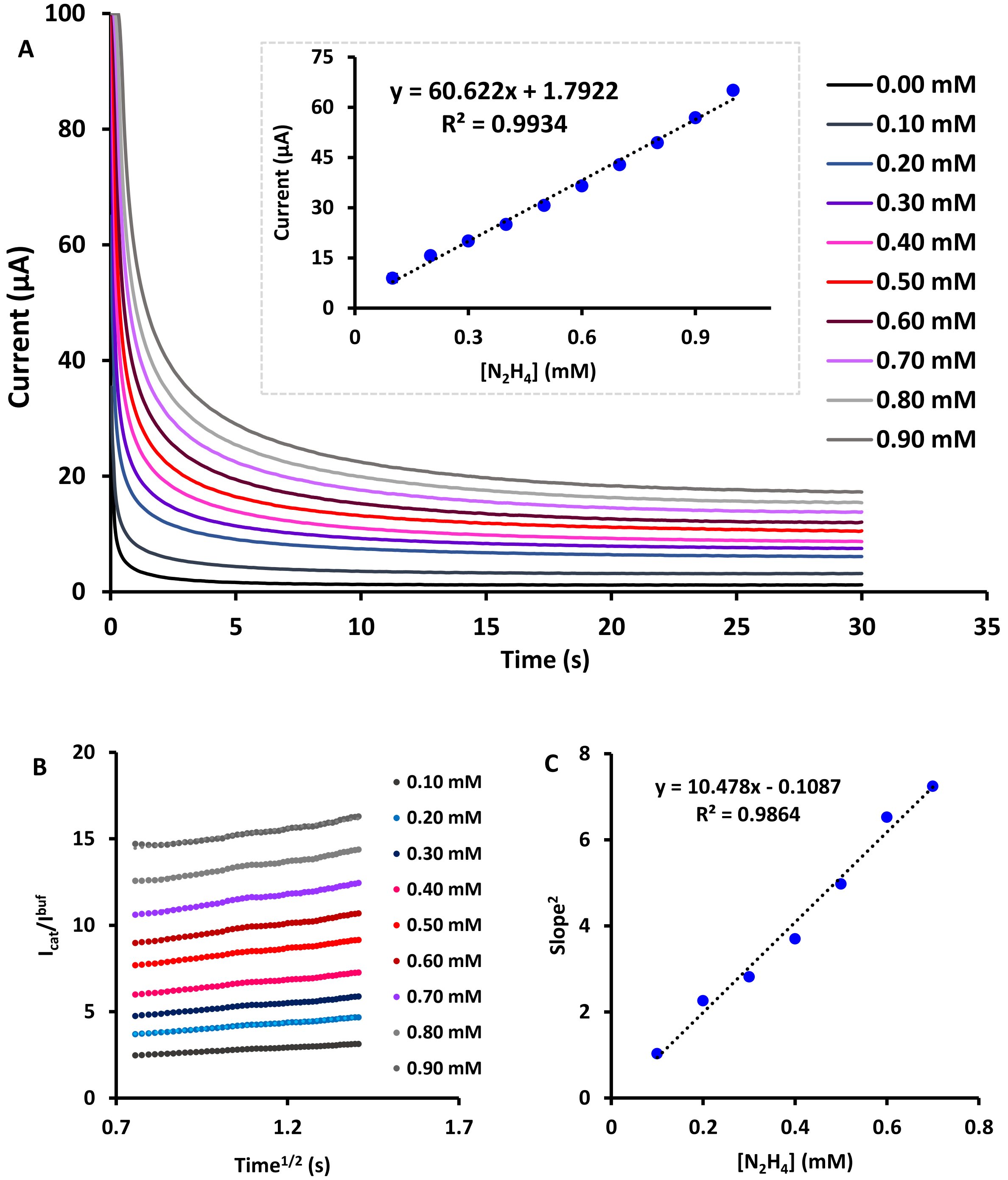

Fig. 5.5: (**A**) Chronoamperograms for **GCE-2A** in different concentrations of hydrazine (in 0.10 M NaOH). Inset: calibration curve for **GCE-2A**. Error bars not visible because all standard deviations are 0.01> (*n = 3*). Plots of the I_{cat}/I_{buf} versus the square root of time (**B**) and a plot of the slope^2 against the concentration of hydrazine (**C**) (**GCE-2A** used as an example).

A great deal of variation was observed in the sensitives with the lowest being 0.86 µA/mM for **GCE-1A** and the highest being 60.9 µA/mM for **GCE-3A** (**Table 5.2**). In terms of the substituents, it is evident that the pentadecylphenoxy-based electrodes generally possess better sensitivities than the *tert*-butyl-based electrodes with a few exceptions (**Table 5.2**). Regarding the symmetry, the electrodes based on the asymmetric Pcs yielded better results than their symmetric counterparts with **GCE-1A** being the exception suggesting that in these particular conditions, the pairing of substituents in the overall construction of the A_3B CoPc is not ideal (**Table 5.2**).

The best performance was registered for **GCE-3A** with an LoD value of 5.10 µM (**Table 5.2**). This observation corresponds with what is often the norm in electrocatalysis where a high sensitivity is accompanied by a low limit of detection [98]. **GCE-4A** was found to be an exception with a value of 10.2 µM accompanied by a low sensitivity of 10.7 µA/mM despite **GCE-2A** presenting a better sensitivity of 60.6 µm/mM (LoD of 26.1 µM) (**Table 5.2**). The other asymmetrical complexes (**GCE-1A** and **GCE-2A**) fare poorly in comparison to the symmetrical pentadecylphenoxy-substituted CoPc derivative, **GCE-5A**. Regarding the *tert*-butyl based complexes, the asymmetric CoPc in **GCE-6A** produced a better LoD value than its symmetric derivative in **GCE-7A**. In the general sense, the CoPcs that bore the 15-carbon chain as the dominant substituent were better than the short, branched alkyl-containing Pcs (**Table 5.2**).

Although high LoD values were obtained for **GCE-1A**, **GCE-2A** and **GCE-7A**, the rest of the probes compare (and even better in some cases) very well with previous reports based on CoPc derivatives as electrocatalysts for hydrazine (**Table 5.3**) [108,203,204]. Furthermore, what is most impressive with these probes is that their results can be improved further through the addition of nanomaterials through covalent or non-covalent linking as in this work, they are studied as single entities.

Table 5.3: Limits of detection for hydrazine in comparison with literature values for CoPc derivatives.

Probe/electrode	LoD (µM)	Ref.
Co tetrahexynl phthalocyanine	6.09	[108]
CoPc – screen-printed electrodes	6.21	[203]
CoPc – carbon paste electrode	73.5	[204]
GCE-3A	5.10	This work
GCE-4A	10.2	This work

5.1.2.2 Catalytic rates

The catalytic rates were calculated as previously reported in similar studies [98,205] where the ratio between the buffer and the buffer containing the analyte was plotted against the square root of time (**Fig. 5.5B**). These yielded straight lines of different slopes which were squared and plotted against the corresponding concentration (**Fig. 5.5C**). The catalytic rate constants were determined through correlating the data obtained with the following equation, **Eq. 5.11** [206]:

$$\frac{I_{cat}}{I_{buf}} = \gamma^{1/2}\,\pi^{1/2} = \pi^{1/2}\,(kCt)^{1/2} \tag{5.11}$$

where I_{cat} and I_{buf} represents the current(s) in the presence and absence of hydrazine, C the concentration of hydrazine, t as the time that has elapsed in seconds and *k*, the catalytic rate. With the exception of **GCE-7A**, which has both a high LoD and *k* value, the general observation that can be made is that the probes that exhibit low LoDs are accompanied by moderately high catalytic rates. **GCE-5A** bears the highest catalytic rate which may be due to the higher surface area it possesses, 3.65 × 10^{-6} mol/cm^2 (**Table 5.1**). Previous reports have noted the influence of surface area on the rate of a reaction in heterogeneous catalysis [207].

5.1.3 Computational chemistry

Computational chemistry methods are often used to better understand experimental results (by identifying the reactive sites) [119,208]. Due to their simplistic structures, a brief exploration based on complexes **6** and **7** was undertaken in an attempt to assess whether computational methods support experimental observations or if they can be used to predict the reactivity of materials, **GCE-6A** and **GCE-7A** in this case.

Geometry optimization for complexes **6** and **7** was performed at the B3LYP level with the 6-31G(d) basis set in the presence and absence of a hydrazine axial ligand (**Fig. 5.6**). In addition to determining the gap between the highest occupied molecular orbital (HOMO) and the lowest unoccupied molecular orbital (LUMO) (E_{gap}), the global reactivity descriptors were calculated. The descriptors, namely: chemical softness (S), hardness (η), electrochemical potential (μ), electrophilicity (ω) and the electronegativity (χ) were determined using the **Eqs. 5.12**-**5.17** [208]:

$$E_{gap} = E_{LUMO} - E_{HOMO} \qquad (\mathbf{5.12})$$

$$S = \eta/2 \qquad (\mathbf{5.13})$$

$$\eta = (E_{LUMO} - E_{HOMO})/2 \qquad (\mathbf{5.14})$$

$$\mu = -(E_{LUMO} - E_{HOMO})/2 \qquad (\mathbf{5.15})$$

$$\omega = \mu^2/2\eta \qquad (\mathbf{5.16})$$

$$\chi = -\mu \qquad (\mathbf{5.17})$$

The frontier orbitals, the HOMO and the LUMO are important in determining the stability and the reactivity of the molecule(s) [208]. Based on Michl's perimeter model [209], frontier π-

MOs arising from the HOMO and LUMO of a $C_{16}H_{16}^{2-}$ parent perimeter with M_L = ±4 and ±5 angular nodal properties, respectively, are referred to as the **a, s, -a** and **-s** molecular orbitals (MOs) in the MO energy diagram in **Fig. 5.7** depending on whether a nodal plane (**a**/**-a**) or significant MO coefficients (**s**/**-s**) are aligned with the *y*-axis. The **a**, **-a** and **-s** MOs were found to correspond to the HOMO, and the near degenerate LUMO and LUMO+1 of the electronic structures of **6** and **7**, while the **s** MO of phthalocyanines is markedly stabilized by having large MO coefficients on the aza nitrogens (**Fig. 5.7**) [68]. The SOMO (singly occupied molecular orbital (orbital with a single electron)) appeared to be localized primarily on the $3d_{z^2}$ orbital of the Co(II) ion (**Fig. 5.7**).

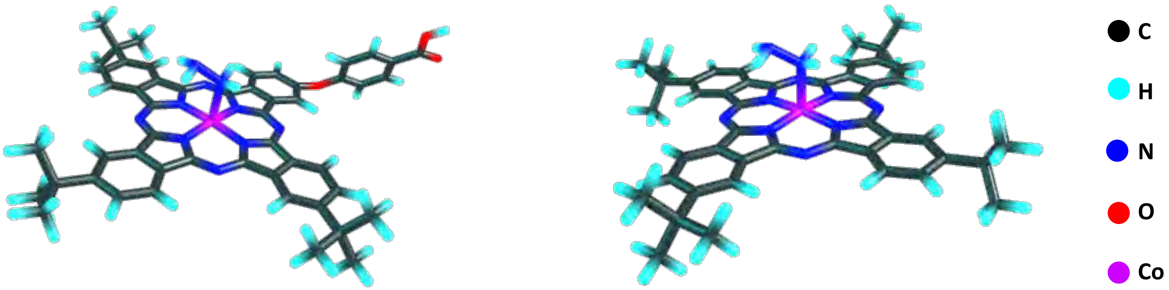

6 **7**

Fig. 5.6: Optimized structures of complexes **6** and **7** (with hydrazine as an axial ligand).

A HOMO energy of −4.89 eV was predicted for **6**, while the value for **7** was −4.76 eV (**Table 5.4**). Although the difference is small, **6** was predicted to be the more stable complex as anticipated based on the introduction of the electron-withdrawing carboxylic acid moiety. Since both the HOMO and LUMO of **6** and **7** are stabilized to a similar extent, with the HOMO−LUMO gap (E_{gap}) for both complexes being 2.22 eV (**Table 5.4**, **Fig. 5.7**) there were no significant differences in the Q-band energies as observed experimentally (**Table 3.1**).

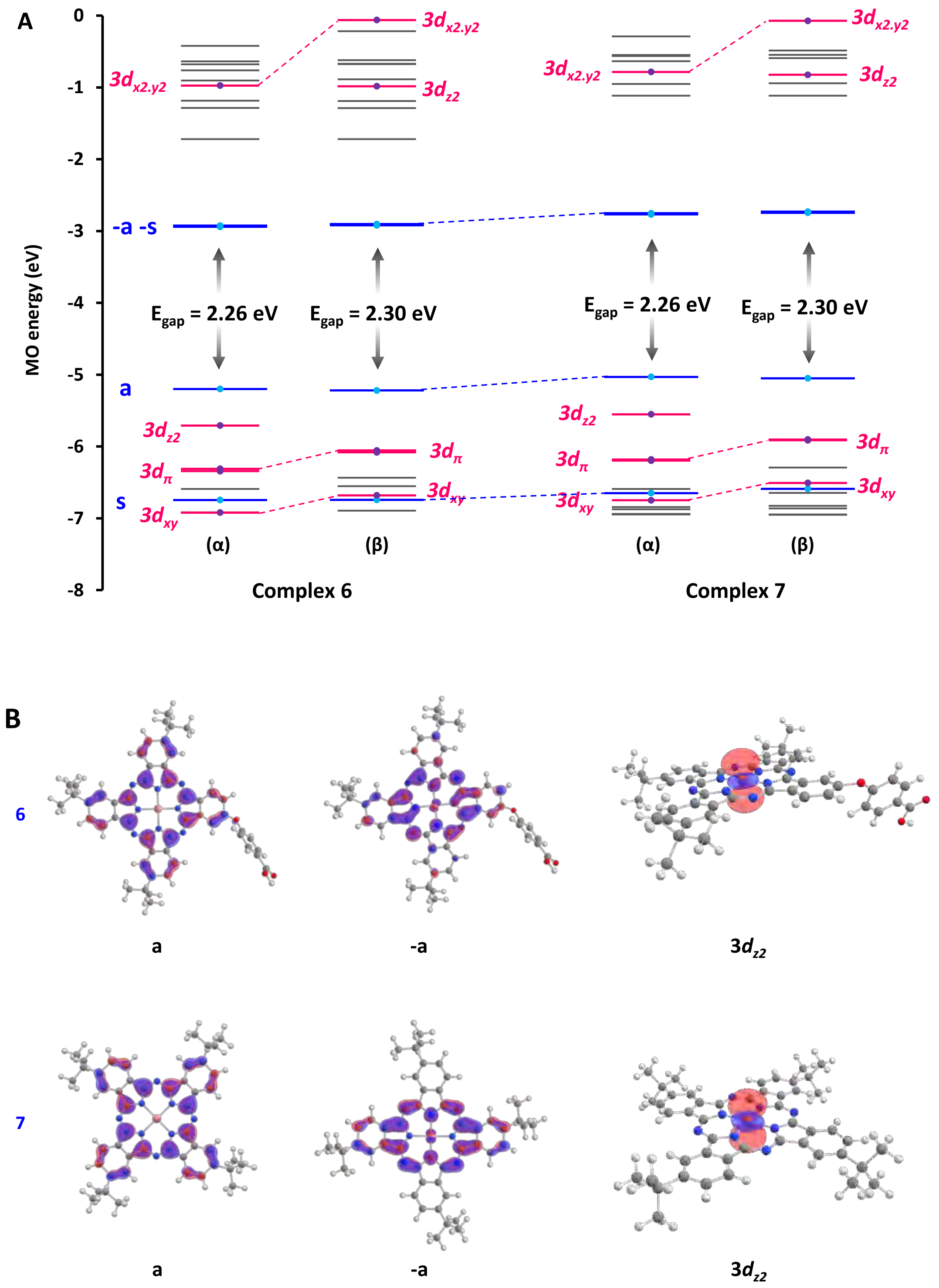

Fig. 5.7: MO energy diagram for complexes **6** and **7** showcasing the HOMO−LUMO gap (E_{gap}, with N_2H_4 as an axial ligand), the **a**, **s**, **-a** and **-s** MOs of Michl's perimeter model [209] and the MOs that are largely localized on the 3*d* atomic orbitals of the Co(II) ion, including the $3d_{z2}$ MO that is likely to be involved in the electrooxidation of hydrazine. The α and β symbols represent the spin orientation of the electrons, spin up or spin down (**A**). Angular nodal patterns of the **a** and **-a** MOs that are the HOMO and LUMO of the π-system, as well as the SOMO, which is localized on the $3d_{z2}$ orbital of the Co(II) ion (**B**).

Table 5.4: E_{HOMO}, E_{LUMO} and the global reactivity descriptors determined for the complexes (α spin orbital energies, in the absence of hydrazine as an axial ligand).

Parameters (eV)	Complex 6^a	Complex 7^a
E_{HOMO}	−4.89 (−5.12)	−4.76 (−5.03)
E_{LUMO}	−2.67 (−2.94)	−2.54 (−2.77)
E_{gap}	2.22 (2.26)	2.22 (2.26)
η	1.11 (1.13)	1.11 (1.13)
η_{DA}	(2.88)	(2.82)
S	0.56 (0.57)	0.56 (0.57)
μ	−3.78 (−4.07)	−3.65 (−3.90)
Ω	6.42 (7.33)	5.98 (6.72)
χ	3.78 (4.07)	3.65 (3.90)

a – Values in brackets are those of the indicators in the presence of hydrazine as an axial ligand.

Other electronic properties were used to determine the relative reactivities of the complexes (**Table 5.4**). The electrophilicity (ω) and the electronegativity (χ) values can be used as the primary indicators in this regard as the chemical softness (S) and hardness (η) produced equal values (**Table 5.4**). And with complex **6** displaying higher electrophilicity (ω) and electronegativity (χ) values than complex **7**, complex **6** was deemed to be the more reactive complex (**Table 5.4**).

The mechanism described in **Eqs. 5.6**-**5.10** is dominated by the cobalt centre which has often been reported to be the case in the electrocatalysis of hydrazine by CoPcs [119]. This implies that the oxidation of hydrazine is facilitated by the interaction with the SOMO which is largely localized on the $3d_{z^2}$ atomic orbital of the Co(II) ion (**Fig. 5.7B**). To further understand the reactivity of these macrocycles in response to the catalysis of hydrazine, further application of the DFT calculations were undertaken with hardness (η) being the most suitable concept to apply in this context. Molecular hardness is loosely described as a molecule’s ability to attract electrons and the higher the value, the greater the ability of that molecule to attract electrons. Due to the similarities in the structure, the values for hardness for both complexes are the same, 1.13 eV (**Table 5.4**). Moreover, these values are comparable to those reported for similar molecules [176,210].

With the hardness values being the same, to better gauge the reactivity of the complexes, the donor-acceptor hardness was determined using Koopman's approximation (**Eq. 5.18**) for determining the electronic coupling between the CoPc and hydrazine [176,211]:

$$\eta_{DA} = (E_{LUMO(A)} - E_{HOMO(D)}) / 2 \qquad (\mathbf{5.18})$$

Where $E_{LUMO(A)}$ represents the LUMO energy level of the acceptor molecule, $E_{HOMO(D)}$ represents the HOMO energy level of the donor and η_{DA} is the donor-acceptor molecular hardness.

The results in **Table 5.4** show that the donor-acceptor molecular hardness for **6** is slightly higher than that of **7**. From this observation, it is expected that there is an enhanced interaction between **6** and hydrazine which was seen to be the case (relative to the interaction between **7** and hydrazine). This is supported by a higher Ip being observed for **GCE-6A** in comparison to **GCE-7A** (**Table 5.1**, **Fig. 5.1B**). Furthermore, previous studies involving similar macrocycles have suggested that a large electronic coupling value (η_{DA}) promotes a shift of redox reactions to lower potentials. This is observed with complex **6** (**GCE-6A**), which has an η_{DA} value of 2.88 eV having a lower oxidation potential (for the oxidation of hydrazine) than the symmetric structure in **GCE-7A** (complex **7**), which has an η_{DA} value of 2.82 eV (**Table 5.4**) [212]. The general observation that was made upon incorporating hydrazine as an axial ligand was a minor increase in the energies of the global indicators, namely the electrophilicity (ω)

and electronegativity (χ) **Fig. 5.8**). Complexes **6** and **7** were predicted to have the same E_{gap} values both in the presence and absence of hydrazine (**Table 5.4**).

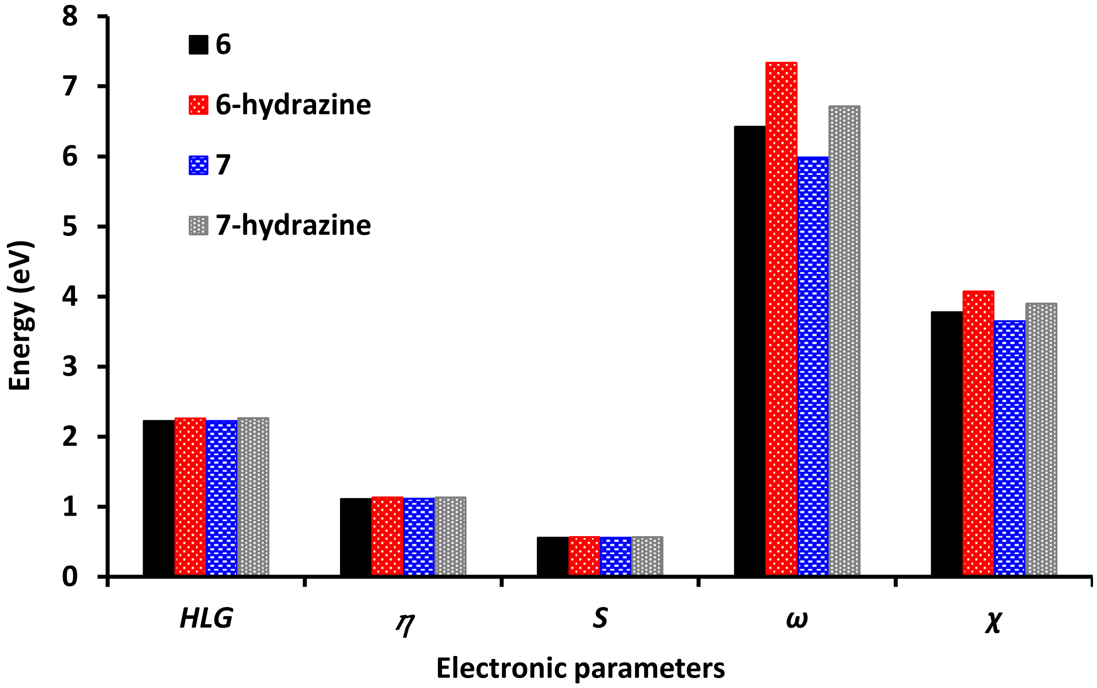

Fig. 5.8: A histogram illustrating the energy differences before and after the introduction of hydrazine as an axial ligand. (HLG = HOMO−LUMO gap).

5.2 Electro-oxidation of nitrite

5.2.1 pH studies

The detection of nitrite also involved the use of both cyclic voltammetry and chronoamperometry. In the preliminary studies in which the influence of the pH was assessed, **GCE-8A** and **GCE-10A** were used. From the voltammograms in **Figs. 5.9A and 5.9B** and the histogram in **Fig. 5.9C**, **GCE-8A** produced the highest I_p at a pH of 7.5 whilst **GCE-10A**, the manganese complex, registered the most favourable I_p at a pH level of 8.0. Consequently, a pH of 7.5 was used for all the CoPcs whilst the studies involving the MnPcs were performed in a phosphate buffer solution (PBS) with a pH level of 8.0. PBS was chosen as the supporting electrolyte as previous literature has reported that the oxidation peak of nitrite is better-resolved in PBS, relative to the acetate and Britton–Robinson buffer solutions [27]. And while it is possible for nitrite to be detected through reduction, oxidation or both, oxidation alone was chosen as the reduction of molecular oxygen falls within the same potential window as the reduction of nitrite [213].

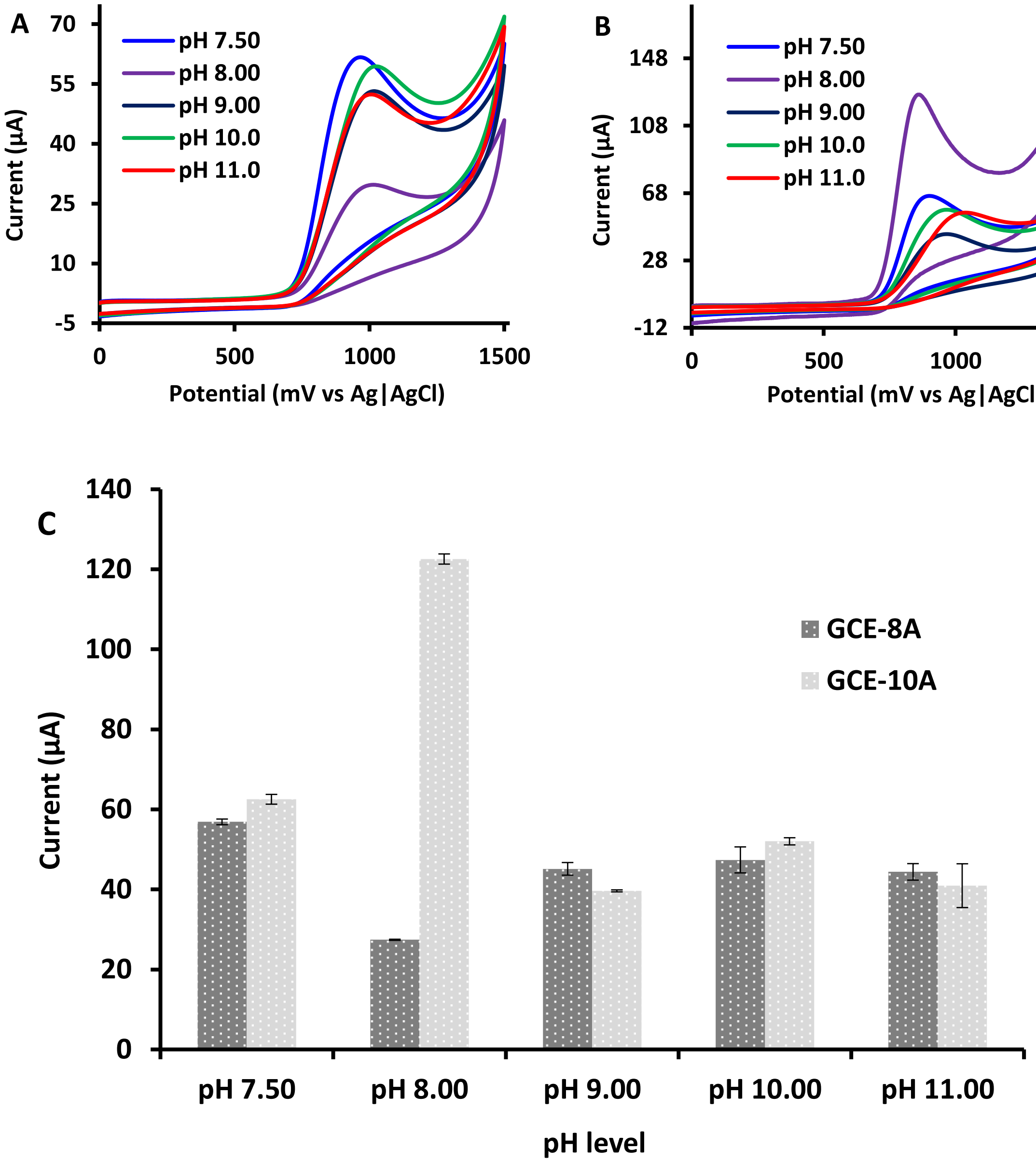

Fig. 5.9: pH studies for **GCE-8A** (**A**) and **GCE-10A** (**B**) and their corresponding bar graphs illustrating a comparative analysis on the peak catalytic currents across the various pH levels (**C**), in 0.10 M PBS, in the presence of 2.0 mM nitrite, all at a scan rate of 100 mV/s.

5.2.2 Voltammetric analyses

The redox potentials seen in the buffers, in the absence of the analyte(s), are sometimes used to make inferences as to what drives the electrochemical reaction between the analyte and the electrode surface (i.e. whether it is the central metal, the Pc's network of π electrons, the substituents or a combination of the aforementioned) [214]. From **Fig. 5.10** and the oxidation potentials for nitrite in **Table 5.5**, the following deductions were made:

- The lowest peak oxidation potentials (E_p) for nitrite were observed in **GCE-8C** and **GCE-10C** with values of 855 mV and 856 mV, respectively.
    - This suggests that clicking is better suited for lowering the E_p relative to electrode modification through adsorption.
- **GCE-12@NGQDs** and **GCE-15A** produced the least desirable E_p value with both registering an E_p of 1018 mV.
    - For **GCE-12@NGQDs**, the result may be attributed to covalent linking to the NGQDs. Amines, similar to alkyls, are good electron-donating groups and by conjugating the two materials together, the potential influence from the $-NH_2$ group of lowering the E_p may have been compromised.
    - An alternative reason, which may be an anomaly but also account for the response observed from **GCE-15A** is that of resonance. The electron-donating or electron-withdrawing ability of amines is dependent on their geometry and so it is possible that the acetaminophenoxy substituent assumes a configuration that renders the molecule more electron-withdrawing than electron-donating [215,216].
- In comparing the symmetric complex (**GCE-9A**) to its asymmetric analogues; for the CoPc derivatives, **GCE-9A** produced the lower E_p value in comparison to the asymmetric complexes showing no advantage for the reduced symmetry.

  - Complex **8** only produced the lower E_p when it was clicked onto the electrode surface (**GCE-8C** with 855 mV versus **GCE-9A** with 952 mV).
- With regards to the MnPc derivatives, the asymmetric **GCE-10A** produced a lower potential with higher currents for nitrite oxidation than its symmetric counterpart **GCE-11A**, showing that the reduction in symmetry is, in some instances, advantageous.
- With respect to the central metals for the molecules adsorbed onto the electrode surface—**GCE-8A** (Co) with **GCE-10A** (Mn) and **GCE-9A** (Co) with **GCE-11A** (Mn), the MnPc derivatives registered the lower peak potential in all cases.
  - MnPcs are reduced easily in comparison to CoPcs [95].
- Regarding the conjugates, in comparison to the Pcs and NGQDs alone, **GCE-9A**, **GCE-12A** and **GCE-NGQDs**, a reduction in the E_p was observed for the π-stacked conjugates (**GCE-9πNGQDs** and **GCE-12πNGQDs**) whilst an increase was observed for the composite formed by covalent means, **GCE-12@NGQDs**.
  - **GCE-NGQDs** produced a result within the range of the CoPcs with an E_p value of 957 mV.

In terms of the peak catalytic current (I_p), the following observations were made (**Table 5.5**):

- The highest I_p was observed for **GCE-10A** with the lowest recorded for **GCE-12πNGQDs**.

- In comparing the symmetric complex (**GCE-9A**) to its asymmetric analogues; for the CoPc derivatives without the NGQDs, variations in the I_p were observed with complexes alone being ranked as follows:

GCE-8C > **GCE-15A** > **GCE-8A** ≥ **GCE-9A** > **GCE-14A** > **GCE-13A** > **GCE-12A**

  - **GCE-8A** being the only exception, produced a similar response to **GCE-9A**.

- With regards to the MnPc derivatives, the asymmetric complex in **GCE-10A** and **GCE-10C** fared better than its symmetric counterpart (**GCE-11A**) irrespective of the method of electrode modification.

- As for the central metals for the molecules adsorbed onto the electrode surface—**GCE-8A** (Co) with **GCE-10A** (Mn) and **GCE-9A** (Co) with **GCE-11A** (Mn), the asymmetric MnPc (**GCE-10A**) produced the better result with a higher I_p value than **GCE-8A**, whilst for the symmetric Pcs, the CoPc (**GCE-9A**) had a slightly better I_p than **GCE-11A**, the MnPc-based electrode.

- Regarding the conjugates, in comparison to the Pcs alone, **GCE-9A** and **GCE-12A**, a decline in the I_p was observed for all the conjugates.

- The bare GCE was also found to elicit an electrochemical response towards the addition of nitrite however, the peak anodic current was observed to be significantly lower than that of the modified electrodes (**Fig. A18**).

In relating the I_p to the surface coverage, to a certain degree, the results are agreeable in that there are no extreme differences. The probes assessed, with surface coverage values ranging from 8.69×10^{-8} mol/cm^2 to 8.40×10^{-7} mol/cm^2, produced I_p values that ranged from 23.7 µA to 123 µA (**Table 5.5**). Taking into consideration what has been reported in the literature, where similar macrocycles with surface coverage values within the 10^{-10} and 10^{-11} mol/cm^2 were reported to produce varying I_p values at the same concentration of the same analyte, nitrite, it can be assumed that the I_p is not governed solely by the surface coverage [217].

Some of these factors that ought to be considered include the pH of the medium in which the electrocatalysis is being performed, the central metal as well as the substituents amongst others. This however, does not imply that a reduction in the surface coverage may not result in an enhancement of the I_p.

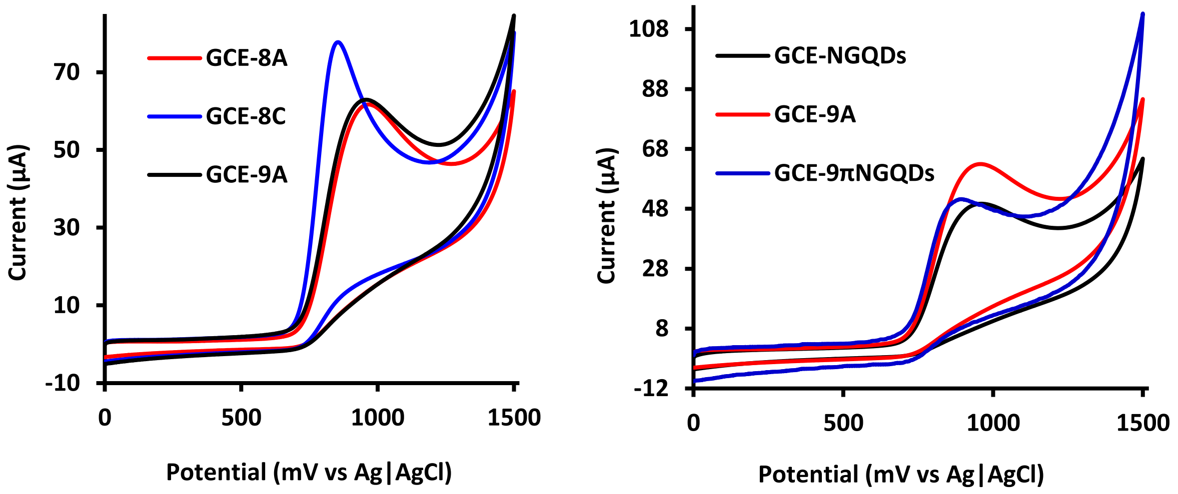

Fig. 5.10: A selection of cyclic voltammograms of the modified electrodes in the presence of 2.0 mM of nitrite in 0.10 M PBS, all at a scan rate of 100 mV/s.

5.2.2.1 Kinetic studies on nitrite-electrode interactions

The kinetic analysis was performed in the same way as it was for hydrazine with the scan rate being varied at a fixed concentration (**GCE-13A** provided as an example in **Fig. 5.11A**). The plot in **Fig. 5.11B** shows a directly proportional relationship between the current and the square root of the scan rate, suggesting a diffusion-controlled process. The slope in the plot of the log I_p vs log v in **Fig. 5.11C** was observed to be 0.42. Similar results were observed for the other electrodes presented in **Table 5.5** with the slopes' proximity to 0.5 being used to infer the electrochemical processes between the analyte and electrode surface as being driven by diffusion.

The Tafel slope values obtained as described by Mohammadizadeh and demonstrated in **Fig. 5.3** all fell within the 60-120 mV/decade range except for **GCE-12@NGQDs**, which was slightly higher (**Table 5.5**) [198]. The magnitude in their deviations however were not extreme hence they too were considered as 1-electron reactions as implied by the Tafel slopes observed for the other probes. Based on these observations, the mechanism in which the oxidation of nitrite was described to proceed in a manner that has been described before according to the following equations, **Eqs. 5.19-5.21** [214]:

$$\mathrm{Co(II)Pc} + \mathrm{NO_2^-} \rightarrow [(\mathrm{NO_2^-})\mathrm{Co(II)Pc}]^- \qquad (\mathbf{5.19})$$

$$[(\mathrm{NO_2^-})\mathrm{Co(II)Pc}]^- \rightarrow (\mathrm{NO_2^-})\mathrm{Co(III)Pc} + e^- \qquad (\mathbf{5.20})$$

$$(\mathrm{NO_2^-})\mathrm{Co(III)Pc} + \mathrm{H_2O} \rightarrow \mathrm{Co(II)Pc} + \mathrm{NO_3^-} + 2\mathrm{H^+} + e^- \qquad (\mathbf{5.21})$$

Equations **5.19** and **5.20** are based on how nitrite has been reported to coordinate to the central metal (nitrite binds axially to cobalt) followed by oxidation of $\mathrm{Co^{2+}}$ to $\mathrm{Co^{3+}}$, which is then followed by a disproportionation reaction in which the cobalt returns to its preferred oxidation state of $\mathrm{Co^{2+}}$ and nitrite is converted to nitrate (**Eq. 5.21**) [214].

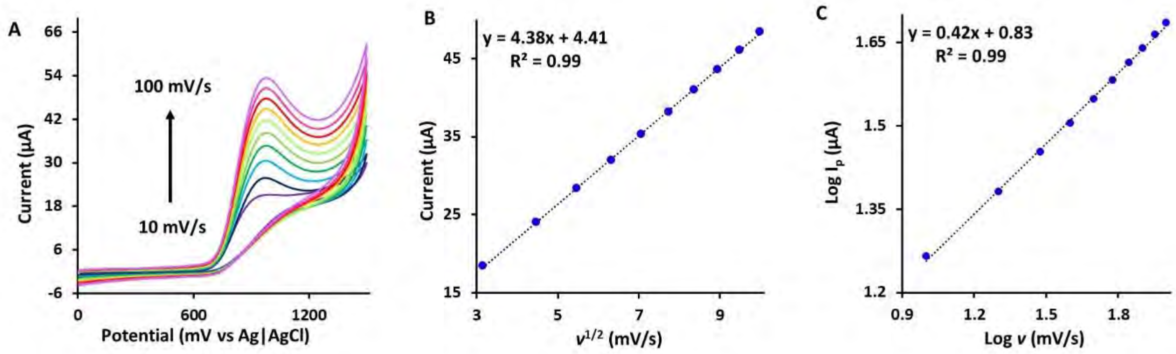

Fig. 5.11: (**A**) is a depiction of the cyclic voltammogram of **GCE-13A** at various scan rates, in the presence of 2.0 mM $\mathrm{NO_2^-}$, in 0.1 M PBS, pH 7.5, (**B**) is the plot of the current against the square root of the scan rate, and (**C**) is the plot of the log I_p against the log of the scan rate, *v*.

Table 5.5: A summary of the voltammetric data obtained in the electrocatalysis of nitrite.

Probe	Γ (mol/cm^2)	E_p (mV) [2.0 mM NO_2^-]	I_p (µA) [2.0 mM NO_2^-]	Tafel slope (mV decade^{-1})
GCE-NGQDs	a	957	45.0	85.1
GCE-8A	2.10×10^{-7}	963	57.5	88.9
GCE-8C	a	855	74.3	84.0
GCE-9A	8.40×10^{-7}	952	57.1	98.6
GCE-9πNGQDs	1.31×10^{-7}	892	45.9	121
GCE-10A	6.57×10^{-8}	858	123	65.8
GCE-10C	a	856	71.5	88.0
GCE-11A	a	875	53.6	99.3
GCE-12A	1.32×10^{-7}	971	45.2	71.3
GCE-12πNGQDs	6.08×10^{-8}	941	23.7	95.3
GCE-12@NGQDs	8.69×10^{-8}	1018	41.2	128
GCE-13A	7.77×10^{-8}	973	48.4	98.8
GCE-14A	6.28×10^{-8}	977	53.0	104
GCE-15A	6.39×10^{-8}	1018	59.1	103

a – No peak/signal in the buffer.

For the Mn(III)Pc , the proposed mechanism, with reasons having being cited in literature, is as follows [**214**]:

$$(L)Mn(III)Pc + NO_2^- \rightarrow (NO_2^-)Mn(III)Pc + L^- \qquad (\mathbf{5.22})$$

$$(NO_2^-)Mn(III)Pc \rightarrow Mn(II)Pc + NO_2^- \qquad (\mathbf{5.23})$$

$$Mn(II)Pc \rightarrow [Mn(III)Pc]^+ + e^- \qquad (\mathbf{5.24})$$

Eq. 5.22 was proposed since the linking of nitrite to Mn(III)Pc and the displacement of the axial ligand has been reported [**214**]. **Eq. 5.23** was proposed since the reduction of the Mn(III)Pc to the Mn (II)Pc by nitrite is known whilst **Eq. 5.24** was brought forward as the Mn(II)

Pc species is formed in the presence of nitrite and oxidation results in the formation of Mn(III)Pc [214].

5.2.2.2 Stability studies

In the same way that the stability of the probes for hydrazine was evaluated, from 20 consecutive cyclic voltammograms, the **GCE-10A** was found to be one of the more stable probes along with **GCE-8A** with a gradual increase in the I_p with an increment in the number of scans (**Fig. 5.12A**). With respect to the I_p, **GCE-8A** was marked by an increment of 15 % after the twentieth scan while for **GCE-10A**, the I_p decreased by a negligible margin of 2 % (**Fig. 5.12B**). **GCE-8C**, **GCE-11A** and **GCE-12πNGQDs** were also found to be one of the more stable probes studied in the electrocatalysis of nitrite with I_p increases of 0.84 %, 9.0 % and 12 % between the first and twentieth scans, respectively. To verify the reproducibility of the sensors, each electrode was fabricated three times and tested in the nitrite solution of the same concentration. The relative standard deviation (% RSD) values ranging from 0.2 to 1.9.

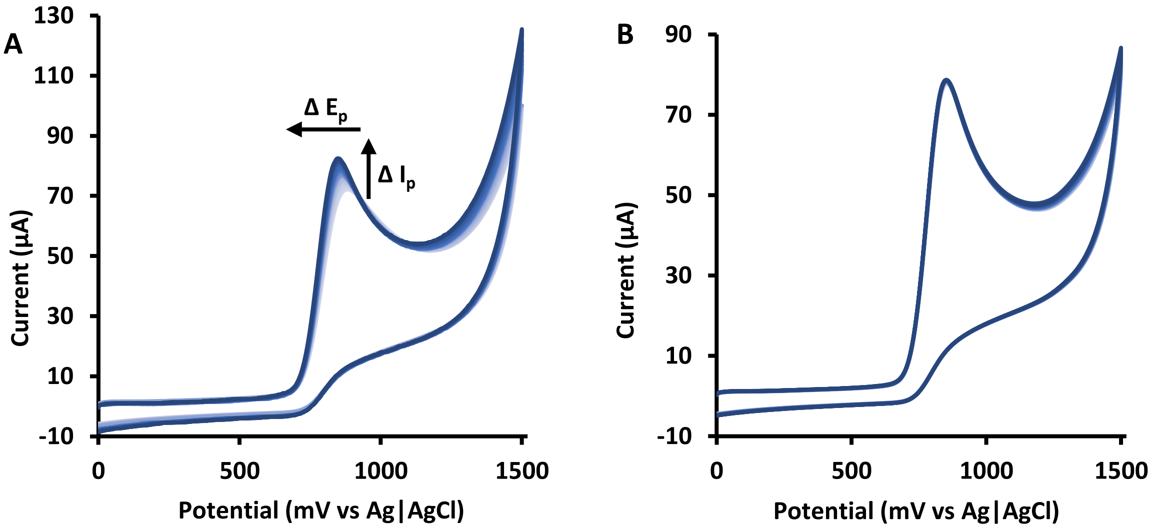

Fig. 5.12: Stability scans for **GCE-8A** (**A**) and **GCE-10A** (**B**) at 100 mV/s in the presence of 2.0 mM of nitrite in 0.10 M PBS.

5.2.3 Interference studies

Upon establishing which of the probes present the most stability (in terms of retaining the peak catalytic current), **GCE-10A** was selected based on its stability for further studies involving foreign ions that are often found to exist in more or less the same environment as nitrite (e.g. soil and water). The selectivity/interference studies were performed using differential pulse voltammetry (DPV) to assess the electrode's response with respect to the magnitude of the peak catalytic current (sulphate ion as an example in **Fig. 5.13**).

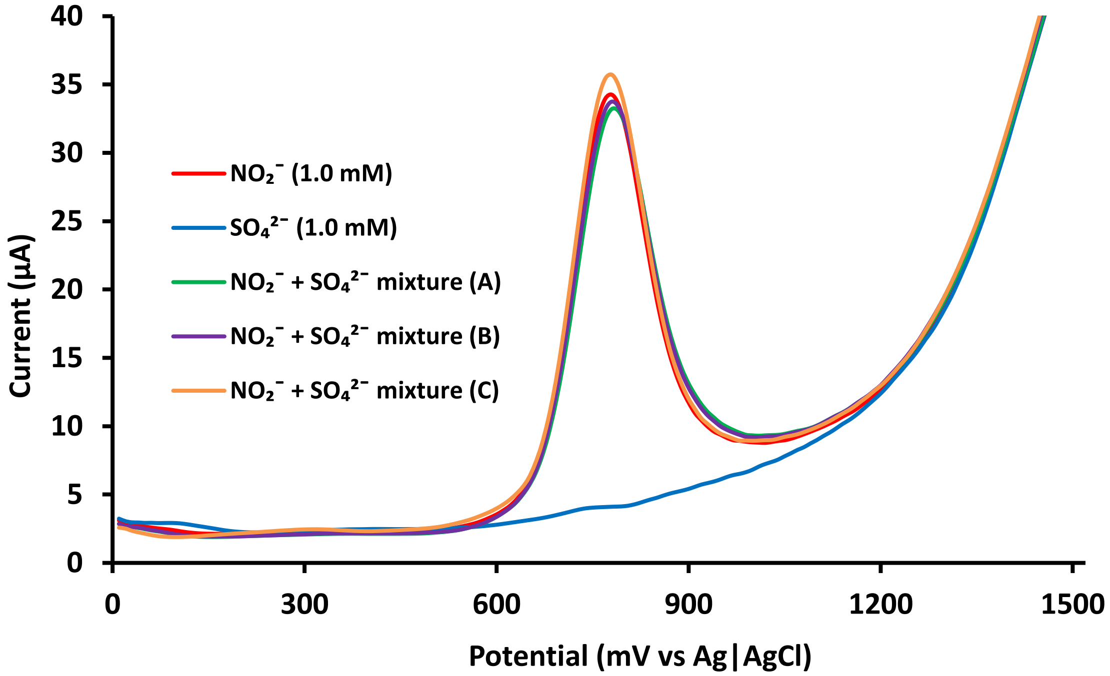

Fig. 5.13: Differential pulse voltammograms for **GCE-10A** in the presence of nitrite and a mixture of nitrite (1.0 mM) and the interferant at different concentrations where mixture (A) 0.5 mM, mixture (B) 1.0 mM and mixture (C) 1.5 mM of the sulphate ion. All in 0.10 M PBS, pH 8.00 at a scan rate of 50 mV/s.

From the differential pulse voltammograms observed in **Fig. 5.13**, it is evident that the interfering ion, sulphate in this case, has little to no influence on **GCE-10A**'s ability to detect nitrite as illustrated by the intensity of the peak catalytic current at various concentrations of the interfering ion relative to the analyte of interest. The same observations were made for **GCE-10A** in the presence of nitrate and chlorine ions with a summary of the findings presented in **Table 5.6**. As observed in **Table 5.6**, **GCE-10A** has a high preference for nitrite as the intensity of the peak catalytic current undergoes subtle changes in the presence of potential interfering ions. These results are also supported by the oxidation potential retaining its original position in the company of the interferants (**Fig. 5.13**).

Table 5.6: Relative response (%) of the sensor in the presence of foreign ions where the concentration of nitrite is fixed at 1.0 mM. Electrode: **GCE-10A**.

Interferant*	0.5 mM	1.0 mM	1.5 mM
NO_3^-	101 (± 1.2)	103 (± 1.2)	106 (± 1.3)
SO_4^{2-}	98.9 (± 2.8)	100 (± 1.9)	104 (± 0.3)
Cl^-	100 (± 1.3)	99.4 (± 1.6)	95.9 (± 0.3)

*Concentration of the interfering ion. Values in brackets represent average standard deviations where *n=3*.

5.2.4 Chronoamperometric analyses

5.2.4.1 Limits of detection

The limits of detection were determined using the same approach as described for hydrazine, using the slope in the inset in **Fig. 5.14A** derived from the chronoamperograms in **Fig. 5.14A** (**GCE-8A** as an example). The sensitivities (slope of the inset in **Fig. 5.14A**) were found to lie between 2.64 µA/mM and 65.4 µA/mM with the MnPcs generally being better than the CoPcs and the π-stacked composite in **GCE-9πNGQDs** eliciting the most desirable response as far as the sensitivity is concerned (**Table 5.7**).

Table 5.7: Electrochemical summary of the chronoamperometric results obtained in the electrochemical sensing of nitrite.

Probe	**Sensitivity (µA/mM)**	**LoD (µM)**	***k*** **($M^{-1}s^{-1}$)**
GCE-NGQDs	25.0 (± 0.3)	2.61 (± 0.1)	3.26×10^{2}
GCE-8A	15.5 (± 0.1)	4.58 (± 0.1)	1.31×10^{1}
GCE-8C	14.8 (± 0.1)	13.0 (± 0.1)	1.10×10^{2}
GCE-9A	2.64 (± 0.1)	7.40 (± 0.1)	9.70×10^{3}
GCE-9πNGQDs	65.4 (± 0.7)	0.70 (± 0.1)	1.01×10^{3}
GCE-10A	19.3 (± 0.1)	6.45 (± 0.1)	1.73×10^{2}
GCE-10C	24.0 (± 0.5)	2.15 (± 0.1)	6.91×10^{6}
GCE-11A	12.4 (± 0.2)	8.99 (± 0.1)	4.26×10^{3}
GCE-12A	18.7 (± 0.04)	5.74 (± 0.1)	7.50×10^{4}
GCE-12πNGQDs	23.1 (± 0.4)	5.27 (± 0.1)	7.46×10^{3}
GCE-12@NGQDs	18.7 (± 0.04)	7.91 (± 0.1)	3.08×10^{4}
GCE-13A	14.1 (± 0.05)	5.89 (± 0.01>)	6.33×10^{3}
GCE-14A	3.44 (± 0.2)	16.4 (± 0.9)	7.34×10^{4}
GCE-15A	3.35 (± 0.4)	60.9 (± 6.1)	2.79×10^{3}

*Values in brackets represent average standard deviations where *n=3*.

With regards to the LoD values, in terms of the Pcs alone, the lowest value was recorded for **GCE-10C** with poorest value being observed for **GCE-15A** (**Table 5.7**). In some cases, regarding the CoPcs, the reduction in symmetry was not found to be beneficial as **GCE-9A** produce a better LoD value than **GCE-8C**, **GCE-14A** and **GCE-15A** (**Table 5.7**). As for the MnPcs, the asymmetric complex produced a better LoD value relative to its symmetric complex irrespective of the method of electrode modification (**GCE-10A** and **GCE-10C** > **GCE-11A**, **Table 5.7**). The best-performing electrode in terms of the LoD however, was **GCE-9πNGQDs** with a value of 0.70 µM illustrating that the combination of Pcs with carbon-based nanomaterials has the ability to enhance the electrochemical response of electrodes (**Table 5.7**).

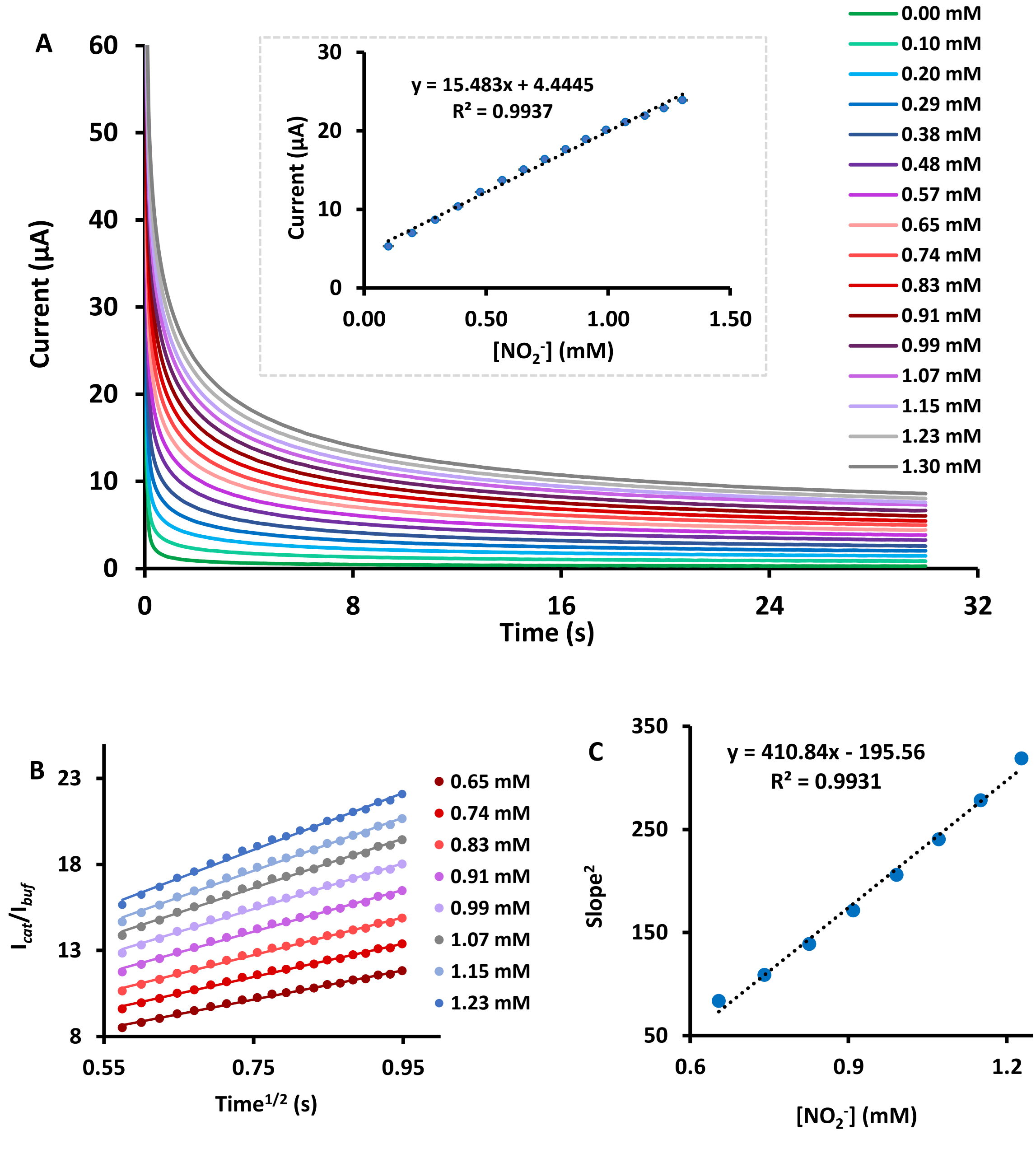

Fig. 5.14: (**A**) Chronoamperograms for **GCE-8A** in different concentrations of nitrite (in 0.10 M PBS, pH 7.50). Inset: calibration curve for **GCE-8A**. Error bars not visible because all standard deviations are 0.01> (*n = 3*). Plots of the I_{cat}/I_{buf} versus the square root of time (**B**) and a plot of the slope^2 against the concentration of nitrite (**C**) (**GCE-8A** used as an example).

The LoD values observed in **Table 5.7** are comparable (better in some instances) to those that have been reported in literature as seen in **Table 5.8** [131,218-220]. Furthermore, these results illustrate a window of improvement through the inclusion or addition of other materials such as nanoparticles as the majority of the catalysts in this work are applied as single entities with the exception of two of the complexes reported (complexes **9** and **12** in **GCE-9πNGQDs**, **GCE-12πNGQDs** and **GCE-12@NGQDs**). The limits of detection obtained in this thesis are well below a value considered to be the maximum amount permissible in drinking water from the World Health Organization (WHO, 65.2 µM) [221].

Table 5.8: Limits of detection for nitrite in comparison with literature values for CoPc and MnPc derivatives.

Probe/electrode	E_p (V)	pH (PBS)	LoD (µM)*	Ref.
GCE-CoTM-QOPc/CNP[a]	0.79	7.00	0.06 (DPV) 0.03 (CA)	[131]
[TMPyPcCo/aCNTs]$_{12}$[b]	~0.90	6.20	2.60 (CA)	[218]
GCE-Pd/CoPc[c]	0.90	7.00	0.10 (DPV)	[219]
CCE-SiO_2/C/MnPc[d]	~0.95	4.00	0.02 (CV)	[220]
GCE-9πNGQDs	0.89	7.50	0.70 (CA)	This work
GCE-10C	0.86	8.00	2.15 (CA)	This work

*Method in which the LoD was determined - CV = cyclic voltammetry, DPV = differential pulse voltammetry, CA = chronoamperometry

a – Cobalt(II) tetra methyl-quinoline oxy bridged phthalocyanine

b – Cationic 2,9,16,23-tetra[4-(*N*-methyl)pyridinyloxy]phthalocyanine cobalt(II) ($[TMPyPcCo]^{4+}$) and acid-treated multiwalled carbon nanotubes (aCNTs)

c – Cobalt phthalocyanine supported palladium nanoparticles

d – Mesoporous Carbon Ceramic SiO_2/C Electrode where C is graphite and manganese(II) phthalocyanine

5.2.4.2 Catalytic rates

The chronoamperometric analysis was used to determine the catalytic rates as well as the limits of detection. From the chronoamperograms in **Fig. 5.14A** (**GCE-8A** as an example), it is evident that the probe yields an increase in current with the increase in the concentration of nitrite. From this data, using **Eq. 5.6** and the plots in **Figs. 5.14B** and **Fig. 5.14C**, the catalytic rates were determined (**Table 5.7**). From the figures in **Table 5.7**, the highest catalytic rate was found to exist for **GCE-10C** with the lowest being for **GCE-8A** with values of 6.91×10^6 s^{-1} M^{-1} and 1.31×10^1 s^{-1} M^{-1} respectively. With the exception of a few probes, the majority of the modified electrodes displayed a fairly high catalytic rate with an exponential of either 10^3 or 10^4 (**Table 5.7**).

5.3 Summary of chapter

The electrochemical sensing of both hydrazine and nitrite was performed using cyclic voltammetry and chronoamperometry. From these techniques, various electrochemical parameters such as the Tafel slope and the limit of detection (LoD) were established, which enabled the determination of the possible reaction mechanism(s) as well as the suitability for potential usage in practical applications (i.e. real-life analysis).

With respect to the probes designed for the detection of hydrazine, the pentadecylphenoxy-based electrodes were generally better than those derived from the *tert*-butyl-containing complexes irrespective of the technique, cyclic voltammetry or chronoamperometry. The only exception was the significant reduction in the oxidation potential for the *tert*-butyl-based electrodes. The computational chemistry results for **GCE-6A** and **GCE-7A** showed that by identifying the relevant parameters, taking into consideration the differences in the structure of the Pcs, to a certain extent, theoretical calculations can be used to predict the electrochemical responses of the designed probes.

A great deal of variation was observed in the sensors designed for nitrite with some of the differences being attributed to the method of electrode modification, the presence of nanomaterials and/or the differences in the central metals (Co(II) vs Mn(III)). Looking at all the probes for nitrite in their totality, in terms of the LoD, the best result was observed for the probe fashioned from the Pc-NGQD composite, demonstrating the potential that nanomaterials possess in terms of enhancing the electrochemical behaviour of Pcs.

CHAPTER 6

CONCLUSIONS AND PROSPECTS

General conclusions and future recommendations are presented in this chapter.

6. General conclusions, future prospects and recommendations

6.1 General conclusions

In summarising the work presented in this thesis, novel symmetric and asymmetric CoPcs and MnPcs were synthesized and characterised. The rationale behind the design of the A_3B Pcs was to create push-pull systems in which the substituents are complementary to each other, to explore how the asymmetric component can be manoeuvred to enhance the electrocatalytic activity of the Pcs (i.e. clicking onto the electrode surface and/or conjugating to nanomaterials by covalent means) and to assess whether all asymmetric Pcs perform better than their symmetric variants or if there are exceptions.

In carrying out the assessment, the Pcs were applied as electrocatalysts in the oxidation of hydrazine and nitrite. The sensors applied in the detection of hydrazine showed that there are instances where symmetric Pcs yield better results than their asymmetric derivatives. In the general sense however, the asymmetric Pcs were found to be more favourable than the symmetric complexes.

Regarding the detection of nitrite, a similar observation was made in that the asymmetric complexes are not always better than the symmetric Pc. From this observation, it can be inferred that the coupling of substituents in asymmetric Pcs has a significant influence on the electrocatalytic activity of Pcs hence it cannot always be assumed that all asymmetric Pcs are better than those with a higher symmetry, A_4-type Pcs.

6.2 Future prospects and recommendations

With the number of symmetric Pcs that have been reported, variations in substituents in A_3B-type Pcs can be considered limitless. This work provides some insight into how the structure of Pcs can be tailored to elicit certain responses such as lowering the oxidation potential and the limit of detection. Based on the work presented in this thesis, the following recommendations are made:

- The synthetic routes for asymmetric Pcs need to be improved in such a way that there is less of the side-products.
    - A more detailed study focusing on varying the solvents, reaction times, the central metal as well as the base needs to be conducted.
- Regarding further tuning of the Pcs, having noted that the yields obtained in the asymmetric Pcs are quite low, it is suggested that a linker in the form of a di-phthalonitrile is used in synthesizing binuclear Pcs instead of synthesizing the Pc or Pcs separately before linking them together.
- Computational methods should be considered in elucidating the mechanisms with a consideration made for the fact that in tetra-substituted Pcs, for both A_4 and A_3B Pcs, regioisomers exist which may account for the differences observed.
    - The inclusion of the electrode surface, while it may not be completely accurate, may also be beneficial in this regard.
- Attempts at fabricating the electrode with the electrocatalysts embedded within is also an aspect worth considering.
    - This may improve the electrocatalytic behaviour of the Pcs and aid in the production of the sensors in bulk.
- The method of conjugating the NGQDs to Pcs is one that also requires optimization so that it possible to estimate the loading of Pc-to-NGQDs based on the duration of the reaction.

REFERENCES

1. A. A. Zagorodni in: *Ion Exchange Materials: Properties and Applications*. Amsterdam: Elsevier, **2007**.
2. P. A. Deshpande, G. Madras, *Catalytic Synthesis of CO Free Hydrogen*. In: S. L. Suib (Ed.) New and Future Developments in Catalysis: Activation of Carbon Dioxide. Amsterdam: Elsevier, **2013**, pp. 223–252.
3. P. W. N. van Leeuwen, *Catalysis, Homogeneous*. In: R. A. Meyers (Ed.) Encyclopedia of Physical Science and Technology (3rd edition). Oxford: Academic Press, **2003**, pp. 457–490.
4. G. Valero, A. Moyano, *Searching for Spontaneous Mirror-Symmetry Breaking in Organoautocatalytic Reactions.* In: G. Pályi, R. Kurdi and C. Zucchi (Eds.) Advances in Asymmetric Autocatalysis and Related Topics. Oxford: Academic Press, **2017**, pp. 241–258.
5. Y. Wu, Y. Liang, H. Wang, Heterogeneous molecular catalysts of metal phthalocyanines for electrochemical CO_2 reduction reactions, Acc. Chem. Res. 54 (**2021**) 3149–3159.
6. S. Coyle, V. F. Curto, F. Benito-Lopez, L. Florea, D. Diamond, *Wearable Bio and Chemical Sensors*. In: E. Sazonov and M. R. Neuman (Eds.) Wearable Sensors. Oxford: Academic Press, **2014**, pp. 65–83.
7. S. I. Dorovskikh, D. D. Klyamer, A. D. Fedorenko, N. B. Morozova, T. V. Basova, Electrochemical sensor based on iron(II) phthalocyanine and gold nanoparticles for nitrite detection in meat products, Sensors 22 (**2022**) 5780.
8. M. D. Brown, M. H. Schoenfisch, Catalytic selectivity of metallophthalocyanines for electrochemical nitric oxide sensing, Electrochim. Acta 273 (**2018**) 98–104.
9. C. S. J. N. O’Donoghue, G. Fomo, T. Nyokong, Electrode modification using alkyne manganese phthalocyanine and click chemistry for electrocatalysis, Electroanalysis 28 (**2016**) 3019–3027.
10. W. Boumya, N. Taoufik, M. Achak, N. Barka, Chemically modified carbon-based electrodes for the determination of paracetamol in drugs and biological samples, J. Pharm. Anal. 11 (**2021**) 138–154.
11. F. Faridbod, V. K. Gupta, H. A. Zamani, Electrochemical sensors and biosensors, Int. J. Electrochem. 2011 (**2011**) 1–2.

12. I. M. Kolthoff, C. Wang, Electrode potentials of platinum, gold, and silver in various solutions of electrolytes, J. Phys. Chem. 41 (**1937**) 539–544.
13. C. Hu, Y. Xiao, Y. Zou, L. Dai, Carbon-based metal-free electrocatalysis for energy conversion, energy storage, and environmental protection, EER 1 (**2018**) 84–112.
14. A. Pandey, S. Sharma, R. Jain, A. N. Raja, Review—Pencil graphite electrode: An emerging sensing material, J. Electrochem. Soc. 167 (**2020**) 037501.
15. M.-Y. Cho, J. H. Lee, S.-H. Kim, J. S. Kim, S. Timilsina, An extremely inexpensive, simple, and flexible carbon fiber electrode for tunable elastomeric piezo-resistive sensors and devices realized by LSTM RNN, ACS Appl. Mater. Interfaces 11 (**2019**) 11910–11919.
16. Y. Yi, G. Weinberg, M. Prenzel. M. Greiner, S. Heumann, S. Becker, R. Schögl, Electrochemical corrosion of a glassy carbon electrode, Catal. Today 295 (**2017**) 32–40.
17. M. K. Puglia, P. K. Bowen, Cyclic voltammetry study of noble metals and their alloys for use in implantable electrodes, ACS Omega 7 (**2022**) 34200–34212.
18. I. Švancara, K. Vytřas, K. Kalcher, A. Walcarius, J. Wang, Carbon paste electrodes in facts, numbers, and notes: A review on the occasion of the 50-years jubilee of carbon paste in electrochemistry and electroanalysis, Electroanalysis 21 (**2009**) 7–28.
19. I. Švancara, J. Zima, Possibilities and limitations of carbon paste electrodes in organic electrochemistry, Curr. Org. Chem. 15 (**2011**) 3043–3058.
20. B. Guo, J. Anzai, T. Osa, Modification of a glassy carbon electrode with diols for the suppression of electrode fouling in biological fluids, Chem. Pharm. Bull. 44 (**1996**) 860–862.
21. B. G. Baker, D. A. J. Rand, R. Woods, A comparison of electrochemical and Auger analysis of the surface composition of platinum-rhodium alloys, J. Electroanal. Chem. 97 (**1979**) 89–198.
22. Y. N. Loginov, A. E. Perivkhin, N. A. Babailov, Evolution of surface defects in platinum alloy wire under drawing. AIP Conference Proceedings 1915 (**2017**) 040032.
23. L. D. Burke, J. M. Moran, P. F. Nugent, Cyclic voltammetry responses of metastable gold electrodes in aqueous media, J. Solid State Electrochem. 7 (**2003**) 529–538.
24. M. J. Nicol, The anodic behaviour of gold, Gold Bull. 13 (**1980**) 46–55.
25. J. I. Gowda, S. T. Nandibewoor, Electrochemical behavior of paclitaxel and its determination at glassy carbon electrode, Asian J. Pharm. 9 (**2014**) 42–49.

26. C. Damphathik, P. Butmee, K. Kunpatee, K. Kalcher, A. Ortner, M. Kerr, J. Jitcharoen, A. Samphao, An electrochemical sensor for the voltammetric determination of artemisinin based on carbon materials and cobalt phthalocyanine, Microchim. Acta 189 (**2022**) 224.

27. K. Zhao, H. Song, S. Zhuang, L. Dai, P. He, Y. Fang, Determination of nitrite with the electrocatalytic property to the oxidation of nitrite on thionine modified aligned carbon nanotubes, Electrochem. commun. 9 (**2007**) 65–70.

28. N. W. Polaske, H.-C. Lin, A.Tang, M. Mayukh, L. E. Oquendo, J. T. Green, E. L. Ratcliff, N. R. Armstrong, S. S. Saavedra, D. V. McGrath, Phosphonic acid functionalized asymmetric phthalocyanines: Synthesis, modification of indium tin oxide, and charge transfer, Langmuir 27 (**2011**) 14900–14909.

29. J. A. Bennet, K. L. Sterling, J. E. Pander III, Direct metal substitution of electropolymerized ferriprotoporphyrin: A simple electrode-modification process for developing electrocatalytic materials, ECS Electrochem. Lett. 2 (**2013**) H37–H39.

30. G. Ramirez, M. C. Goya, L. Mendoza, B. Matsuhiro, M. Isaacs, Y.-Y. Chen, M. C. Arévalo, J. Henríquez, W. Cheuquepán, M. J. Aguirre, Iron porphyrin-modified electrodes: Influence of the method of modification on the stability and electroactivity in oxidation of sulfite or hydrogensulfite in ethanol–water solutions, J. Coord. Chem. 62 (**2009**) 2782–2791.

31. M. Delamar, R. Hitmi, J. Pinson, J. M. Saveant, Covalent modification of carbon surfaces by grafting of functionalized aryl radicals produced from electrochemical reduction of diazonium salts, J. Am. Chem. Soc. 114 (**1992**) 5883–5884.

32. P. Mashazi, T. Nyokong, Electrocatalytic studies of covalently immobilized metal tetra-amino phthalocyanines onto derivatized screen-printed gold electrodes, Microchim. Acta 171 (**2010**) 321–332.

33. S. G. Agalave, S. R. Maujan, V. S. Pore, Click Chemistry: 1,2,3-triazoles as pharmacophores, Chem. Asian J. 6 (**2011**) 2696–2718.

34. S. R. Nxele, P. Mashazi, T. Nyokong, Electrode modification using alkynyl substituted Fe(II) phthalocyanine via electrografting and click chemistry for electrocatalysis, Electroanalysis 27 (**2015**) 2468–2478.

35. K. Pei, T. Zhai, Emerging 2D organic-inorganic heterojunctions, Cell Rep. 1 (**2020**) 100166.

36. M. Bacon, S. J. Bradley, T. Nann, Graphene quantum dots, Part. Part. Syst. Charact. 31 (**2014**) 415–428.
37. S. Benítez-Martínez, M. Valcárcel, Graphene quantum dots in analytical science, Trends Anal. Chem. 72 (**2015**) 93–113.
38. A. K. Geim, Graphene: Status and prospects, Science 324 (**2009**) 1530–1534.
39. X. Niu, Y. Li, H. Shu, J. Wang, Revealing the underlying absorption and emission mechanism of nitrogen doping graphene quantum dots, Nanoscale 8 (**2016**) 19376–19382.
40. Y. Dong, J. Shao, C. Chen, H. Li, R. Wang, Y. Chi, X. Lin, G. Chen, Blue luminescent graphene quantum dots and graphene oxide prepared by tuning the carbonization degree of citric acid, Carbon 50 (**2012**) 4738–4743.
41. J. Drbohlavova, V. Adam, R. Kizek, J. Hubalek, Quantum dots — Characterization, preparation and usage in biological systems, Int. J. Mol. Sci. 10 (**2009**) 656–673.
42. D. Iannazzo, A. Pistone, M. Salamò, S. Galvagno, R. Romeo, S. V. Giofré, C. Branca, G. Visalli, A. Di Pietro, Graphene quantum dots for cancer targeted drug delivery, Int. J. Pharm. 518 (**2017**) 185–192.
43. J. Shen, Y. Zhu, X. Yang, C. Li, Graphene quantum dots: emergent nanolights for bioimaging, sensors, catalysis and photovoltaic devices, Chem. Commun. 48 (**2012**) 3686–3699.
44. M. Arvand, S. Hemmati, Analytical methodology for the electro-catalytic determination of estradiol and progesterone based on graphene quantum dots and poly(sulfosalicylic acid) co-modified electrode, Talanta 174 (**2017**) 243–255.
45. F. Chen, W. Gao, X. Qiu, H. Zhang, L. Liu, P. Liao, W. Fu, Y. Luo, Graphene quantum dots in biomedical applications: Recent advances and future challenges, Frontiers in Laboratory Medicine 1 (**2017**) 192–199.
46. K. Bhattacharya, S. P. Mukherjee, A. Gallud, S. C. Burkert, S. Bistarelli, S. Bellucci, M. Bottini, A. Star, B. Fadeel, Biological interactions of carbon-based nanomaterials: From coronation to degradation, Nanomedicine 12 (**2016**) 333–351.
47. S. Bak, D. Kim, H. Lee, Graphene quantum dots and their possible energy applications: A review, Curr. Appl. Phys. 16 (**2016**) 1192–1201.

48. X. Tong, Q. Wei, X. Zhan, G. Zhang, S. Sun, The new graphene family materials: Synthesis and applications in oxygen reduction reaction, Catalysts 7 (**2017**) https://doi.org/10.3390/catal7010001.

49. S. J. Bradley, R. Kroon, G. Laufersky, M. Röding, R. V. Goreham, T. Gschneidtner, K. Schroeder, K. Moth-Poulsen, M. Andersson, T. Nann, Heterogeneity in the fluorescence of graphene and graphene oxide quantum dots, Microchim. Acta 184 (**2017**) 871–878.

50. B. Zheng, Y. Chen, P. Li, Z. Wang, B. Cao, F. Qi, J. Liu, Z. Qiu, W. Zhang, Ultrafast ammonia-driven, microwave-assisted synthesis of nitrogen-doped graphene quantum dots and their optical properties, Nanophotonics 6 (**2017**) 259–267.

51. C. Zhao, X. Song, Y. Liu, Y. Fu, L. Ye, N. Wang, F. Wang, L. Li, M. Mohammadniaei, M. Zhang, Q. Zhang, J. Liu, Synthesis of graphene quantum dots and their applications in drug delivery, J. Nanobiotechnol. 18 (**2020**) 142.

52. J. Ju, W. Chen, Synthesis of highly fluorescent nitrogen-doped graphene quantum dots for sensitive, label-free detection of Fe (III) in aqueous media, Biosens. Bioelectron. 58 (**2014**) 219–225.

53. S. Sangam, A. Gupta, A. Shakeel, R. Bhattacharya. A. K. Sharma, D. Suhag, S. Chakrabarti, S. K. Garg, S. Chattopadhyay, B. Basu, V. Kumar, S. K. Rajput, M. K. Dutta, M. Mukherjee, Sustainable synthesis of single crystalline sulphur-doped graphene quantum dots for bioimaging and beyond, Green Chem. 20 (**2018**) 4245–4259.

54. C. Wang, D. Chen, S. Tang, Y. Yang, X. Li, F. Xie, Q. Guo, PVDF-triggered multicolor fluorine-doped graphene quantum dots for water detection and anti-counterfeiting, Microchim. Acta 189 (**2021**) 6.

55. S. Chung, R. A. Revia, M. Zhang, Graphene quantum dots and their applications in bioimaging, biosensing, and therapy, Adv. Mater. 33 (**2021**) 1904362.

56. C. G. Claessens, U. Hahn, T. Torres, Phthalocyanines: From outstanding electronic properties to emerging applications, Chem. Rec. 8 (**2008**) 75–97.

57. K. Mitra, M. C. T. Hartman, Silicon phthalocyanines: Synthesis and resurgent applications, Org. Biomol. Chem. 19 (**2021**) 1168–1190.

58. J. F. van Staden, Application of phthalocyanines in flow- and sequential-injection analysis and microfluidics systems: A review, Talanta 139 (**2015**) 75–88.

59. Y. Liu, D. Zhu, *Asymmetrical Phthalocyanines*. In: H. S. Nalwa (Ed.) Handbook of Surfaces and Interfaces of Materials. Oxford: Academic Press, **2001**, pp. 405–438.

60. X. Li, B.-D. Zheng, X.-H. Peng, S.-Z. Li, J.-W. Ying, Y. Zhao, J.-D. Huang, J. Yoon, Phthalocyanines as medicinal photosensitizers: Developments in the last five years, Coord. Chem. Rev. 379 (**2017**) 147–160.
61. C. Constantin, A.-R. Lupu, T. E. Fertig, M. Gherghiceanu, S. Pop, R.-M. Ion, M. Neagu, Unveiling Ga(III) phthalocyanine—a different photosensitizer in neuroblastoma cellular model, J. Cell. Mol. Med. 23 (**2019**) 1086–1094.
62. C. W. Foster, J. Pillay, J. P. Metters, C. E. Banks, Cobalt phthalocyanine modified electrodes utilised in electroanalysis: Nano-structured modified electrodes vs. bulk modified screen-printed electrodes, Sensors 14 (**2014**) 21905–21922.
63. T. V. Basova, A. K. Ray, Review—Hybrid materials based on phthalocyanines and metal nanoparticles for chemiresistive and electrochemical sensors: A mini-review, ECS J. Solid State Sci. Technol. 9 (**2020**) 061001.
64. D. Akyüz, A. Koca, An electrochemical sensor for the detection of pesticides based on the hybrid of manganese phthalocyanine and polyaniline, Sens. Actuators B Chem. 283 (**2019**) 848–856.
65. M. Yahya, Y. Nural, Z. Seferoğlu, Recent advances in the nonlinear optical (NLO) properties of phthalocyanines: A review, Dyes Pigm. 198 (**2022**) 109960.
66. M. Urbani, M.-E. Ragoussi, M. K. Nazeeruddin, T. Torres, Phthalocyanines for dye-sensitized solar cells, Coord. Chem. Rev. 381 (**2019**) 1–64.
67. T. Furuyama, T. Ishii, N. Ieda, H. Maeda, M. Segi, M. Uchiyama, H. Nakagawa, Cationic axial ligands on sulfur substituted silicon(IV) phthalocyanines: Improved hydrophilicity and exceptionally red-shifted absorption into the NIR region, Chem. Commun. 55 (**2019**) 7311–7314.
68. J. Mack, N. Kobayashi, Low symmetry phthalocyanines and their analogues, Chem. Rev. 111 (**2011**) 281–321.
69. D. K. MacFarland, C. M. Hardin, M. J. Lowe, A phthalocyanine synthesis group project for general chemistry, J. Chem. Educ. 77 (**2000**) 1484–1485.
70. V. Rădiþoiu, L. Wagner, A. Rădiþoiu, P. Ardeleanu, V. Amăriuþei, A. Sorescu, Synthesis and characterization of some phthalic acid derivatives precursors for phthalocyanine chromogens, Rev. Chim. 59 (**2008**) 973–978.
71. K. Sakamoto, E. Ohno-Okumura, Syntheses and functional properties of phthalocyanines, Materials 2 (**2009**) 1127–1179.

72. M. A. Dahlen, The phthalocyanines a new class of synthetic pigments and dyes, Ind. Eng. Chem. 31 (**1939**) 839–847.

73. V. N. Nemykin, E. A. Luk'yanets, Synthesis of substituted phthalocyanines, Arkivoc 2010 (**2010**) 136–208.

74. T. F. M. de Souza, F. C. T. Antonio, M. Zanotto, P. Homem-de-Mello, A. O. Ribeiro, Photophysical and photochemical properties and aggregation behavior of phthalocyanine and naphthalocyanine derivatives, J. Braz. Chem. Soc. 29 (**2018**) 1199–1209.

75. D. Gounden, G. N. Ngubeni, M. S. Louzada, S. Khene, J. Britton, N. Nombona, Synthesis, spectroscopic and DFT Characterization of 4β-(4-*tert*-butylphenoxy)phthalocyanine positional isomers for non-linear optical absorption, S. Afr. J. Chem. 70 (**2017**) 49–59.

76. J. Sforzini, F. C. Bocquet, F. S. Tautz, Adsorption-induced symmetry reduction of metal-phthalocyanines studied by vibrational spectroscopy, Phys. Rev. B 96 (**2017**) 165410–165422.

77. C. Murray, N. Dozova, J. G. McCaffrey, S. FitzGerald, N. Shafizadeh, C. Crépin, Infra-red and Raman spectroscopy of free-base and zinc phthalocyanines isolated in matrices, Phys. Chem. Chem. Phys. 12 (**2010**) 10406–10422.

78. V. N. Nemykin, S. V. Dudkin, F. Dumoulin, C. Hirel, A.G. Gürek, V. Ahsen, Synthetic approaches to asymmetric phthalocyanines and their analogues, Arkivoc 2014 (**2014**) 142–204.

79. N. B. McKeown, *Phthalocyanines*. In: J. A. McCleverty and T. J. Meyer (Eds.) Comprehensive Coordination Chemistry II. United Kingdom: Elsevier, **2003**, pp. 507–514.

80. L. Zhao, S. Li, Y. Liu, R. Xing, X. Yan, Kinetically controlled self-assembly of phthalocyanine–peptide conjugate nanofibrils enabling superlarge redshifted absorption, Chinese Chem. Soc. Chem. 1 (**2019**) 173–180.

81. M. A. Bartlett, J. Sundermeyer, Group 10 metal–thiocatecholate capped magnesium phthalocyanines – coupling chromophore and electron donor/acceptor entities and its impact on sulfur induced red-shifts, Dalton Trans. 47 (**2018**) 16255–16263.

82. J. Mack, M. J. Stillman, Assignment of the optical spectra of metal phthalocyanine anions, Inorg. Chem. 36 (**1997**) 413–425.

83. B. Brozeka-Pulska, M. Orlikowski, H. Abramcyzk, *Phthalocyanines: From Dyes to Photosensitizers in Diagnostics and Treatment of Cancer. Spectroscopy and Raman Imaging Studies of Phthalocyanines in Human Breast Tissues.* In: K. M. Kadish, K. M. Smith and R. Guilard (Eds.) Handbook of Porphyrin Science. World Scientific Publishing, **2020**, pp. 1–49.
84. T. Nyokong, *Electronic Spectral and Electrochemical Behavior of Near Infrared Absorbing Metallophthalocyanines*. In: J. Jiang (Ed.) Functional Phthalocyanine Molecular Materials. Berlin: Springer, **2010**, pp. 45–87.
85. E. A. Ough, Z. Gasyna, M. J. Stillman, Photochemical, electrochemical, and chemical formation of the π-cation-radical species of magnesium phthalocyanine. Analysis of the absorption and MCD spectra of $[MgPc(-1)]^{\bullet+}$, Inorg. Chem. 30 (**1991**) 2301–2310.
86. T.-H. Huang, K. E. Rieckhoff, E. M. Voight, New singlets in the phthalocyanines, J. Chem. Phys. 77 (**1982**) 3424–3441.
87. K. Sakamoto, *Cyclic Voltammetry of Phthalocyanines*. In: N. W. Maxakato, S. S. Gwebu, G. H. Mhlongo (Eds.) Voltammetry. London, United Kingdom, IntechOpen, **2019** [Online]. Available from: https://www.intechopen.com/chapters/63960 (Accessed: 30 November 2022).
88. M. Arıcı, D. Arıcan, A. L. Uğur, A. Erdoğmuş, Electrochemical and spectroelectrochemical characterization of newly synthesized manganese, cobalt, iron and copper phthalocyanines, Electrochim. Acta 87 (**2013**) 554–566.
89. M. Peterson, C. Hunt, Z. Wang, S. E. Heinrich, G. Wu, G. Ménard, Synthesis, characterization, and electrochemical properties of a first-row metal phthalocyanine series, Dalton Trans. 49 (**2020**) 16268–16277.
90. M. Özçeşmeci, I. Nar, E. Hamuryudan, Synthesis and electrochemical and spectroelectrochemical characterization of chloromanganese(III) phthalocyanines, Turk. J. Chem. 38 (**2014**) 1064–1072.
91. J. Obirai, T. Nyokong, Synthesis, spectral and electrochemical characterization of mercaptopyrimidine-substituted cobalt, manganese and Zn (II) phthalocyanine complexes, Electrochim. Acta 50 (**2005**) 3296–3304.
92. İ. Acar, E. T. Saka, S. Topçu, Z. Bıyıklıoğlu, H. Kantekin, A. Aktaş, Synthesis and electrochemistry of new octa-substituted metal-free and metallophthalocyanines, J. Coord. Chem. 68 (**2015**) 1847–1858.

93. T. Nyokong, Electrochemistry of some second-row transition-metal phthalocyanine complexes, S. Afr. J. Chem. 48 (**1995**) 23–29.
94. T. Nyokong, The nature of the oxidation products of dicyanoruthenium phthalocyanine in aqueous and non-aqueous solvents, Polyhedron 12 (**1993**) 375–381.
95. A. B. P. Lever, E. R. Milaeva, G. Speier, *The Redox Chemistry of Metallophthallocyanines in Solution*. In: C. C. Leznoff and A. B. P. Lever (Eds.) Phthalocyanines: Properties and Applications. New York: VCH, **1993**, pp. 1–69.
96. S. Centane, O. J. Achadu, T. Nyokong, Effects of substituents on the electrocatalytic activity of cobalt phthalocyanines when conjugated to graphene quantum dots, Electroanalysis 29 (**2017**) 2470–2482.
97. S. Centane, T. Nyokong, Impedimetric aptasensor for HER2 biomarker using graphene quantum dots, polypyrrole and cobalt phthalocyanine modified electrodes, Sens. Bio-Sens. Res. 34 (**2021**) 100467.
98. S. Centane, E. K. Sekhosana, R. Matshitse, T. Nyokong, Electrocatalytic activity of a push-pull phthalocyanine in the presence of reduced and amino functionalized graphene quantum dots towards the electrooxidation of hydrazine, J. Electroanal. Chem. 820 (**2018**) 146–160.
99. R. Nkhahle, K. E. Sekhosana, S. Centane, T. Nyokong, Electrocatalytic activity of asymmetrical cobalt phthalocyanines in the presence of N doped graphene quantum dots: The push-pull effects of substituents, Electroanalysis 31 (**2019**) 891–904.
100. N. Ndebele, P. Şen, T. Nyokong, Electrochemical detection of dopamine using phthalocyanine-nitrogen-doped graphene quantum dot conjugates, J. Electroanal. Chem. 886 (**2021**) 115111.
101. S. R. Nxele, D. O. Oluwole, T. Nyokong, Electrocatalytic activity of a push pull Co(II) phthalocyanine in the presence of graphitic carbon nitride quantum dots, Electrochim. Acta 326 (**2019**) 134978.
102. S. R. Nxele, T. Nyokong, The electrochemical detection of prostate specific antigen on glassy carbon electrode modified with combinations of graphene quantum dots, cobalt phthalocyanine and an aptamer, J. Inorg. Biochem. 221 (**2021**) 111462.
103. S. Centane, T. Nyokong, Co phthalocyanine mediated electrochemical detection of the HER2 in the presence of Au and CeO_2 nanoparticles and graphene quantum dots, Bioelectrochemistry 149 (**2023**) 108301.

104. K. H. Koh, S. H. Noh, T.-H. Kim, W. J. Lee, S.-C. Yi, T. H. Han, A graphene quantum dot/phthalocyanine conjugate: a synergistic catalyst for the oxygen reduction reaction, RSC Adv. 7 (**2017**) 26113–26119.

105. M. Ahn, M.-J. Kim, D. W. Cho, K.-R. Wee, Electron push–pull effects on intramolecular charge transfer in perylene-based donor–acceptor compounds, J. Org. Chem. 86 (**2021**) 403–413.

106. B. Ghazal, K. Azizi, E. F. Ewies, A. S. A. Youssef, V. M. Mwalukuku, R. Demadrille, T. Torres, S. Makhseed, Push–pull zinc phthalocyanine bearing hexa-tertiary substituted carbazolyl donor groups for dye-sensitized solar cells, Molecules 25 (**2020**) 1692.

107. E. M. Maya, C. García, E. M. García-Frutos, P. Vázquez, P. Vázquez, T. Torres, Synthesis of novel push−pull unsymmetrically substituted alkynyl phthalocyanines, J. Org. Chem. 65 (**2000**) 2733–2739.

108. C. S. J. N. O’ Donoghue, M. Shumba, T. Nyokong, Electrode modification through click chemistry using Ni and Co alkyne phthalocyanines for electrocatalytic detection of hydrazine, Electroanalysis 29 (**2017**) 1731–1740.

109. Y. İpek, H. Dinçer, A. Koca, Electrode modification based on “click electrochemistry” between terminal-alkynyl substituted cobalt phthalocyanine and 4-azidoaniline, Sens. Actuators B Chem. 193 (**2014**) 830–837.

110. B. Öztaş, D. Akyüz, A. Koca, Immobilization of alkynyl functionalized manganese phthalocyanine via click electrochemistry for electrocatalytic oxygen evolution reaction, Phys. Chem. Chem. Phys. 19 (**2017**) 26121–26131.

111. D. Akyüz, H. Dinçer, A. R. Özkaya, A. Koca, Electrocatalytic hydrogen evolution reaction with metallophthalocyanines modified with click electrochemistry, Int. J. Hydrog. Energy 40 (**2015**) 3019–3027.

112. G. Fomo, N. Nwaji, T. Nyokong, Low symmetric metallophthalocyanine modified electrode via click chemistry for simultaneous detection of heavy metals, J. Electroanal. Chem. 813 (**2018**) 58–66.

113. D. Mwanza. S. Mvango, S. Khene, T. Nyokong, P. Mashazi, Exploiting click chemistry for the covalent immobilization of tetra (4-propargyloxyphenoxy) metallophthalocyanines onto phenylazide-grafted gold surfaces, Electrochim. Acta 254 (**2017**) 89–100.

114. E. Dube, N. Nwaji, J. Mack, T. Nyokong, The photophysicochemical behavior of symmetric and asymmetric zinc phthalocyanines, surface assembled onto gold nanotriangles, New J. Chem. 42 (**2018**) 14290–14299.
115. S. Mapukata, N. Kobayashi, M. Kimura, T. Nyokong, Asymmetrical and symmetrical zinc phthalocyanine-cobalt ferrite conjugates embedded in electrospun fibers for dual photocatalytic degradation of azo dyes: Methyl Orange and Orange G, J. Photochem. Photobiol. A 379 (**2019**) 112–122.
116. G. Zanotti, P. Imperatori, A. M. Paoletti, G. Pennesi, Sustainable approaches to the synthesis of metallophthalocyanines in solution, Molecules 26 (**2021**) 1760.
117. Agency for Toxic Substances and Disease Registry (ATSDR). **1997**. *Toxicological profile for hydrazines*. Atlanta, GA: U.S. Department of Health and Human Services, Public Health Service.
118. J. E. Troyan, Properties, production, and uses of hydrazine, Ind. Eng. Chem. 45 (**1953**) 2608–2612.
119. D. A. Venegas-Yazigi, G. I. Cárdenas-Jirón, J. H. Zagal, Theoretical study of the electron transfer reaction of hydrazine with cobalt(II) phthalocyanine and substituted cobalt(II) phthalocyanines, J. Coord. Chem. 56 (**2003**) 1269–1275.
120. V. Mani, A. T. E. Vilian, S. Chen, Graphene oxide dispersed carbon nanotube and iron phthalocyanine composite modified electrode for the electrocatalytic determination of hydrazine, Int. J. Electrochem. 7 (**2012**) 12774–12785.
121. K. I. Ozoemena, Anodic oxidation and amperometric sensing of hydrazine at a glassy carbon electrode modified with cobalt (II) phthalocyanine–cobalt (II) tetraphenylporphyrin (CoPc-$(CoTPP)_4$) supramolecular complex, Sensors 6 (**2006**) 874–891.
122. C. Q. Sun, Y. P. Sun, X. Zhang, X. Y. Zhang, D. Jiang, Q. Gao, H. Xu, J. Shen, Fabrication of a multilayer film containing cobalt phthalocyanine on the surface of a gold electrode based on electrostatic interaction and its application as an amperometric sensor of hydrazine, Thin Solid Films 288 (**1996**) 291–295.
123. S. Tajik, H. Beitollahi, S. Z. Mohammadi, M. Azimzadeh, K. Zhang, Q. Van Le, Y. Yamauchi, H. W. Jang, M. Shokouhimehr, Recent developments in electrochemical sensors for detecting hydrazine with different modified electrodes, RSC Adv. 10 (**2020**) 30481–30498.

124. V. Mani, S. T. Huang, R. Devasenathipathy, T. C. K. Yang, Electropolymerization of cobalt tetraamino-phthalocyanine at reduced graphene oxide for electrochemical determination of cysteine and hydrazine, RSC Adv. 6 (**2016**) 38463–38469.

125. D. I. Prangnell, T. M. Samocha, N. Staresinic, *Water*. In: T. M. Samocha (Ed.) Sustainable Biofloc Systems for Marine Shrimp. Oxford: Academic Press, **2019**, pp. 37–58.

126. R. Iyengar, D. J. Stuehr, M. A. Marletta, Macrophage synthesis of nitrite, nitrate, and N-nitrosamines: Precursors and role of the respiratory burst, Proc. Nati. Acad. Sci. USA 84 (**1987**) 6369–6373.

127. A. R. Butler, M. Feelisch, Therapeutic uses of inorganic nitrite and nitrate, Circulation 117 (**2008**) 2151–2159.

128. K.-O. Honikkel, The use and control of nitrate and nitrite for the processing of meat products, Meat Sci. 78 (**2008**) 68–76.

129. A. A. Saeed, B. Singh, M. N. Abbas, Y. M. Issa, E. Demsey, Electrocatalytic nitrite determination using iron phthalocyanine modified gold nanoparticles, Electroanalysis 27 (**2015**) 1086–1096.

130. A. L. Sousa, W. J. R. Santos, R. C. S. Luz, F. S. Damos, L. T. Kubota, A. A. Tanaka, S. M. C. N. Tanaka, Amperometric sensor for nitrite based on copper tetrasulphonated phthalocyanine immobilized with poly-L-lysine film, Talanta 75 (**2008**) 333–338.

131. B. S. Jilani, M. Nayaka, P. Malathesh, C. D. Mruthyunjayachar, K. R. V. Reddy, Cobalt (II) tetra methyl-quinoline oxy bridged phthalocyanine carbon nano particles modified glassy carbon electrode for sensing nitrite: A voltammetric study, Mater. Chem. Phys. 239 (**2020**) 121920.

132. Y. Wu, C. Li, Z. Dou, L. Cui, D. Liu, X. He, A novel nitrite sensor fabricated through anchoring nickel-tetrahydroxy-phthalocyanine and polyethylene oxide film onto glassy carbon electrode by a two-step covalent modification approach, J. Solid State Electrochem. 18 (**2014**) 2625–2635.

133. O. J. Achadu, T. Nyokong, Interaction of graphene quantum dots with 4- acetamido-2,2,6,6-tetramethylpiperidine-oxyl free radicals: A spectroscopic and fluorimetric study, J. Fluoresc. 26 (**2016**) 283–295.

134. G. G. Matlou, N. Kobayashi, M. Kimura, T. Nyokong, Synthesis and photophysical studies of asymmetric zinc phthalocyanine–magnetic nanoparticle conjugates, New J. Chem. 41 (**2017**) 12309–12318.

135. Y. Chen, A. Q. Dayo, H. Zhang, A Wang, J. Wang, W. Liu, Y. Yang, Q. Qin, Y. Yang, Synthesis of cardanol-based phthalonitrile monomer and its copolymerization with phenol–aniline-based benzoxazine, J. Appl. Polym. Sci. 136 (**2019**) 47505.
136. D. O. Oluwole, E. Prinsloo, T. Nyokong, Photophysicochemical properties of nanoconjugates of zinc(II) 2(3)-mono-2-(4-oxy)phenoxy)acetic acid phthalocyanine with cysteamine capped silver and silver–gold nanoparticles, Polyhedron 119 (**2016**) 434–444.
137. E. Dube, N. Nwaji, D. O. Oluwole, J. Mack, T. Nyokong, Investigation of photophysicochemical properties of zinc phthalocyanines conjugated to metallic nanoparticles, J. Photochem. Photobiol. A 349 (**2017**) 148–161.
138. N. Rapulenyane, E. Antunes, N. Masilela, T. Nyokong, Synthesis and photophysicochemical properties of novel zinc phthalocyanines mono substituted with carboxyl containing functional groups, J. Photochem. Photobiol. A 250 (**2012**) 18–24.
139. H. Kliesch, A. Weitemeyer, S. Müller, D. Wöhrle, Synthesis of phthalocyanines with one sulfonic acid, carboxylic acid, or amino group, Eur. J. Org. Chem. 1995 (**1995**) 1269–1273.
140. D. Quinton, E. Antunes, S. Griveau, T. Nyokong, F. Bedioui, Cyclic voltammetry and spectroelectrochemistry of a novel manganese phthalocyanine substituted with hexynyl groups, Inorg. Chem. Commun. 14 (**2011**) 330–332.
141. M. S. Ağirtas, M. S. Izgi, Synthesis and characterization of new metallophthalocyanines with four phenoxyacetamide units, J. Mol. Struct. 927 (**2009**) 126–128.
142. S. D’ Souza, E. Antunes, C. Litwinski, T. Nyokong, Photophysical behavior of zinc monoaminophthalocyanines linked to mercaptopropionic acid-capped CdTe quantum dots, J. Photochem. Photobiol. A 220 (**2011**) 11–19.
143. Gaussian 09, Revision E.01, M. J. Frisch, G. W. Trucks, H. B. Schlegel, G. E. Scuseria, M. A. Robb, J. R. Cheeseman, G. Scalmani, V. Barone, B. Mennucci, G. A. Petersson, *et al.*, Gaussian, Inc., Wallingford CT, 2013.
144. O. J. Achadu, I. Uddin, T. Nyokong, Fluorescence behavior of nanoconjugates of graphene quantum dots and zinc phthalocyanines, J. Photochem. Photobiol. A 317 (**2016**) 12–25.

145. L. S. Mpeta, G. Fomo, T. Nyokong, Click chemistry electrode modification using 4-ethynylbenzyl substituted cobalt phthalocyanine for applications in electrocatalysis, J. Coord. Chem. 71 (**2018**) 1623–1638.
146. S. Altun, Z. Odabaş, A. Altındal, A. R. Özkaya, Coumarin-substituted manganese phthalocyanines: synthesis, characterization, photovoltaic behaviour, spectral and electrochemical properties, Dalton Trans. 43 (**2014**) 7987–7997.
147. J. Rusanova, M. Pilkington, S. Decurtins, A novel fully conjugated phenanthroline-appended phthalocyanine: synthesis and characterisation, Chem. Commun. 19 (**2002**) 2236–2237.
148. L. Jin, Y. Wang, F. Yan, J. Zhang, F. Zhong, The synthesis and application of nitrogen-doped graphene quantum dots on brilliant blue detection, J. Nanomater. 2019 (**2019**) 1471728.
149. Z. D. Liu, H. X. Zhao, C. Z. Huang, Obstruction of photoinduced electron transfer from excited porphyrin to graphene oxide: A fluorescence turn-on sensing platform for iron (III) ions, PLoS One 7 (**2012**) e50367.
150. L. Shi, B. Hernandez, M. Selke, Singlet oxygen generation from water-soluble quantum dot organic dye nanocomposites, J. Am. Chem. Soc. 128 (**2006**) 6278–6279.
151. L. Li, J.F. Zhao, N. Won, H. Jin, S. Kim, J. Y. Chen, Quantum dot-aluminium phthalocyanine Conjugates perform photodynamic reactions to kill cancer cells via fluorescence resonance energy transfer (FRET), Nanoscale Res. Lett. 7 (**2012**) 386–393.
152. B. Shi, Y. Su, Y. Duan, S. Chen, W. Zuo, A nanocomposite prepared from copper(II) and nitrogen-doped graphene quantum dots with peroxidase mimicking properties for chemiluminescent determination of uric acid, Microchim. Acta 186 (**2019**) 397.
153. O. Bajjou, M. Khenfouch, M. Baïtoul, B. Mothudi, M. Dhlamini, E. Faulques, M. Maaza, Vibrational and optical properties of meso-tetrakis(4-phenylsulfonica-acid) porphyrin decorated with graphene oxide, Mater. Sci. Eng. 186 (**2017**) 012003.
154. O. Frank, M. Bouša, I. Riaz, R. Jalil, K. S. Novoselov, G. Tsoukleri, J. Parthenios, L. Kavan, K. Papagelis, C. Galiotis, Phonon and structural changes in deformed bernal stacked bilayer graphene, Nano Lett. 12 (**2012**) 687–693.
155. T. Souza, V. Ciminelli, N. Mohallem, A comparison of TEM and DLS methods to characterize size distribution of ceramic nanoparticles, J. Phys. Conf. Ser. 733 (**2016**) 12039–12044.

156. M. Winey, J. B. Meehl, E. T. O'Toole, T. H. Giddings, Jr., Conventional transmission electron microscopy, Mol. Biol. Cell. 25 (**2014**) 319–323.

157. Y.-H. Deng, Sublimable materials facilitate the TEM sample preparation of oil-soluble nanomaterials, Appl. microsc. 50 (**2020**) 21.

158. N. Nwahara, J. Britton, T. Nyokong, Improving singlet oxygen generating abilities of phthalocyanines: Aluminum tetrasulfonated phthalocyanine in the presence of graphene quantum dots and folic acid, J. Coord. Chem. 70 (**2017**) 1601–1616.

159. L. C. Nene, M. Managa, T. Nyokong, Photo-physicochemical properties and in vitro photodynamic therapy activity of morpholine-substituted zinc(II)-phthalocyanines π-π stacked on biotinylated graphene quantum dots, Dyes Pigm. 165 (**2019**) 488–498.

160. F. J. Rawson, A, J. Downard, K. H. Baronian, Electrochemical detection of intracellular and cell membrane redox systems in Saccharomyces cerevisiae**,** Sci. Rep. 4 (**2014**) 5216–5224.

161. R. L. McCreery, Advanced carbon electrode materials for molecular electrochemistry, Chem. Rev. 108 (**2008**) 2646–2687.

162. J. D. Schrattenecker, R. Heer, E. Melnik, T. Maier, G. Fafilek, R. Hainberger, Hexaammineruthenium (II)/(III) as alternative redox-probe to hexacyanoferrate (II)/(III) for stable impedimetric biosensing with gold electrodes, Biosens. Bioelectron. 127 (**2019**) 25–30.

163. J. E. Hein, V. V. Fokin, Copper-catalyzed azide–alkyne cycloaddition (CuAAC) and beyond: new reactivity of copper(I) acetylides, Chem. Soc. Rev. 39 (**2010**) 1302–1315.

164. N. Aristov, A. Habekost, Cyclic voltammetry - A versatile electrochemical method investigating electron transfer processes, World J. Chem. Educ. 3 (**2015**) 115–119.

165. N. Elgrishi, K. J. Rountree, B. D. McCarthy, E. S. Rountree, T. T. Eisenhart, J. L. Dempsey, A practical beginner's guide to cyclic voltammetry, J. Chem. Educ. 95 (**2018**) 197–206.

166. C. P. Canales, *Electrochemical Impedance Spectroscopy and Its Applications*. In: P. V. Pham (Ed.) 21st Century Nanostructured Materials. London, United Kingdom, IntechOpen, **2021** [Online]. Available from: https://www.intechopen.com/chapters/79697 (Accessed: 26 December 2022).

167. N. I. Ramli, N. A. B. Ismail, F. Abd-Wahab, W. W. A. Salim, *Cyclic Voltammetry and Electrical Impedance Spectroscopy of Electrodes Modified with PEDOT:PSS-Reduced Graphene Oxide Composite*. In: K. Pal (Ed.) Transparent Conducting Films. London,

United Kingdom, IntechOpen **2018** [Online]. Available from: https://www.intechopen.com/chapters/63257 (Accessed: 26 December 2022).

168. V. Horvat-Radošević, K. Kvastek, D. Križekar, Kinetics of the $[Fe(CN)_6]^{3-}/[Fe(CN)_6]^{4-}$ redox couple reaction on anodically passivated $Fe_{80}B_{20}$, CCACAA 70 (**1997**) 537–561.
169. H. A. Ishkhanyan, V. P. Krainov, One-dimensional Hubbard-Luttinger model for carbon nanotubes, Phys. Scr. 90 (**2015**) 074043.
170. A. J. Clancy, M. K. Bayazit, S. A. Hodge, N. T. Skipper, C. A. Howard, M. S. P. Shaffer, Charged carbon nanomaterials: Redox chemistries of fullerenes, carbon nanotubes, and graphenes, Chem. Rev. 118 (**2018**) 7363–7408.
171. Z. Zheng, Q. Yu, Z. Chen, W. Zhu, Q. Hu, Y. Liu, L. Gui, Y. Song, Investigation of localized electrochemical reactivity on a β-PbO_2 electrode using scanning electrochemical microscopy, J. Electroanal. Chem. 878 (**2020**) 114699.
172. A. L. Whitworth, D. Mandler, P. R. Unwin, Theory of scanning electrochemical microscopy (SECM) as a probe of surface conductivity, Phys. Chem. Chem. Phys. 7 (**2005**) 356–365.
173. C. A. Caro, F. Bedioui, J. H. Zagal, Electrocatalytic oxidation of nitrite on a vitreous carbon electrode modified with cobalt phthalocyanine, Electrochim. Acta 47 (**2002**) 1489–1494.
174. A. H. Suroviec, Determining surface coverage of self-assembled monolayers on gold electrodes, Chem. Educator 17 (**2012**) 83–85.
175. J. Gooding, V. Praig, E. Hall, Platinum-catalyzed enzyme electrodes immobilized on gold using self-assembled layers, Anal. Chem. 70 (**1998**) 2396–2402.

176. S. Khene, K. Lobb, T. Nyokong, Characterization of nickel tetrahydroxy phthalocyanine complexes and the electrocatalytic oxidation of 4-chlorophenol: Correlation of theory with experiments, Electrochim. Acta 362 (**2009**) 5055–5063.
177. Z. Li, M. Lieberman, W. Hill, XPS and SERS study of silicon phthalocyanine monolayers: Umbrella vs octopus design strategies for formation of oriented SAMs, Langmuir 17 (**2001**) 4887–4894.

178. M. P. Siswana, K. I. Ozoemena, T. Nyokong, Electrocatalysis of asulam on cobalt phthalocyanine modified multi-walled carbon nanotubes immobilized on a basal plane pyrolytic graphite electrode, Electrochim. Acta 42 (**2006**) 114–122.

179. F. Bedioui, S. Trevin, V. Albin, M. Guadalupe, G. Villegas, J. Devynck, Design and characterization of chemically modified electrodes with iron(III) porphyrinic-based polymers: Study of their reactivity toward nitrites and nitric oxide in aqueous solution, Anal. Chim. Acta 341 (**1997**) 177–185.
180. A. Fujimoto, Y. Yamada, A. Koinuma, S. Satoshi, Origins of sp^3 C peaks in C_{1s} X-ray photoelectron spectra of carbon materials, Anal. Chem. 88 (**2016**) 6110–6114.
181. R. J. J. Jansen, H. van Bekkum, XPS of nitrogen-containing functional groups on activated carbon, Carbon 33 (**1995**) 1021–1027.
182. E. V. Basiuk, L. V. Huerta, V. A. Basiuk, Noncovalent bonding of 3d metal(II) phthalocyanines with single-walled carbon nanotubes: A combined DFT and XPS study, Appl. Surf. Sci. 470 (**2019**) 622–630.
183. P. Fortgang, T. Tite, V. Barnier, N. Zehani, C. Maddi, F. Lagarde, A.-S. Loir, N. Jaffrezic-Renault, C. Donnet, F. Garrelie, C. Chaix, Robust electrografting on self-organized 3D graphene electrodes, ACS Appl. Mater. Interfaces 8 (**2016**) 1424–1433.
184. S. Tardio, P. J. Cumpson, Practical estimation of XPS binding energies using widely available quantum chemistry software, Surf. Interface Anal. 50 (**2018**) 5–12.
185. T. Nyokong, *Electronic Spectral and Electrochemical Behavior of Near Infrared Absorbing Metallophthalocyanines*. In: J. Jiang (Ed.) Functional Phthalocyanine Molecular Materials. Structure and Bonding. Berlin, Heidelberg: Springer, **2010**, pp. 45–87.
186. D. A. Geraldo, C. A. Togo, J. Limson, T. Nyokong, Electrooxidation of hydrazine catalyzed by noncovalently functionalized single-walled carbon nanotubes with CoPc, Electrochim. Acta 53 (**2008**) 8051–8057.
187. V. Sinka, D. A. Cruz, J. M. López-Soria, V. S. Martín, P. O. Miranda, J. I. Padrón, *Synthesis of Heterocycles With Iron Salts as Sustainable Metal Catalysts.* In: D. Solé and I. Fernández (Eds.) Advances in Transition-Metal Mediated Heterocyclic Synthesis. London: Elsevier, **2018**, pp. 193–229.
188. W. J. Albery, Electrode kinetics, Phil. Trans. R. Soc. Lond. A 302 (**1981**) 221–235.
189. S. Trasatti, *Reaction Mechanism and Rate Determining Steps.* In: W. Vielstich, A. Lamm, H. A. Gasteiger and H. Yokokawa (Eds.) Handbook of fuel cells. United Kingdom: John Wiley and Sons, Ltd. **2010**, pp. 1–9.

190. N. Pal, N. Saxena, A. Mandal, Equilibrium and dynamic adsorption of gemini surfactants with different spacer lengths at oil/aqueous interfaces, Colloids Surf. A: Physicochem. Eng. Asp. 533 (**2017**) 20–32.
191. S. Karim Hassaninejad-Darzi, F. Shajie, A sensitive voltammetric determination of anti-parkinson drug pramipexole using titanium dioxide nanoparticles modified carbon paste electrode, J. Braz. Chem. Soc. 28 (**2017**) 529–539.
192. S. N. Azizi, S. Ghasemi, E. Chiani, Nickel/mesoporous silica (SBA-15) modified electrode: An effective porous material for electrooxidation of methanol, Electrochim. Acta 88 (**2013**) 463–472.
193. L. L. Okumura, A. A. Saczk, M. F. de Oliveira, A. C. C. Fulgêncio, L. Torrezani, P. E. N. Gomes, R. M. Peixoto, Electrochemical feasibility study of methyl parathion determination on graphite-modified basal plane pyrolytic graphite electrode, J. Braz. Chem. Soc. 22 (**2011**) 652–659.
194. T. Shinagawa, A. T. Garcia-Esparza, K. Takanabe, Insight on Tafel slopes from a microkinetic analysis of aqueous electrocatalysis for energy conversion, Sci. Rep. 5 (**2015**) 13801.
195. B. Haghighi, H. Hamidi, S. Bozorgzadeh, Sensitive and selective determination of hydrazine using glassy carbon electrode modified with Pd nanoparticles decorated multiwalled carbon nanotubes, Anal. Bioanal. Chem. 398 (**2010**) 1411–1416.
196. J. Zhang in: *PEM Fuel Cell Electrocatalysts and Catalyst Layers*. London: Springer-Verlag, **2008**.
197. J. M. Zen, A. S. Kumar, M. R. Chang, Electrocatalytic oxidation and trace detection of amitrole using a nafion/lead-ruthenium oxide pyrochlore chemically modified electrode, Electrochim. Acta 45 (**2000**) 1691–1699.
198. N. Mohammadizadeh, S. Z. Mohammadi, M. Kaykhaii, Highly sensitive amperometric detection of propranolol using graphite screen printed electrode modified with zirconium dioxide nanoparticles, Anal. Bioanal. Electrochem. 9 (**2017**) 277–285.
199. A. Salimi, K. Abdi, Enhancement of the analytical properties and catalytic activity of a nickel hexacyanoferrate modified carbon ceramic electrode prepared by two-step sol–gel technique: application to amperometric detection of hydrazine and hydroxyl amine, Talanta 63 (**2004**) 475–483.

200. M. E. G. Lyons, R. L. Doyle, Oxygen evolution at oxidised iron electrodes: A tale of two slopes, Int. J. Electrochem. Sci. 7 (**2012**) 9488–9501.

201. D. Antipin, M. Risch, Calculation of the Tafel slope and reaction order of the oxygen evolution reaction between pH 12 and pH 14 for the adsorbate mechanism, Electrochem. Sci. Adv. (**2022**) e2100213.

202. D. Geraldo, C. Linares, Y.-Y. Chen, S. Ureta-Zanartu, J. H. Zagal, Volcano correlations between formal potential and Hammett parameters of substituted cobalt phthalocyanines and their activity for hydrazine electro-oxidation. Electrochem. commun. 4 (**2002**) 182–187.

203. C. W. Foster, J. Pillay, J. P. Metter, C. E. Banks, Cobalt phthalocyanine modified electrodes utilised in electroanalysis: Nano-structured modified electrodes vs. bulk modified screen-printed electrodes, Sensors 14 (**2014**) 21905–21922.

204. C. D. C. Conceição, R. C. Faria, A. A. Tanaka, Electrocatalytic oxidation and voltammetric determination of hydrazine in industrial boiler feed water using a cobalt phthalocyanine-modified electrode, Anal. Lett. 41 (**2008**) 1010–1021.

205. S. Sinha, M. S. Aaron, J. Blagojevic, J. J. Warren, Electrocatalytic dioxygen reduction by carbon electrodes noncovalently modified with iron porphyrin complexes: Enhancements from a single proton relay, Chem. Eur. J. 21 (**2015**) 18072–18075.

206. X. Gu, X. Li, S. Wu, J. Shi, G. Jiang, G. Jiang, S. Tian, A sensitive hydrazine hydrate sensor based on a mercaptomethyl-terminated trinuclear Ni(II) complex modified gold electrode, RSC Adv. 6 (**2016**) 8070–8078.

207. P. Bernard, P. Stelmachowski, P. Broś, W. Makowski, A. Kotarba, Demonstration of the influence of specific surface area on reaction rate in heterogeneous catalysis, J. Chem. Educ. 98 (**2021**) 935−940.

208. S. Talebi, A. Abedi, V. Amani, Cobalt(II) complexes with small variations in the heterocycle ligand, crystal structure and DFT calculations, J. Mol. Struct. 1230 (**2021**) 129911–129922.

209. J. Michl, Magnetic circular dichroism of aromatic molecules, Tetrahedron 25 (**1984**) 3845–3934.

210. S. Griveau, F. Bedioui, C. Adamo, The oxidation of thiols by cobalt N_4-Complexes: A correlation between theory and experiments, J. Phys. Chem. A 105 (**2001**) 11304–11311.

211. R. G. Pearson, The principle of maximum hardness, Acc. Chem. Res. 26 (**1993**) 250–255.
212. I. Ciofini, F. Bedioui, J. H. Zagal, C. Adamo, Environment effects on the oxidation of thiols: Cobalt phthalocyanine as a test case, Chem. Phys. Lett. 376 (**2003**) 690–697.
213. V. Mani, A. P. Periasamy, S. M. Chen, Highly selective amperometric nitrite sensor based on chemically reduced graphene oxide modified electrode, Electrochem. Commun. 17 (**2012**) 75–78.
214. B. Agboola, T. Nyokong, Comparative electrooxidation of nitrite by electrodeposited Co(II), Fe(II) and Mn(III) tetrakis (benzylmercapto) and tetrakis (dodecylmercapto) phthalocyanines on gold electrodes, Anal. Chim. Acta 587 (**2007**) 116–123.
215. H. Karabıyık, C. Kırılmiş, H. Karabıyık, Geometry dependence of electron donating or accepting abilities of amine groups in 4,4′-disulfanediylbis(methylene)dithiazol-2-amine: Pyramidal versus planar, J. Mol. Struct. 1141 (**2017**) 650–659.
216. V. Bernal, A. Erto, L. Giraldo, J. C. Moreno-Piraján, Effect of solution pH on the adsorption of paracetamol on chemically modified activated carbons, Molecules 22 (**2017**) 1032.
217. N. Ndebele, T. Nyokong, Electrocatalytic behaviour of chalcone Substituted Co, Cu, Mn and Ni phthalocyanines towards the detection of nitrite, J. Electroanal. Chem. 926 (**2022**) 116951.
218. J. Zhang, Z. Chen, H. Wu, F. Wu, C. He, B. Wang, Y. Wu, Z. Ren, An electrochemical bifunctional sensor for the detection of nitrite and hydrogen peroxide based on layer-by-layer multilayer films of cationic phthalocyanine cobalt (II) and carbon nanotubes, J. Mater. Chem. B 4 (**2006**) 1310–1317.
219. X. Song, L. Gao, Y. Li, L. Mao, J. Yang, A sensitive and selective electrochemical nitrite sensor based on a glassy carbon electrode modified with cobalt phthalocyanine-supported Pd nanoparticles, Anal. Methods 9 (**2017**) 3166–3171.
220. R. Abdur, L. S. S. Santos, S. B. A. Barros, L. T. Kubota, R. Landers, Y. Gushikem, Electrochemical detection of nitrite in meat and water samples using a mesoporous carbon ceramic SiO_2/C electrode modified with in situ generated manganese(II) phthalocyanine, Electroanalysis 26 (**2014**) 541–547.

221. S. Lu, H. Jia, M. Hummel, Y. Wu, K. Wang, X. Qi, Z. Gu, Two-dimensional conductive phthalocyanine-based metal–organic frameworks for electrochemical nitrite sensing, RSC Adv. 11 (**2021**) 4472–4477.

APPENDICES

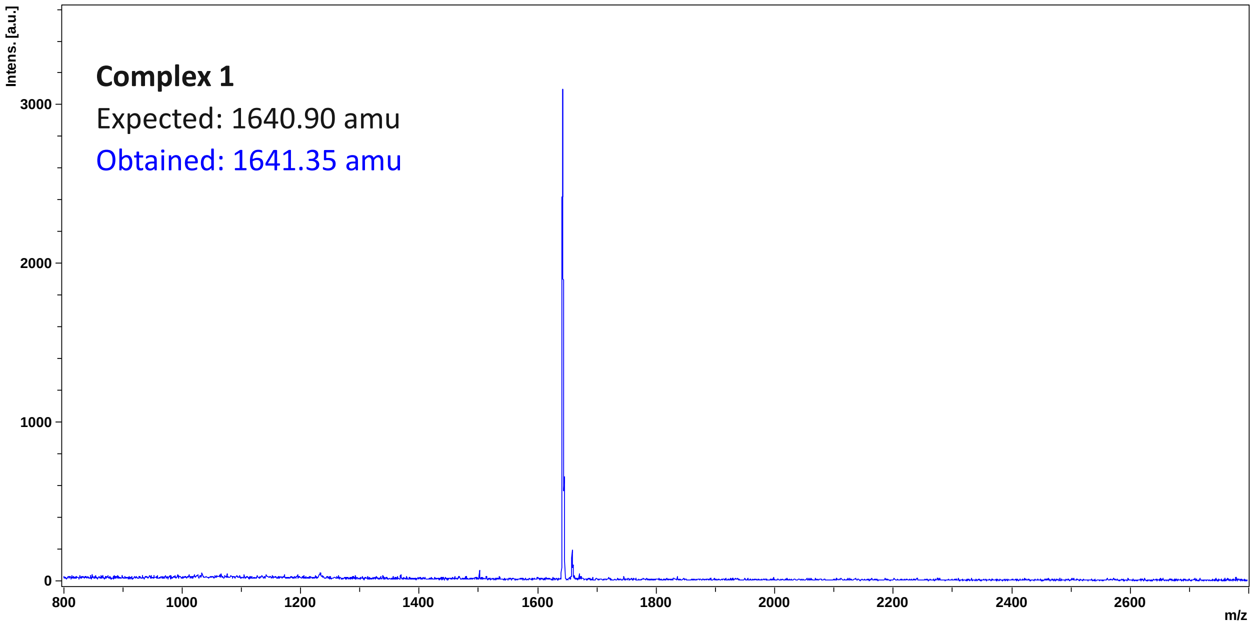

Fig. A1: Obtained mass spectral data for complex **1**.

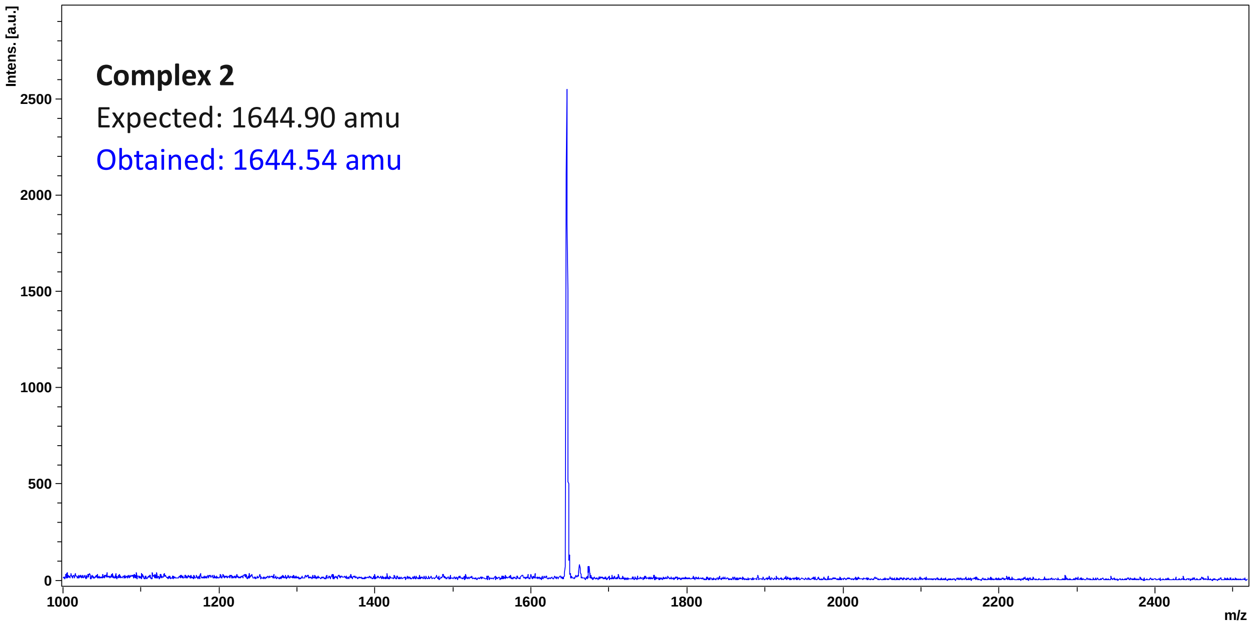

Fig. A2: Obtained mass spectral data for complex **2**.

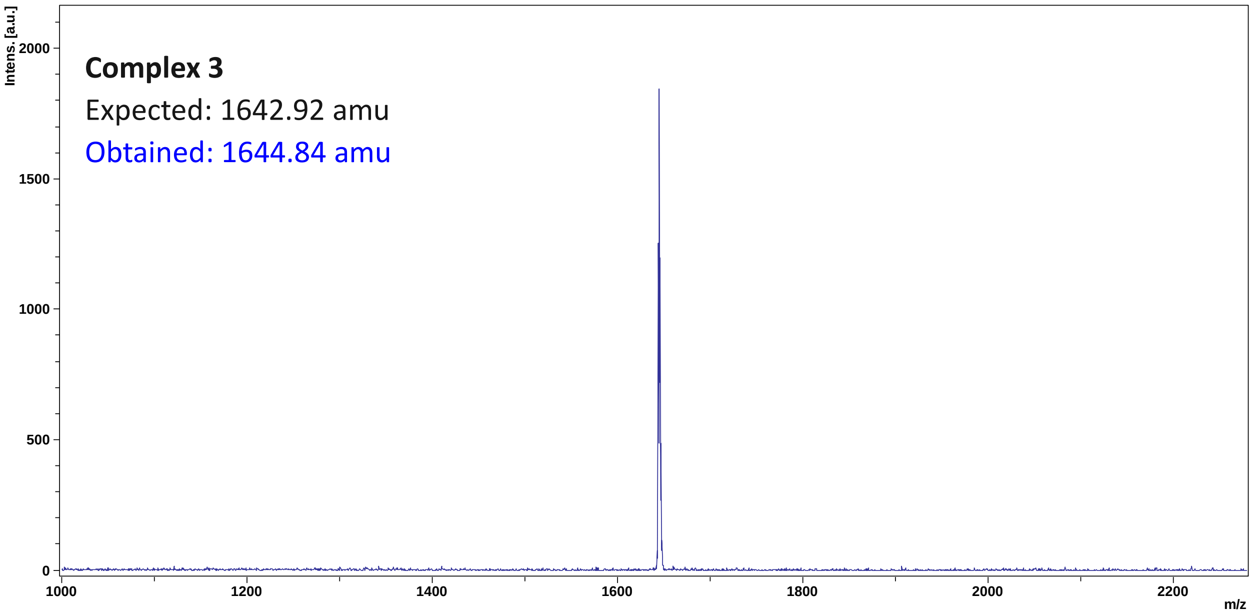

Fig. A3: Obtained mass spectral data for complex **3**.

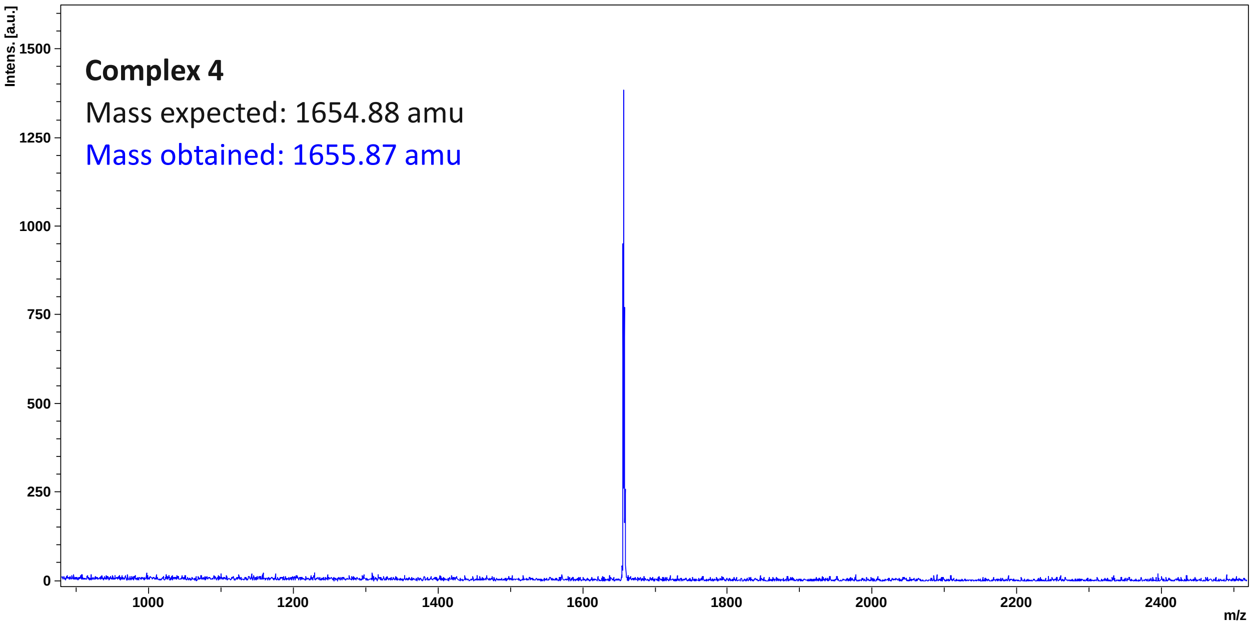

Fig. A4: Obtained mass spectral data for complex **4**.

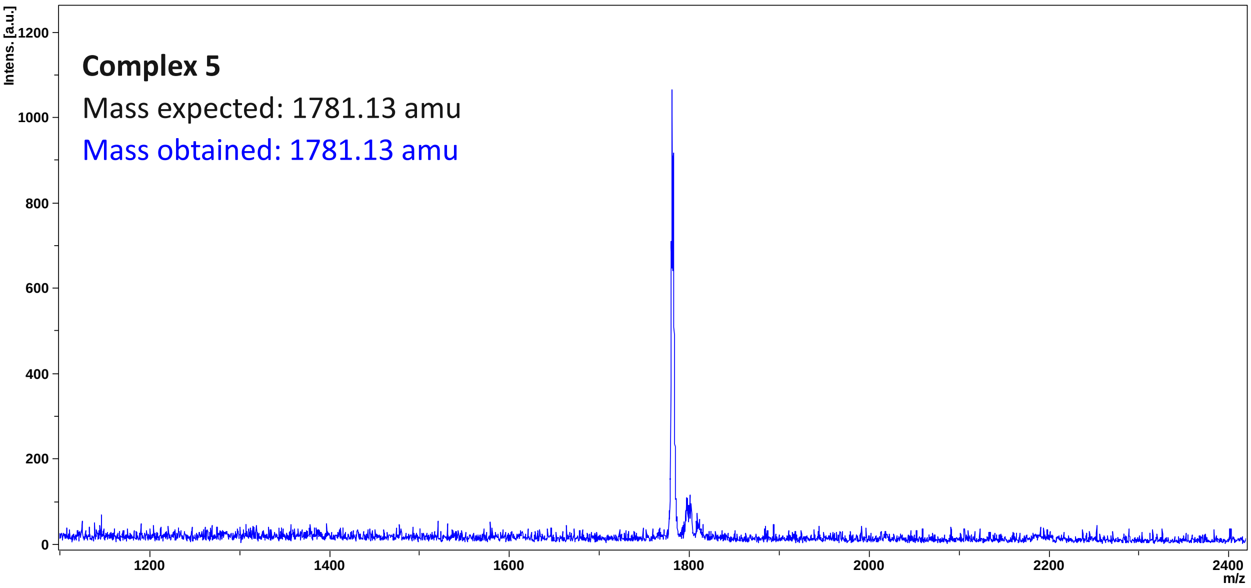

Fig. A5: Obtained mass spectral data for complex **5**.

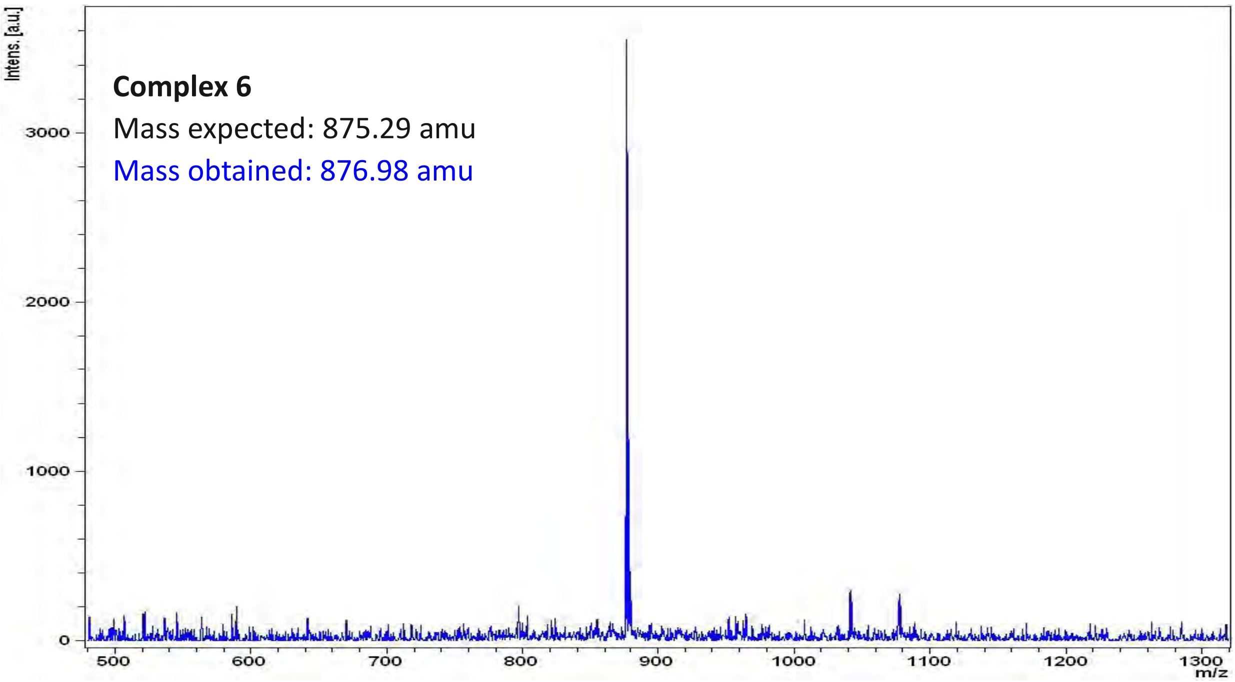

Fig. A6: Obtained mass spectral data for complex **6**.

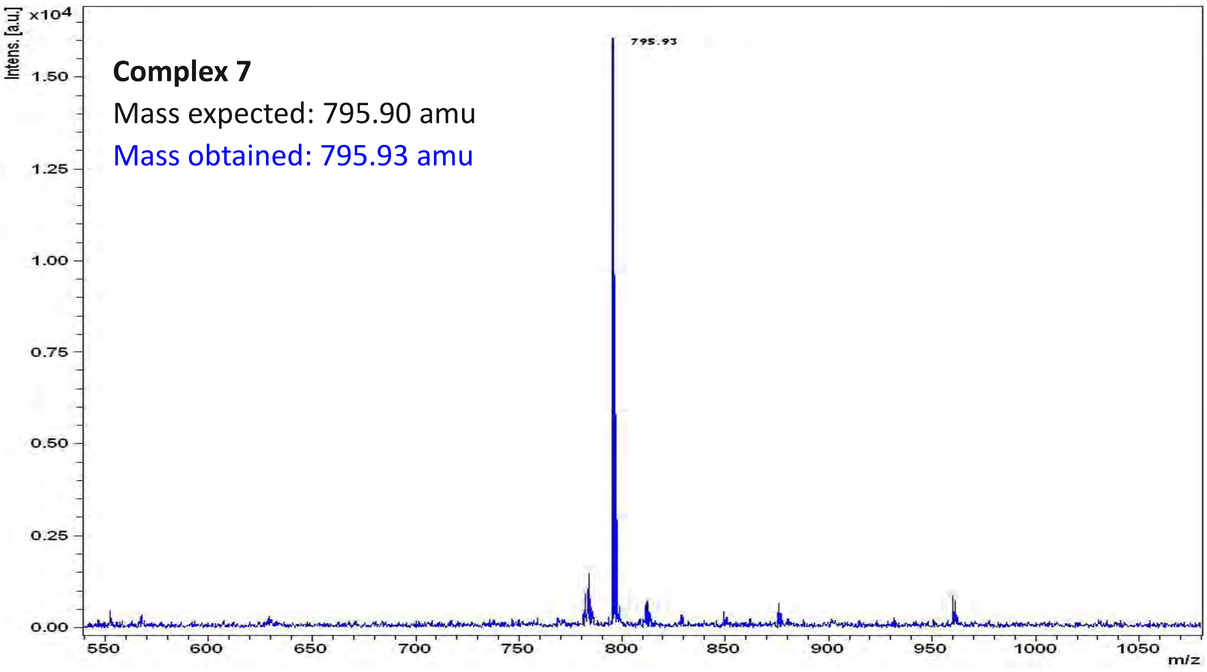

Fig. A7: Obtained mass spectral data for complex **7**.

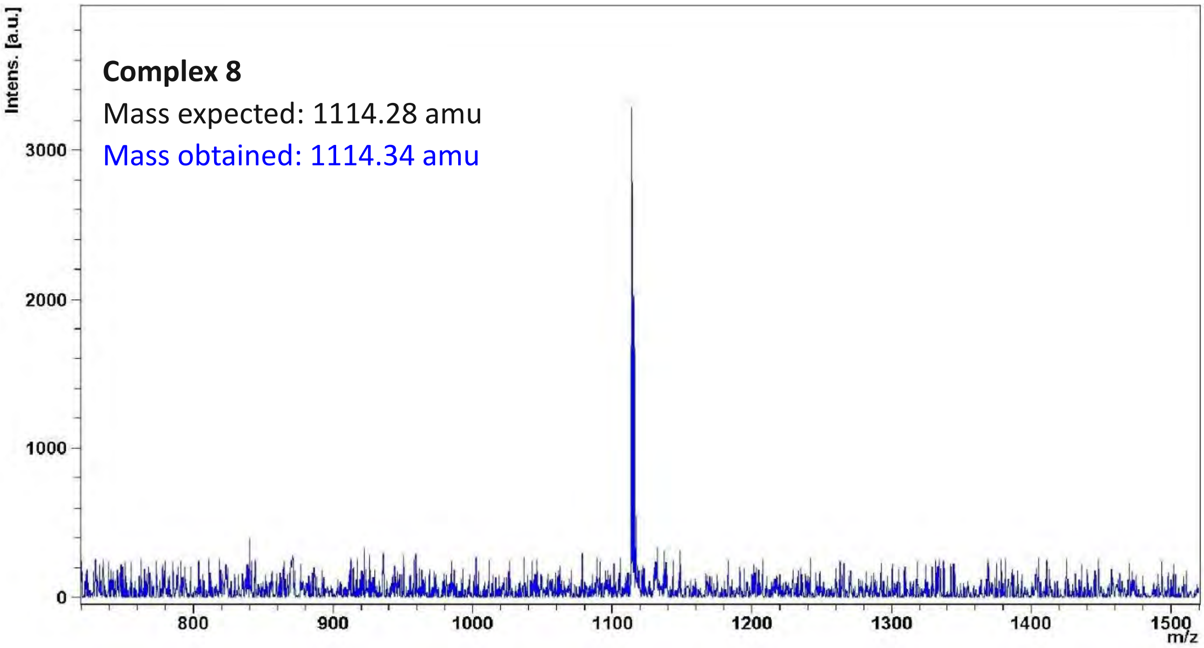

Fig. A8: Obtained mass spectral data for complex **8**.

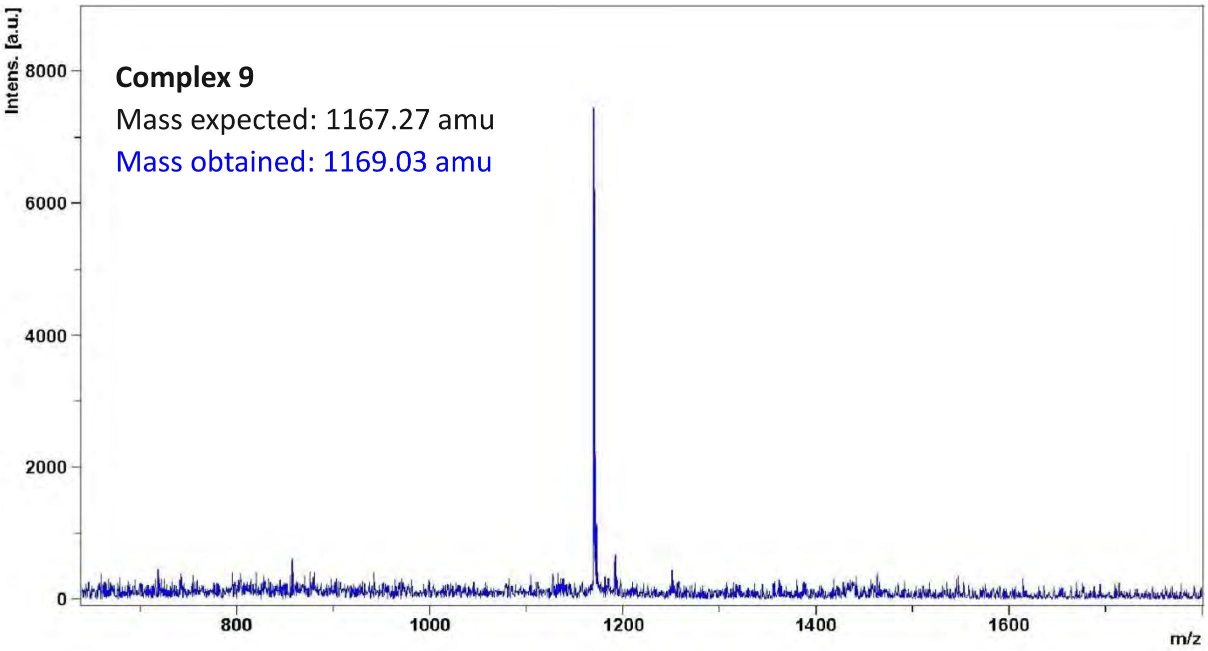

Fig. A9: Obtained mass spectral data for complex **9**.

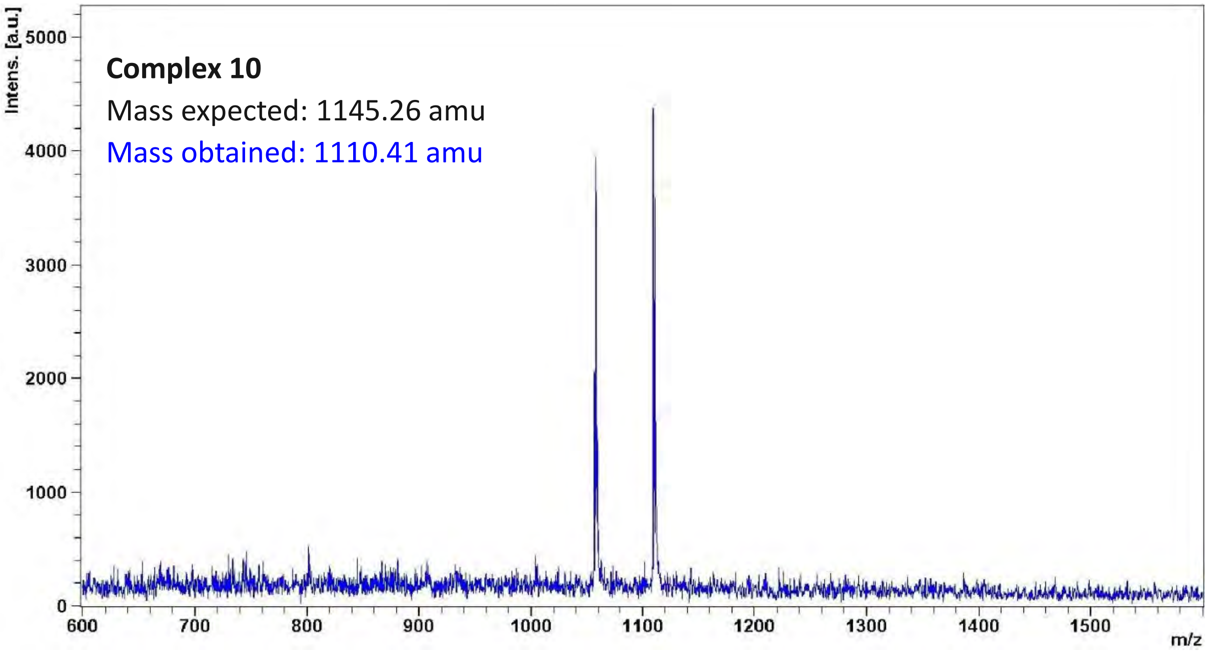

Fig. A10: Obtained mass spectral data for complex **10**.

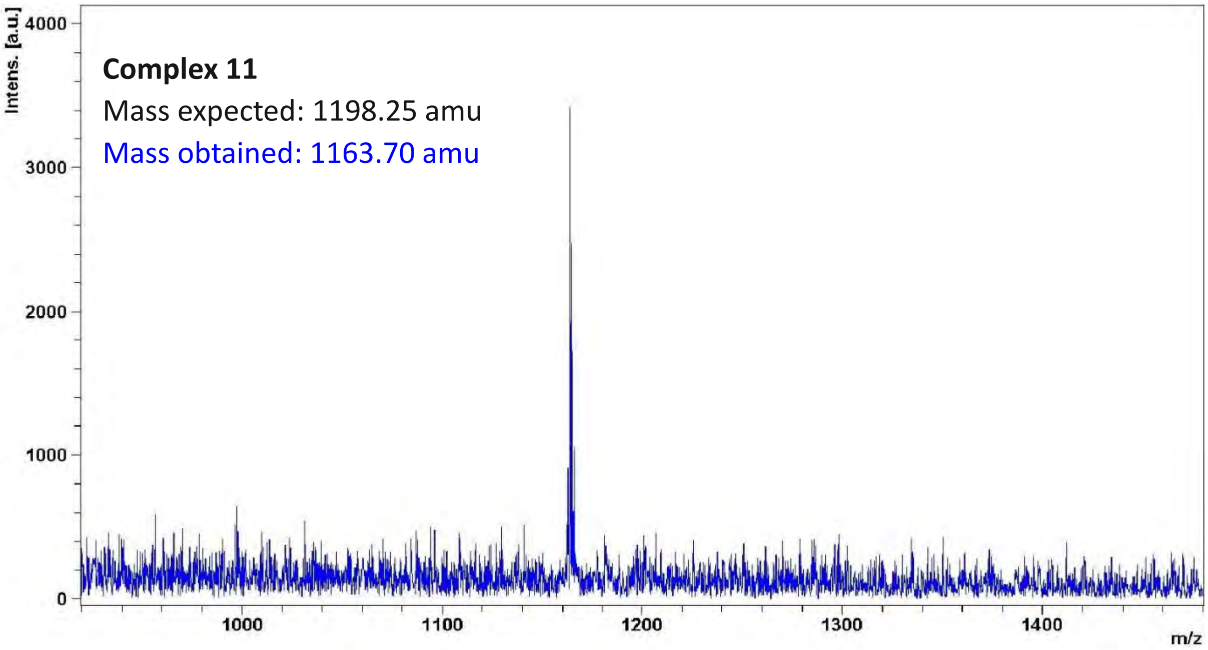

Fig. A11: Obtained mass spectral data for complex **11**.

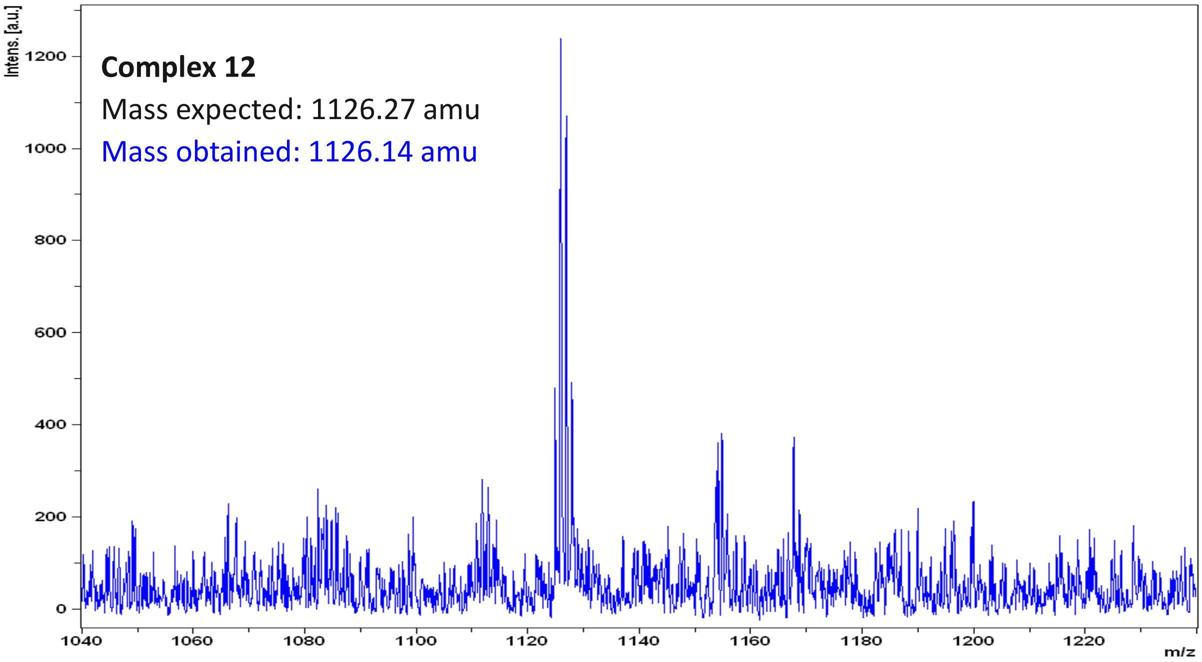

Fig. A12: Obtained mass spectral data for complex **12**.

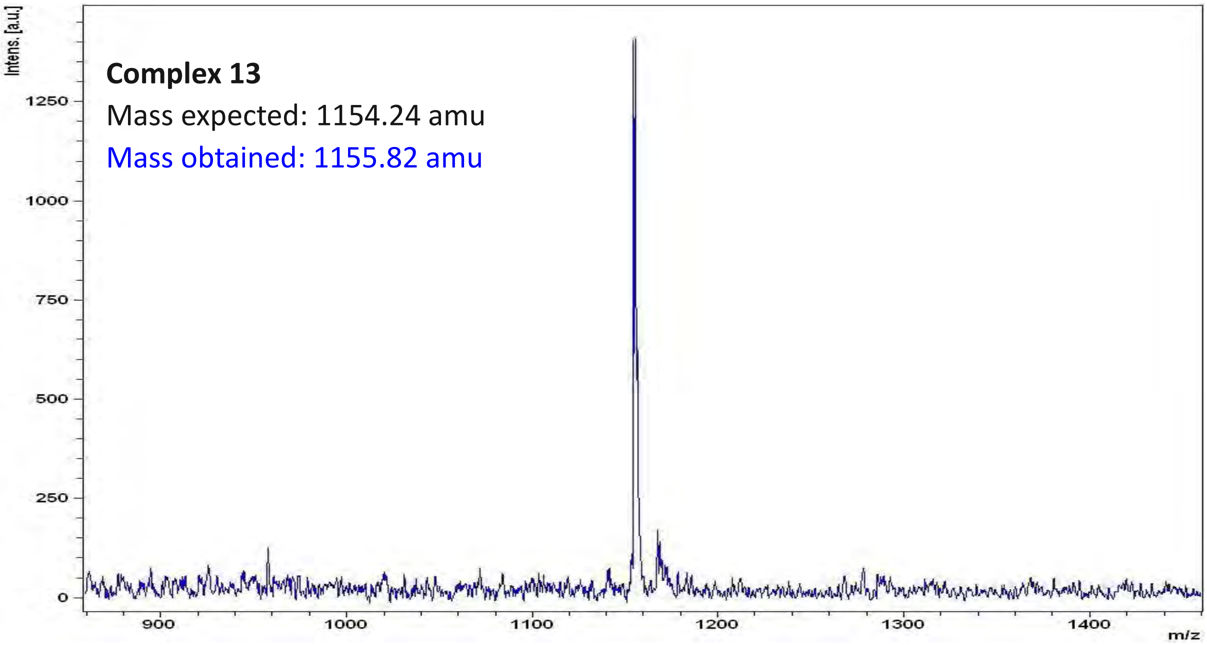

Fig. A13: Obtained mass spectral data for complex **13**.

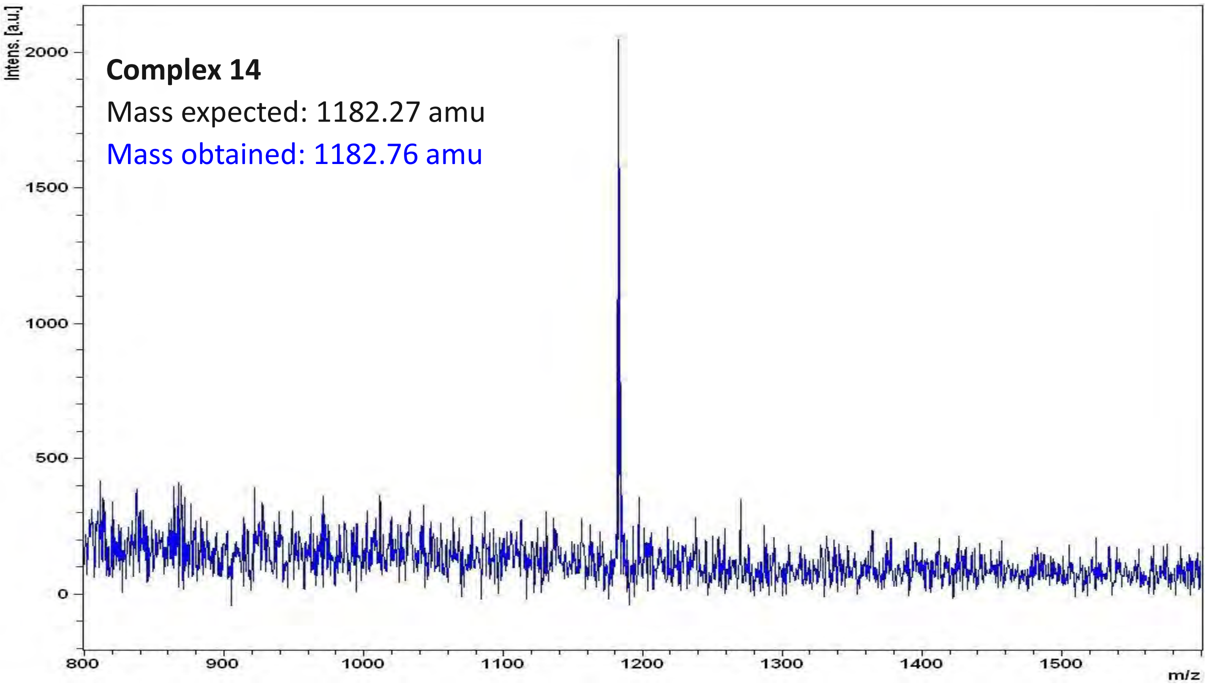

Fig. A14: Obtained mass spectral data for complex **14**.

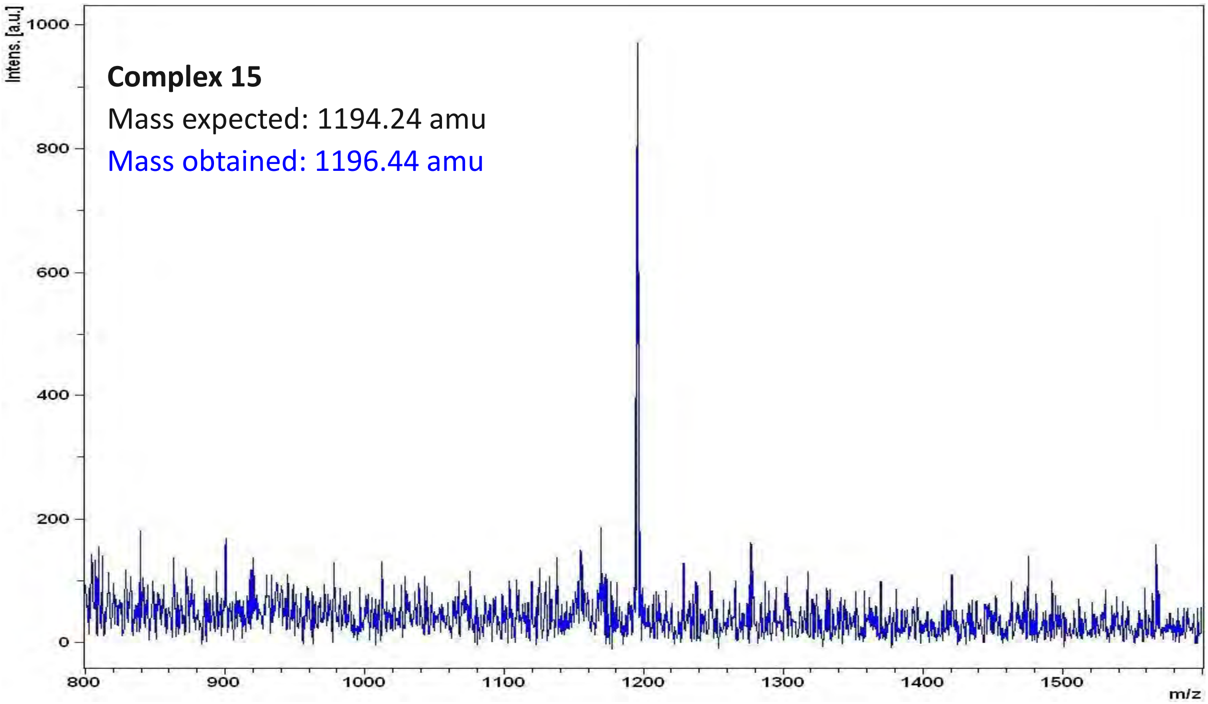

Fig. A15: Obtained mass spectral data for complex **15**.

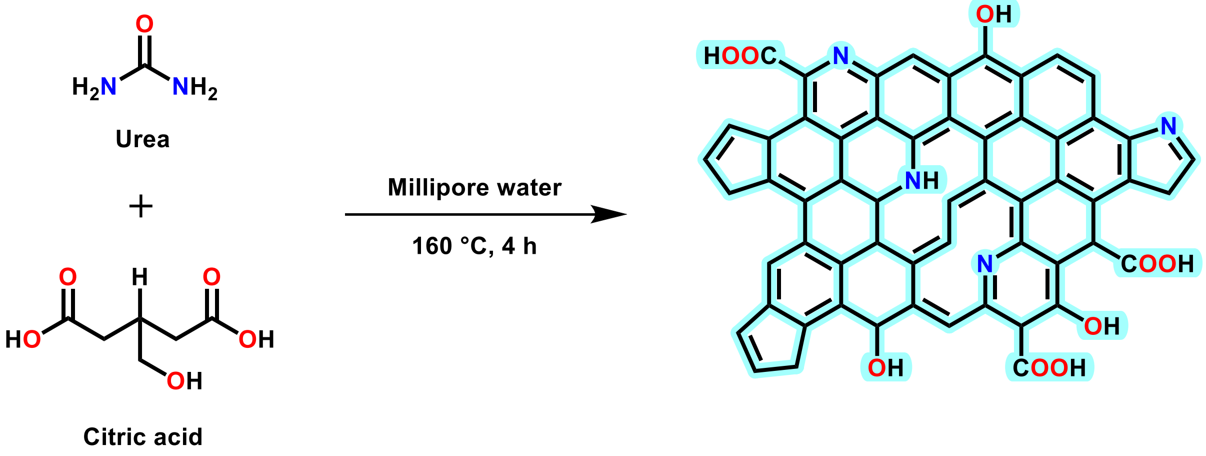

Scheme A1: An illustration of the synthetic route undertaken in the synthesis of the NGQDs.

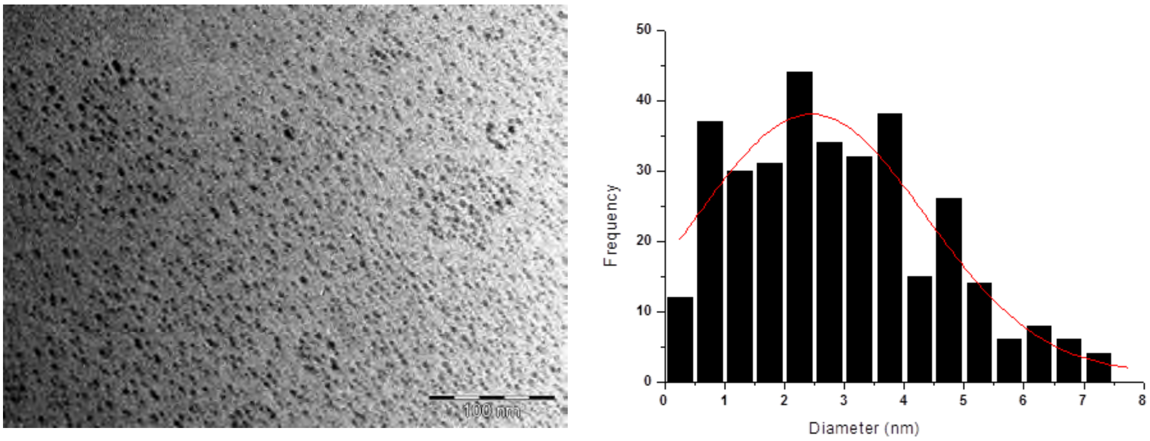

Fig. A16: TEM image of the synthesized NGQDs with a histogram demonstrating the average particle size distribution.

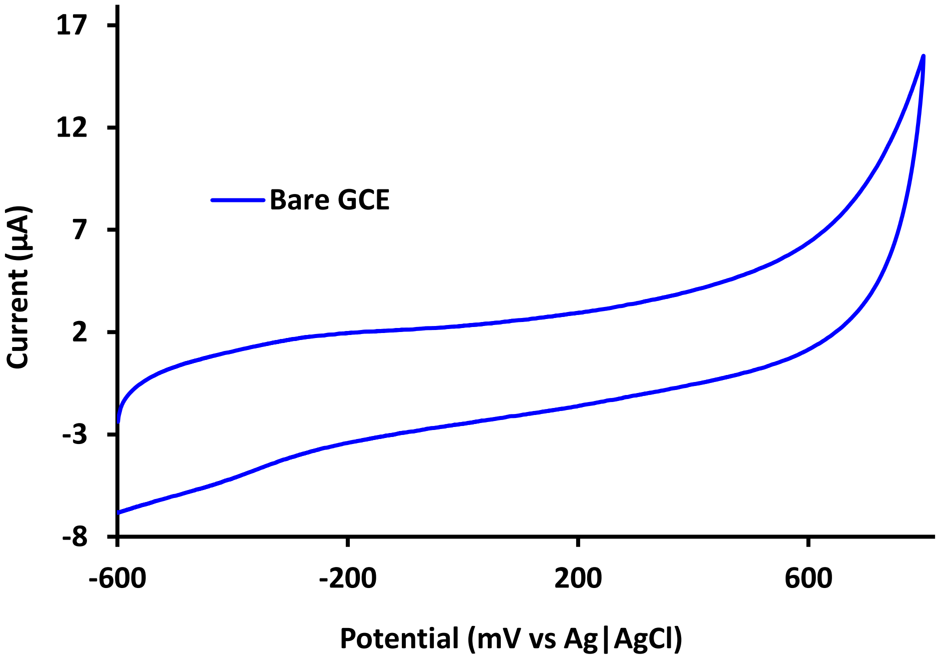

Fig. A17: Cyclic voltammogram of the bare electrode in the presence of 2.0 mM of hydrazine, in 0.1 M NaOH, at a scan rate of 100 mV/s.

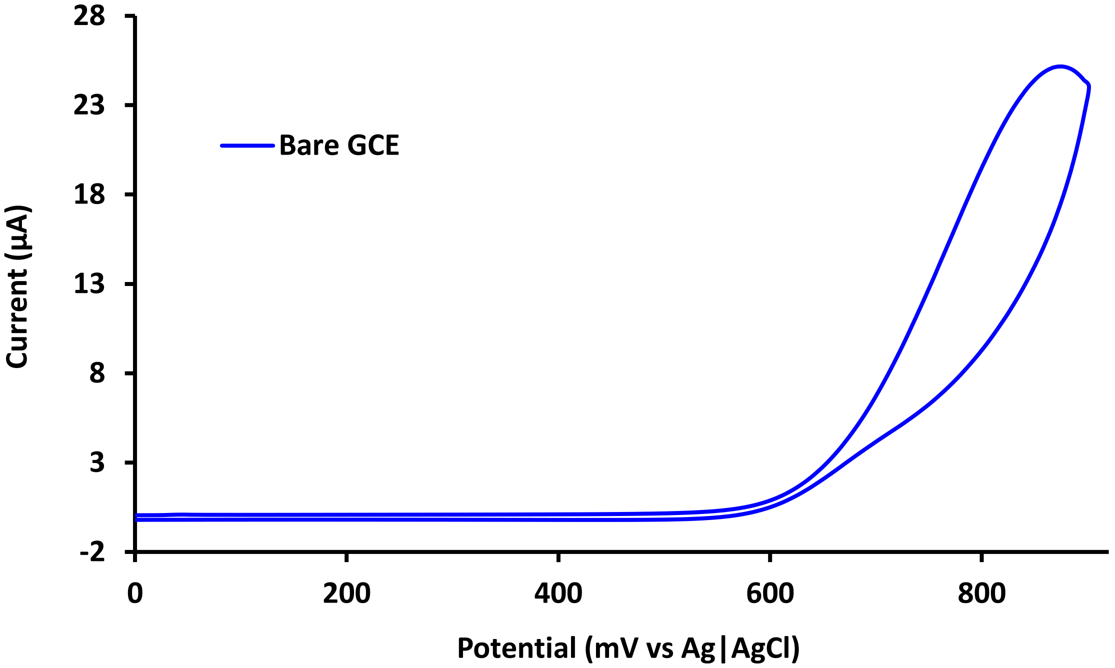

Fig. A18: Cyclic voltammogram of the bare electrode in the presence of 2.0 mM of nitrite, in 0.1 M PBS (pH 7.5), at a scan rate of 100 mV/s.